UNIVERSITY OF SOUTHAMPTON

FACULTY OF PHYSICAL SCIENCE AND ENGINEERING

OPTOELECTRONICS RESEARCH CENTRE

Volume 1 of 1

Development of Visible-to-LWIR multispectral chalcogenide glasses

by

ANDREA RAVAGLI

Thesis for the degree of Doctor of Phylosophy

[September_2018]

UNIVERSITY OF SOUTHAMPTON

<u>ABSTRACT</u>

FACULTY OF PHYSICAL SCIENCE AND ENGINEERING

Thesis for the degree of Doctor of Philosophy

DEVELOPMENT OF VISIBLE-TO-LWIR MULTISPECTRAL CHALCOGENIDE GLASSES

Andrea Ravagli

In the last four decades, Gallium Lanthanum Sulphide (GLS) glasses have been studied and proposed as material for active and passive applications. In this thesis, the effect of Se, Te, In and Cs on GLS is described presenting a new class of chalcogenide glasses with transparency from Visible to Long Wave IR range (500 nm – 16 µm). The addition of the new component was done by exchanging S with Se and Te, Ga with In and La with Cs in a variety of combinations to probe the glass forming ability of the new systems. The glasses were prepared mixing the precursors in a dry-N_2 glovebox and adopting a melt-quench method in a Ar-purged furnace. The powders were melted at 1150 °C for 24 hours and then annealed at 490 °C for 24 hours. Glass formation in Se, Te and In samples was observed and the optical, thermal and mechanical properties of these samples were characterised. The addition of the new components resulted in an extension of the transmission towards the LWIR. Particularly, the largest improvement was observed for the sample containing 60 mol% Ga_2Se_3 which transmitted light up to 15 µm. This sample also exhibited transmission in the visible range up to 550 nm. Although modest improvements were observed for Te-GLS and In-GLS, these compositions exhibited phase separation and large losses in mass during the melting process. The thermal and mechanical properties of the samples were studied to investigate the possibility to produce optical components such as multispectral lenses. The results obtained showed superior properties than the commercial chalcogenide glasses. Indeed, higher characteristic temperatures, mechanical strength and comparable thermal expansion were observed. The effect of the temperature on the optical properties was studied up to 500 °C for high temperature applications. The properties in the THz spectrum were studied to study the dielectric properties of the glasses. The n_2 was measured for supercontinuum generation and other applications in non-linear optics. The spectral properties of Nd^{3+} and Er^{3+} were studied for applications as amplifiers and middle-IR lasers. For these samples, mathematical models supported the experimental results to better understand the mechanism of light emission.

Table of Contents

Table of Contents

Table of Tables

Table of Tables

Table of Figures

Table of Figures

Academic Thesis: Declaration Of Authorship

I, Andrea Ravagli declare that this thesis and the work presented in it are my own and has been generated by me as the result of my own original research.

Development of Visible-to-LWIR multispectral chalcogenide glasses

I confirm that:

1. This work was done wholly or mainly while in candidature for a research degree at this University;
2. Where any part of this thesis has previously been submitted for a degree or any other qualification at this University or any other institution, this has been clearly stated;
3. Where I have consulted the published work of others, this is always clearly attributed;
4. Where I have quoted from the work of others, the source is always given. With the exception of such quotations, this thesis is entirely my own work;
5. I have acknowledged all main sources of help;
6. Where the thesis is based on work done by myself jointly with others, I have made clear exactly what was done by others and what I have contributed myself;
7. Parts of this work have been published as:

- *"Structural and spectral characterisation of Er^{3+} and Nd^{3+} doped Ga-La-S-Se glasses"*, **Ravagli, A.**, et al., RSC Adv., 2018, **8**, 27556, DOI: 10.1039/c8ra04795b.
- *"Optical, Thermal, and Mechanical Characterization of Ga$_2$Se$_3$-Added GLS Glass"*, **Ravagli, A.**, et al., Advanced Materials, Vol. 29, Issue 27, 2017, DOI: 10.1002/adma.201606329.
- "*Ga-La-S-Se glass for visible and thermal imaging*", **Ravagli, A.**, et al., Advanced Optical Technologies, Vol. 6, issue 2, 2017, DOI: 10.1515/aot-2016-0069.
- "Dielectric and structural characterisation of chalcogenide glasses via terahertz time-domain spectroscopy", **Ravagli, A.,** et al., Optical Materials, Vol. 69, 2017, DOI: j.optmat.2017.04.057.
- *"Nonlinear refractive index of ultrafast laser inscribed waveguides in gallium lanthanum sulphide",* Demetriou, G., Hewak, D.W., **Ravagli, A.,** et al., Applied Optics, Vol. 56, Issue 19, 2017, DOI: AO.56.005407.
- *"Tuneable sputtered films by doping for wearable and flexible thermoelectrics",* Morgan, K., **Ravagli, A.**, et al, at MRS Fall Meeting 2017, Boston, United States, 26 Nov - 01 Dec 2017.
- *"Enhancing the applications of chalcogenide glass for passive and active multispectral applications"* Hewak, D., **Ravagli, A.**, et al, at SPIE Security and Defence, Warsaw, Poland, 11 - 14 Sep 2017.

Academic Thesis: Declaration Of Authorship

- *"Structural modification of Ga-La-S glass for a new family of chalcogenides"*, **Ravagli, A.**, et al., 2017, at <u>SPIE DCS Defence and Security</u>, Anaheim, United States, 09 - 13 Apr 2017, DOI: 10.1117/12.2262091.

- *"Measurement of dn/dT and dk/dT of optical crystals, ceramics, and chalcogenide glasses between 80K and 1050K"*, O'Keefe, E., Craig, C., Hewak, D., Hobson, P., Humphrey, A., Pearce, D. and **Ravagli, A.,** at <u>SPIE DCS Defence and Security</u>, Anaheim, United States, 09 - 13 Apr 2017.

- *"Spatially controlled doping of silver in chalcogenide glass by thermal, photo and electron beam effects"*, Morgan, K., Craig, C., **Ravagli, A.**, et al, at <u>2017 European Conference on Lasers and Electro-Optics and European Quantum Electronics Conference,</u> Berlin, Germany, 25–29 June 2017.

- *"Modular and extensible lesson on fiber optics for youths,"* Wong, N. H. L., Tong, A. S. K., M. T., Posner, and **Ravagli, A.,** 2017, Proceedings of 14th Conference on Education and Training in Optics and Photonics, DOI10.1117/12.2266445.

- *"Cathedral outreach: student-led workshops for school curriculum enhancement in non-traditional environments"*, Posner, M., Jantzen, A., van Putten, L., **Ravagli, A.**, et al, at <u>Education and Training in Optics and Photonics 2017</u>, Hangzhou, China, 29–31 May 2017. DOI: 10.1117/12.2266445

- *"Next generation chalcogenide glasses for visible and IR imaging"* Hewak, D., Bastock, P., Craig, C., Huang, C., Khan, K., Ravagli, A., et al, at <u>SPIE Security + Defence and Remote Sensing,</u> Edinburgh, United Kingdom, 26 - 29 September 2016.

- *"Ga-La-S glass for UV and IR applications"*, **Ravagli, A.**, et al, at <u>IONS Quebec 2016</u>, Quebec City, Canada, June 2016.

- GB Patent Application No. GB1615780.2.

- Andrea Ravagli. (2018, September 3). Judd-Ofelt Analysis (Version 1). Zenodo. http://doi.org/10.5281/zenodo.1408112

Signed: ....

Date: ....

Acknowledgements

I would like to start by thanking my supervisor Dan Hewak for giving me the opportunity to work on a very exciting project, being impartial throughout this experience in research and academia. A big thank you goes to all the people who helped and supported me during my research, Paul Bastock, Chris Craig, Ed Weatherby, Adam Lewis, Ghadah Alzaidy, Fernando Guzman, Bruno Moog and Katrina Morgan. I gratefully acknowledge the financial support of the UK Engineering and Physical Science Research Council.

The number of people I would like to acknowledge for their personal support is countless and the positive impact of some of them throughout this long journey was invaluable. Let's start from my companions of the "Fritzies" group (previously named "Cerveza Cartel, no gringos") for all the good times we spent together. Whether it was a quick chat or a session of politically incorrect jokes, your company has been essential to get through stressful moments and enjoy the good ones. A special thank you also goes to Angeles, Omar, Amy, Rex and Olly for their friendship and their support.

A super special thank you to Lochana, friend of a lifetime always ready with his wise advice and extremely open mind. As you said on this important achievement: "It makes me happy, considering where we both come from. We've come far and there's definitely much more to reach!". From playing football in a courtyard of an industrial estate to the completion of my PhD, your friendship has been indispensable and a continuous source of inspiration.

Last but not least, my family. A million words would not be enough to express how grateful I am. You have all been an example of tenacity, hard work and generosity that not even the best school would have provided. Even if you are not scientists or doctors, facing the personal challenges through my PhD would have been impossible without you as inspiration and supporters. My eternal gratitude for this achievement, my previous achievements and any other challenge I will succeed on goes to you.

"Fortuna audaces iuvat".

Definitions and Abbreviations

CF – Crystal Field

c_p – Specific heat capacity at constant pressure

CTE – Coefficient of Thermal Expansion

CVD – Chemical Vapour Deposition

DSC – Differential Scanning Calorimetry

DTA – Differential Thermal Analysis

ED – Electric dipole

EXAFS – Extended X-ray Absroption Fine Structure

GLS – Gallium Lanthanum Sulfide

HEXRD – High Energy X-Ray Diffreaction

H_v – Vickers Hardness

IR - InfraRed

J – Total angular momentum

L – Orbital Angular Momentum

LWIR – Long Wave InfraRed

Ln - Lanthanide

MD – Magnetic Dipole

n – refractive index

n_2 – non-linear refractive index

NA –Numerical Aperture

R_c – Critical cooling rate

RE – Rare Earth

S – Spin angular momentum

T_g – Glass transition temperature

TGA – Thermo-gravimetrical Analysis

T_m – Melting point

TMA – Thermo-mechanical Analysis

T_s – Strain point

T_x – Crystallisation Temperature

VFT - Vogel–Fulcher–Tammann

XRD – X-Ray Diffraction

η - Viscosity

τ_m – Measured excited state lifetime

τ_{JO} – Judd-Ofelt excited state lifetime

15

Definitions and Abbreviations

Chapter 1

Introduction

1.1 The puzzle of glass

The compounds included in the nomenclature of "glass" are some of the most ancient and most used human-made materials. In fact, the first evidence of man-made glass was found in East Mesopotamia and was dated around 3500 BC.[1] This class of materials remains not fully understood due to their unique combination of macroscopic and microscopic properties. The uncertainties arise from the lack of long-range order in the molecular structure distinguishing these materials from crystals. This observation led to a significant number of attempts to formulate a correct and comprehensive definition of glass. Some of the most popular include: "Glass is…"

• "…a nonequilibrium, non-crystalline state of matter that appears solid on a short time scale but continuously relaxes towards the liquid state". [2]

• "…a frozen under-cooled liquid"; [2]

• "an inorganic product of fusion that has cooled to a rigid condition without crystallisation"; [3]

• "Glass is a non-equilibrium, non-crystalline condensed state of matter that exhibits a glass transition"; [4]

• "… an X-ray amorphous material that exhibits the glass transition. …";[5]

• "Glass is a solid having a non-crystalline structure, which continuously converts to a liquid upon heating"; [6]

Despite some differences in the aspects considered, all of the definitions above agree on the non-crystallinity of glass and on the observation of a glass transition temperature (T_g). At this particular temperature, a transition from a rubbery to a brittle state is observed with the atoms "frozen" in a liquid-like arrangement. The exact identification of the structure of glass is thus another object of debate in glass science. Indeed, the conventional techniques for structural characterisation such as X-Ray Diffraction, Raman spectroscopy, FTIR and NMR are not very effective. This is due to the capability of these techniques to reveal regular and periodical structures very precisely, whilst the non-periodical chemical structure of amorphous materials can

only be depicted as an approximated scenario. In literature, several studies on the short-range "order" of glass can be found. These works predicted the structure of glasses by means of computational simulations, High-Energy XRD (HEXRD) and Extended X-ray Absorption Fine Structure (EXAFS). [7] As a result, the atomic distances between the single components were calculated reliably. However, the coordination numbers calculated for the atoms represented an averaged result and were rarely integers. This left doubts on the chemistry of the coordination spheres and great effort are being spent on improving the in-silico simulation of the chemistry of amorphous materials. Indeed, the current models cannot study systems with more than a few thousands atoms which may not be a representative portion of the material as a whole and the coordination numbers are taken as an average.[8]–[10] In addition, this type of simulations are extremely demanding from a computational point of view and therefore it does not allow yet the development of systematic compositional studies. In light of these uncertainties, the investigation discussed in this thesis attempted to unravel the puzzle of the structure of a new glass combining the information obtained from a large number of characterisation techniques.

Although some of the properties of glass may not be fully explained, this material is widely produced and recycled in industrial applications. In 2008, in the territory of the EU-27 about 37 million tonnes of glass were produced. Among the large varieties of products, container glass was the most produced with a total amount of 21.4 million tonnes of which 50% was recycled.[11]

Usually, chalcogenide glasses are included in the category of speciality glass and differ from the other materials as they do not contain oxygen. Chalcogenides consists of S, Se and Te bonded covalently to other elements. The chemistry of these materials is responsible for their unique optical properties. The high atomic weight of chalcogens results in a low energy bandgap and wide transparency in the infrared (IR). The typical transmission occurs up to 13μm for sulphide glasses, 17μm for selenide glasses and 20μm for telluride glasses. [12] These materials are also strongly polarizable and exhibit a high linear refractive index (n = 2-3) and pronounced non-linear effects.[13]–[15] The interest for chalcogenides has been constantly growing since the 60's (Figure 1) leading to the development of commercial applications such as lenses or glass flats for middle and LWIR optics. Commercially available chalcogenides are made of a combinations of S, Se and Te with semi-metals such as Ge, As and Sb. [16]–[24] More exotic compositions and applications can be found in literature for laboratory-level glasses under development, one of which is described in this thesis.
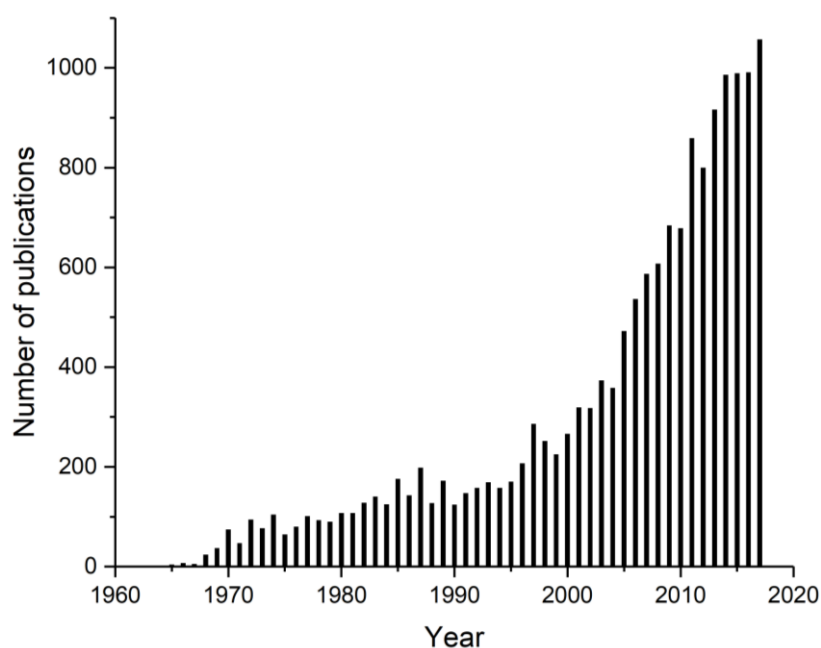
Figure 1: Histogram showing the number of publication on chalcogenides per year. Reference: www.scopus.com.

1.2   Motivations and aims of the project

The chalcogenide glasses predominantly applied for commercial infrared applications are based on As, Ge, Se and Te. [12] A large number of combinations between these four elements has been developed over the years and they find applications as passive and active media. In particular, multispectral imaging and mid-IR lasers are applications currently attracting the most of the interest. [25], [26] One of the main advantages of these commercial compositions is the possibility of easily producing fibres and lenses. Indeed, the physical-chemical properties allow fabrication processes at relatively low temperature avoiding crystallisation or phase separation. However, several drawbacks arise as a direct consequence of this capability. For starters, the chemistry of As, Ge, Se and Te involves weak bonds which make the glasses significantly more brittle and fragile than silica. In addition, the low melting point limits the application of these materials to temperatures close to ambient conditions. Lastly, Se and Te-based glasses possess a narrow optical bandgap energy and they rarely exhibit transparency in the UV-Visible range.

The issue of the poor mechanical properties could be tackled with glass ceramics in which a small portion of crystals is grown in the glass. [27] However, the presence of crystals causes scattering of light, which is not desirable for optical applications. Furthermore, the growth of crystals is usually carried out adding compounds such as CsCl, which increase the sensitivity of the materials to moisture obscuring several IR bands.[28] Hence the requirement for stronger materials that do not undergo phase separation during thermal processing. Gallium Lanthanum Sulphide glasses

Introduction

represent an alternative to glass ceramic. These glasses are promising materials as they possess excellent optical, thermal and mechanical properties with the potential to replace the currently used materials. The glass formation ability of the system gallium-lanthanum-sulphur was observed for the first time in 1976 by Lozac'h and co-workers. [29] Since then, several studies reported the unique properties of this glass which distinguish it from the other chalcogenide glasses.[24] They concluded that presence of La was the key factor determining the peculiar properties of this material. Indeed, the La-S bond is stronger than any other metal-sulphur bonds resulting in strong mechanical and thermal properties. Optically, this bond determined the transparency in part of the visible spectrum. In addition, all the properties of chalcogenides were preserved, including the IR transmission, high refractive index and strong non-linear effects. The studies depicted a promising scenario for GLS glasses and big efforts were spent to apply this material in optical devices. The best result was obtained in 1997 when lasing of Nd^{3+}-doped GLS fibres was reported.[30] To date, this represents the only case of laser activity reported in a chalcogenide glass and further efforts were spent to achieve laser activity with mid-IR wavelengths.[31], [32]. More recently, the research activity at the Optoelectronics Research Centre focused on the purification of GLS achieving significantly reduced attenuations throughout the range of transparency. However, the chemistry of the glass represented the main limitation to the IR transparency at wavelengths above 9 μm. For this reason, telluride glasses can transmit over 20 μm and they are widely used in thermal imaging despite their fragility.[33]

In view of these premises, the aim of this research project was to modify GLS glasses in order to extend the transmission window towards the thermal range of the spectrum between 8 – 14 μm. The approach used to achieve this goal is to adding Se, Te, In and CsCl to GLS decreasing the phonon energy of the material. A large number of compositions were studied to define the glass forming range of each system. In addition, an extensive number of optical, thermal and mechanical characterisations were needed to assess the effect of the new components on the properties of the glasses. These analyses were all interpreted as pieces of a puzzle and were used to have a clear pictures of the properties and capabilities of the materials. A large glass formation is desirable to tailor the spectral properties and improve IR transparency as much as possible. On the other hand, the addition of any of the substituents listed above was expected to cause a weakening of the mechanical and thermal properties with respect of regular GLS. Hence the necessity to find a compromise between concentration of optical and thermo-mechanical properties. These materials have been considered for applications as Rare Earth (RE) host. The investigation on RE-doped Se-GLS was carried out to assess the spectral properties of lanthanides in Se-GLS glasses aiming to tailor the concentration of dopant for laser applications. In principle, the improved transmission in the IR should increase the efficiency of the radiative transitions of

REs in this range. The light emission of Nd^{3+} and Er^{3+}-doped Se-GLS were investigated and compared to the results in literature to determine the dynamics of the radiative decays. In addition, the investigation intended to find the optimal concentration of dopant in order to maximise the radiative lifetime. The goals of the project can be summarised as follows:

• Extending the transmission window of GLS towards longer wavelengths;

• Studying the glass formation ability, the optical, thermal and mechanical properties; of Se, Te and CsCl-added GLS;

• Investigating the glass forming ability of Nd^{3+} and Er^{3+}-doped Se-GLS and their spectroscopy to optimise the concentration of dopants for laser applications.

1.3   Outline of the thesis

The thesis reports the work on the fabrication and characterisation of GLS-based chalcogenide glasses with the addition of Se, Te, In and CsCl. After an overview on chalcogenide glasses in Chapter 1, each of the following chapters include a literature survey relevant to the aspect discusses, a theoretical part and a detailed description of the experimental work.

In Chapter 2, the fabrication of the novel materials object if this study is described. The theory of glass formation and devitrification are described in this chapter. A review of the glass forming chalcogenides and the relative fabrication and purification technique is included. In addition, a summary of the impurities commonly found in chalcogenide glasses is outlined. The observation made in previous studies on GLS glasses are also described correlating the glass formation with the chemistry of the glass. The results of the structural characterisation are compared to the data available in literature.

In Chapter 3, the results of the optical characterisations are described. The chapter includes a theoretical introduction to the phenomena causing light absorption and a comparison of the results obtained with the literature. The improved optical transmission was compared to that of regular GLS. In addition, a test with a thermal camera was carried out in order to assess the improvement obtained. The investigation on the properties of the glasses in the THz domain was carried out in collaboration with Dr. Mira Naftaly at the National Physical Laboratories where the experiments were carried out. The Temperature-Dependent FTIR experiments were carried out with Dr. Eoin O'Keefe and Alastair Humphrey at laboratories of Qinetiq ltd. The experiments on the non-linear properties of Se-GLS glasses was carried in collaboration with Prof. Ajoy Kar, Dr. Mark Mackenzie and Dr. James Morris at Heriot-Watt University were the optical setup was located.

Introduction

In Chapter 4, the results of the thermal and mechanical characterisations are described. The chapter gives a theoretical description of the parameters determined within the experimental work, as well as an overview of the thermal behaviour of glass. The results were compared to the data available for commercial chalcogenide glasses. This was done since commercial chalcogenides represent examples of commercial-grade materials and preserving superior properties was one of the main motivations of the work.

In Chapter 5, the study of Nd^{3+} and Er^{3+}-doped Se-GLS are reported. A theoretical background on the spectroscopy governing light absorption by Rare Earths is given and the mechanisms of cross-relaxation, co-operative upconversion and radiation trapping are described. The models used for data analysis, namely Judd-Ofelt analysis and the Auzel Equations, are described. The results of this chapter were interpreted accounting for the emission mechanisms and the chemistry of the glass. The investigation reported in this chapter was carried out in collaboration with Prof. Daniel Milanese, Dr. Nadia Boetti and Dr. Diego Pugliese at the Politecnico di Torino (Italy) where the optical measurements were taken. The results were then confirmed in the laboratories of the Optoelectronics Research Centre where a replica of the optical set up was built.

In Chapter 6 the conclusions are drawn and possible further works are proposed.

Chapter 2

Chalcogenide glasses manufacture

2.1   Glass purification and fabrication

The performance of infrared glass in optical components is strongly dependent on the purity of the material. For this reason, a vast amount of effort has been spent on the improvement of the purity of the precursors through the development of novel purification and fabrication processes.

For glasses fabricated from volatile elements such as As, S, Se, Te, purification techniques that exploit their high vapour pressure can be used.[33], [34] For instance, selective sublimation and distillation were successfully carried out to reduce the amount of oxygen contained in the precursors. The first process can be used when the precursors and the relative oxides have a large difference in sublimation point. This is carried out by heating up the precursors in a dynamic vacuum.[35] The distillation process takes place in a multi-zone furnace in which the glass is located within the hottest zone. The vapours of the glass migrate towards the adjacent colder zones solidifying in the coldest. Generally, getter metals are added to the distillation batch to further remove oxygen and moisture adsorbed to the components of the melting system.[36] The getter metal is chosen according the strength of the bond it makes with the impurity, which must be greater than the bond strength between the impurity and the components of the glass. For instance, small quantities of Al metal can be added to the melt if the enthalpy of formation of Al-O bond is the lowest amongst the constituents of the glass melt. In this way, oxygen reacts preferentially with Al and the concentration of oxide impurities in the glass can be drastically reduced. However, the getter chosen for the melt must be inert towards the ampoule and the glass melt to avoid undesired contaminations. This purification process can also be carried out during the glass melting process though an in situ purification. In this case, the getter is separated from the glass via sublimation. Other getters such as porous silica were added to remove carbon but leading to an increase of Si-O absorption in the glass.[37]

For higher boiling elements such as Ge, the superficial oxide layer can be eliminated with acid etching.[38] On the other hand, gas-phase purification techniques can be used involving a reactive gas such as H_2 and H_2S. The reactive gas must be chosen in order to remove both metallic and non-metallic impurities from precursors or glasses. For instance, in previous work S_2Cl_2 vapour

Chalcogenide glasses manufacture

was adopted to reduce the amount of OH, SH and Ge-H impurities in Ge-S glass following the reactions:

$$2OH_{(s)} + S_2Cl_{2(g)} \rightarrow 2HCl_{(g)} + SO_{2(g)} \qquad \text{Equation 1}$$

$$2SH_{(s)} + S_2Cl_{2(g)} \rightarrow 2HCl_{(g)} + 4S_{(g)} \qquad \text{Equation 2}$$

$$2GeH_{(s)} + S_2Cl_{2(g)} \rightarrow 2HCl_{(g)} + 2GeS_{(g)} \qquad \text{Equation 3}$$
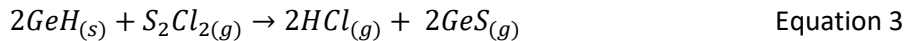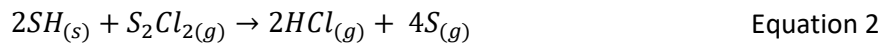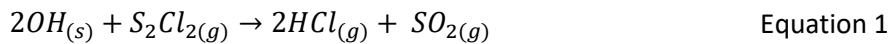
The treatment resulted in a substantial reduction of the attenuation due to light absorption of these species. For instance, the attenuation at 6.6µm caused by H_2O dropped from around 1300dB/m to below 100dB/m. [39] The reactive atmosphere process can be also be employed to synthesise the desired precursors from high purity metals and non-metals (>99.999%) from chalcogens in hydride form (e.g. H_2S) or carbide form (e.g. CS_2). Rare earth chalcogenides can be synthesised following this route starting from rare earths oxides or halides.[24], [40] Since rare earths establish very strong bonds with oxygen, the reaction occurs at a slow rate and temperatures over 1000°C are generally required.[41]

Further purification can be obtained by eliminating dissolved gasses from the melt through a process called fining. This process is widely applied in the industrial production of silicate glasses and consist of two mechanisms:[42]

-       primary fining, in which the formation of large bubbles is promoted by combined action of high temperature and the addition of chemicals releasing additional gas (fining agent). In this process, the equilibrium between bubbles and dissolved gas is moved towards the formation of bubbles. Once the size of the bubbles is large enough, they migrate towards the surface the melt and the gases are released in the atmosphere;

-       secondary fining, in which the gases contained in residual bubbles are dissolved back in the glass. This process takes place during the quenching stage, when the viscosity of the melt increases and the solubility of the gasses in the melt decreases. However, the decrease in temperature also results in the internal pressure of the bubble to decrease. If the glass is low in dissolved gases, those contained in the bubbles can diffuse in the glass and the bubbles can decrease in volume until they disappear.

The two processes can greatly reduce the concentration of volatile impurities such as O_2, H_2O, CO_2, SO_2, SeO_2. However, particular care must be taken in the choice of the fining agent, the amount used and the suitability with the glass. In the primary fining, an excessive bubbling can have detrimental effect on the glass leading in extreme cases to the formation of foam at the surface of the melt. On the other hand, since the secondary fining only aims to reduce the

scattering cause by bubbles in the glass, an excessive quantity of fining agent can result in undesired light absorption by the agent itself once the glass is formed.

Improvements of the fabrication process of chalcogenide glasses have been attempted following several routes. Chemical Vapour Deposition (CVD) is widely used to dope and fabricate silica-based glass preforms but it is inconvenient for the fabrication of chalcogenide glasses preform due to the slow deposition rate.[15] Melting routes are preferred and usually require silica ampoules due to high vapour pressure of precursors, especially in elemental forms. Once the elements are in place the ampoule is vacuumed down to 10^{-4} Pa and sealed. The vacuum can improve the purity of the melt eliminating the gases absorbed on the wall of the ampoule. [43] In particular eliminating moisture and oxygen is crucial for the performance of the glasses in the middle IR region.[44] The melting occurs in a rocking furnace (Figure 2) where the melt homogenised with a constant oscillation of the body of the furnace.[24], [33] The drawbacks of this technique are mainly due to safety concerns and special arrangements have to be set in order to avoid the explosion of the ampoule.[15], [45] In addition, the sealed system does not allow volatile impurities to boil off the melt thus preventing any in situ purification of the glass. As a result, impurities such as SH^- are considerably more concentrated in glasses melted in sealed ampoules than those melted in an open atmosphere.[24] Furthermore, silica itself can be a source of impurities if not dry, clean, pure and unreactive. In fact, to melt GLS in a silica ampoule, a carbon crucible or carbon coated ampoules are needed due to reactivity between silica and La_2S_3.[46]
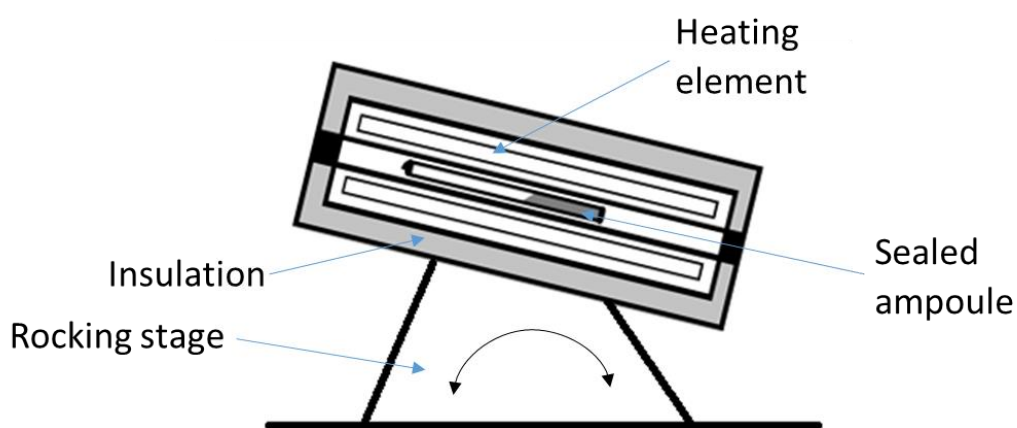
Figure 2: Schematics of a rocking furnace. The sealed ampoule containing the glass melt is docked in the furnace where a moving stage allows the apparatus to oscillate.

The main effect of impurities to optical materials is to compromise the transparency within specific spectral regions. A summary of the main absorption bands in sulphide and selenide glasses is reported in Table 1. Ensuring low levels of oxygen, hydrogen and carbon is essential to

produce materials with good transmission in the middle (3 – 8 μm) and LWIR region (8 – 15 μm). In addition, impurities can interact with rare earth in doped glasses, quenching emission and lifetime of the excited states dissipating the energy as emitted light into molecular vibrations (see Section 3.1.2).[47] In this mechanism, the molecular vibrations bridge the energy gap between an electronic excited state and the sublevels of the material. For example, the effect of the OH vibration is particularly strong on emissions in the IR region such as 2700 nm and 1550 nm in Er^{3+} and 1300 nm in Pr^{3+}. [26], [48], [49] Impurities can also affect the glass formation of a melt provoking heterogeneous crystallisation within the specimen.[50] Crystalline inclusions also act as scattering centres and can compromise the transparency of the glass.

Table 1: Absorption bands of some impurities in chalcogenide glasses

Impurity	Absorption band (μm)	Reference
OH	2.92	[36]
SH	4.01, 3.65, 3.11, 2.05	[51]
SeH	7.80, 4.57, 4.12, 3.53, 2.32	[51]
SO	8.70	[52]
SeO_2	7.96, 8.7	[34]
SeO	10.67, 11.06	[53]
AsOH	10.80	[38]
(GaO)OH	10.59, 9.83	[54]
LaO	21.64	[55]
COS	4.95	[56]
CO_2	4.31, 4.33, 15.00	[56]
CS_2	6.68, 4.65	[56]
CSe_2	7.8	[56]

2.2   Melting procedure and apparatus for the fabrication of GLS glasses

The process applied to melt GLS glass and modified GLS compositions constitutes one of the main novelties of this work. In particular, the procedure adopted allowed us to manufacture selenide glasses within an open flowing atmosphere, as opposed to the sealed ampoule approach conventionally used. The furnace set up is sketched in Figure 3.
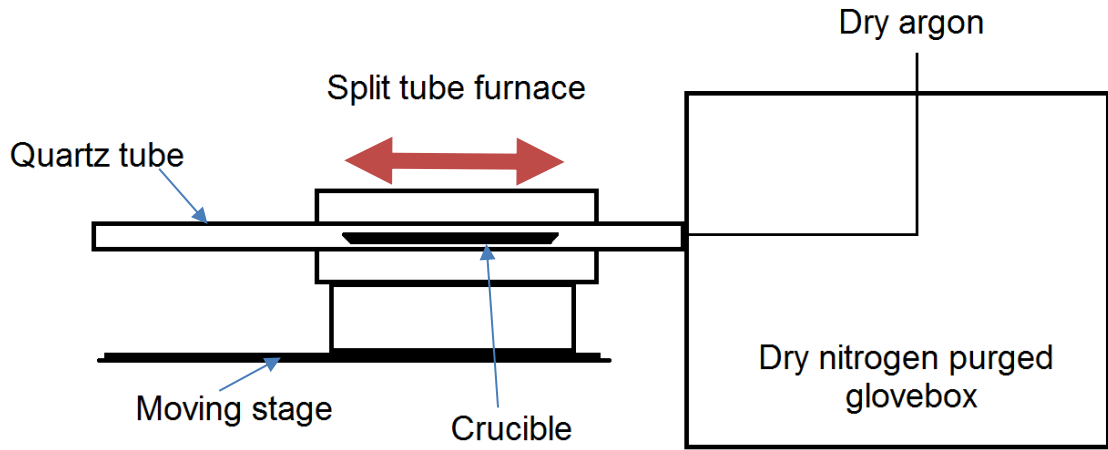
Figure 3: Schematic of the melting system adopted for the synthesis of Se-GLS.

The chemistry of the precursors is the key factor that allows us to avoid the necessity of a sealed system. As described in Section 2.1, S, Se and Te used as elements have a high vapour pressure. Therefore, they are not suitable for open melting systems and not compatible to alloying with the high melting temperature of La. In addition, high purity La can be expensive and requires particular arrangements for handling and storage due to its strong reactivity with moisture. These issues can be tackled using metal-chalcogen compounds, namely La_2S_3, Ga_2S_3, Ga_2Se_3, Ga_2Te_3, In_2S_3. The purity of the precursors used to manufacture the samples are reported in Appendix A. It is expressed on a metal basis thus not considering oxygen as an impurity. The commercial supplies of La_2S_3 only provides 3N purity (99.9%), whilst 5N Ga_2S_3 and La_2Se_3 can be found. Improvements to the quality of the glass can be made through the production of precursors from high purity metals. Gallium precursors can be produced converting commercially available high purity Ga (7N) with H_2S and Se following the reactions:

$$2Ga_{(s)} + 3H_2S_{(g)} \rightarrow Ga_2S_{3\,(s)} + 3H_{2\,(g)} \qquad\qquad \text{Equation 4}$$

$$2Ga_{(s)} + 3S_{(g)} \rightarrow Ga_2S_{3\,(s)} \qquad\qquad \text{Equation 5}$$
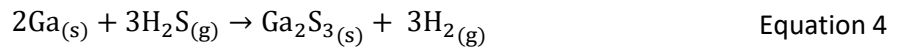
For La_2S_3 a different solid precursor should be used due to the reactivity of metallic La with moisture. Generally, 5N La_2O_3 can be used with good conversions. However, since oxide impurities can be deleterious for IR transparency, high purity halide precursors can also be employed. The conversions are done with H_2S following the mechanisms:

$$La_2O_{3(s)} + 3H_2S_{(g)} \rightarrow La_2S_{3(s)} + 3H_2O_{(g)} \qquad\qquad \text{Equation 6}$$

$$2LaX_{3(s)}(X = F, Cl) + 3H_2S_{(g)} \rightarrow La_2S_{3(s)} + 6HX_{(g)} \qquad\qquad \text{Equation 7}$$

Chalcogenide glasses manufacture
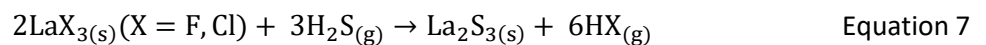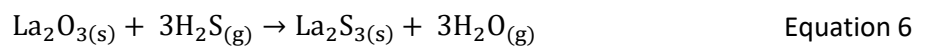
In order to achieve higher purities than the precursors available in the market, the process and the system adopted must be carefully optimised. Particularly, the conversion time must be carefully calibrated to avoid the excessive addition of S and Se which can compromise the glass formation.

2.2.1 Melting protocol and purity of modified GLS glasses

The precursors used for the study were not pre-treated with any purification process since the fraction of oxides contained was low and did not compromise glass formation or the optical properties. The presence of residual impurities in the glasses is presumably due to the contaminants in the precursors due to the special arrangements adopted for the glass melt. In particular, to ensure low oxygen content the gas used during the fabrication was dried to a moisture level of 1 ppb and the and the quartz tube was baked before the melt to eliminate adsorbed moisture. The use of getters has been considered but not applied for several reasons. Firstly, the separation of the getter cannot be carried out via distillation since the precursors melt and boil at extremely different temperatures. For instance, the melting point of Ga_2S_3 is 1090°C and 2100°C for La_2S_3.[57] Secondly, the bond strength of La-O bond was found to be one of the strongest reported in literature. Therefore, the metals commonly used in literature would not be effective and may contaminate the glass. The use of boron has been considered due to the strong bonding with oxygen. However, the separation from the glass represented a significant obstacle since boron oxide sublimates at 1500°C and a large amount of glass can be lost at that temperature.

To preserve the purity of the precursors, a dry-N_2 glovebox was used as storage to avoid exposure to oxygen and moisture preserving the purity. The precursors are mixed with the desired ratio and homogenised on a roller mixer for 1 hour. The homogenised mixture is then poured in a vitreous carbon crucible and placed in the split tube furnace. The choice of the materials for crucible and glass tube is important as it can afflict the quality of the glass. Crucibles for glass melting can be made of platinum, silica or alumina due to their resistance to high temperatures. However, those materials were found to be soluble in molten GLS. Vitreous carbon crucible can be adopted provided that the crucible did not devitrify and was not damaged during previous glass melts. These requirements are necessary to avoid the contamination of the glass since carbon is one of the most detrimental impurities for IR transmission as shown in Table 1. The tube was made of quartz to resist to a large number of glass melts and retain the shape and the mechanical strength after every melt. The tubes are washed in HF bath after every glass melt to eliminate any contamination to occur to the following melt. The clean tubes must undergo a heating cycle before any glass melts to eliminate residual water and HF from previous cleanings.

Once the tube furnace is set up, a stream of Ar is flowed through the tube for the whole length of the process. The stream is pre-filtered to eliminate oxygen, moisture and metals coming from the piping system. The filter employed is a ultra-fine point of use filter that reduced the moisture level from 10 ppbV to 1 ppbV. The Ar flow had the role of removing volatile compounds evaporating from the melts. In particular, SeO_2 and SO_2 can be eliminated providing further purification of the glass. This in-situ purification was done pre-heating the powders for 3 hours and kept occurring during the glass melts. The pre-heating step helped to eliminate volatile impurities before the mixture melts in order to avoid and excessive bubbling.

The melting process is carried out at 1150 °C which is only high enough to melt Ga_2S_3. However, once this component has melted it can act as a solvent and La_2S_3 is solubilised going to the liquid phase at a temperature much lower than its melting point. Following the full meting cycle the loss of mass at the end of the glass melt is around 1% which proves the stability of the precursors at the process temperature. The addition of Ga_2Se_3 (T_m = 1020 °C), In_2S_3 (T_m = 1050 °C) and In_2Se_3 (T_m = 890 °C) followed the same principle with a loss of mass of 2-3% for samples with high In and Se content.[57] For Ga_2Te_3 (T_m = 790 °C) the loss of mass was considerably higher (around 10%) and only a proof of principle of the glass formation could be done. For future studies of this glass forming system may require a sealed system for glass melting. The melt is kept at 1150 °C for 24 hours and then quenched to room temperature sliding the furnace away from the crucibles. If the glass formation occurs, the samples are then annealed to strengthen the glass. The annealing step was carried out at 490 °C for all the samples as this temperature was between the strain point and the glass transition temperature (see Chapter Chapter 4).

The process described was successfully used to produce Se-based chalcogenide glasses with an open atmosphere. Commercial and research grade Se-glasses are currently synthetised with sealed systems. An open system dramatically facilitates the glass production in terms of safety, preparation and quality of the final product. Future developments may lead to the adoption of this technology for the production of commercial materials.

2.3   Glass formation

The method usually applied in glass manufacturing is the melt-quench process. This method consists of two stages. In the first step, the precursors are melted and kept in the liquid state for the time required to obtain a homogeneous melt. In the second step, also known as "quenching", the temperature is abruptly decreased from above the melting temperature (T_m) to room temperature. If the quench occurs with a high rate, crystallisation of the melt can be avoided and glass formation is observed. From a microscopic perspective, the quenching must be fast enough so that the atoms do not have enough time to arrange a crystalline lattice. As a result, the

material is found into a quasi-equilibrium phase.[58] Macroscopically, the drop in temperature causes the increase of the viscosity of the fluid decreasing the mobility of the atoms. The glass transition takes place when the viscosity reaches 10^{12} Pa·s. The temperature at which this process occurs is called glass transition temperature (T_g). At this point, the position of the atoms is frozen in an amorphous, liquid-like configuration and the glass is formed. [59]
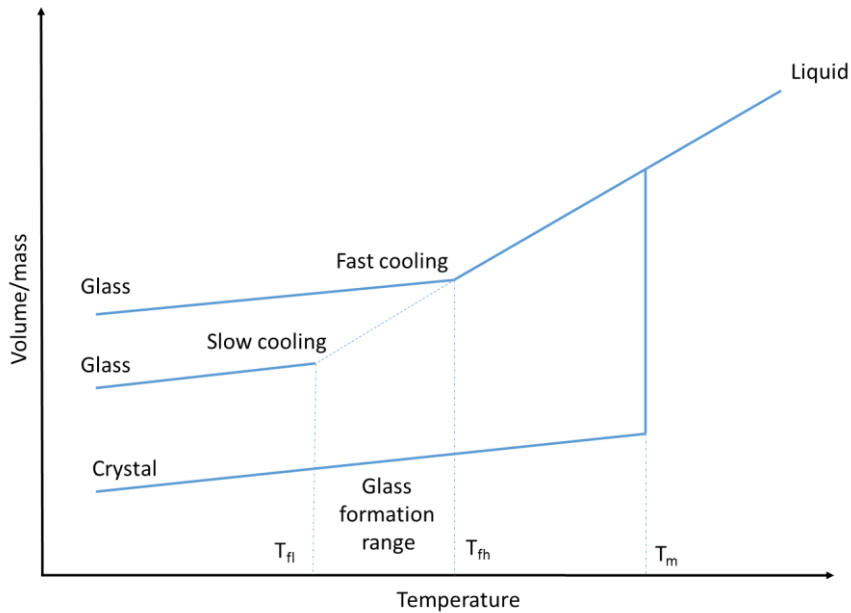
Figure 4: Cooling curve of a glass forming melt.

As shown in Figure 4, during the quenching stage the volume of the melt (y axis) of the melt slowly decreases reaching the T_g range. Within this range, the temperature in which the material reaches a meta-stable equilibrium in the solid state is known as fictive temperature.[59] The fictive temperature is correlated to the configuration of the atoms frozen in the quasi-equilibrium stage. This configuration strongly deviates from the crystalline equilibrium state in as-quenched glass samples, which can be very fragile due to retention of structural stress. Hence the tendency for as-quenched glasses to undergo a relaxation mechanism towards more stable arrangements. This mechanism can be accelerated by annealing the glass. This process is usually carried out at temperatures around T_g and provokes a decrease in fictive temperature. Chalcogenide glasses can be effectively annealed at temperatures below T_g due to the formation of weak chemical bonds.[58] The structural relaxation induced with the annealing process can follow two models.[60] The first one is known as Topological Short-Range Ordering and considers the change in position of the atoms regardless the chemical species. This approach can be used to account for changes in density due to the annealing. The second model is called Chemical Short-Range Ordering and describes the change of the chemical environment around a given atom. This model can predict the formation of given chemical bonds which affect the mechanical, thermal and optical characteristics of the material. Therefore, post-quenching treatments can be potentially

used to tailor the properties of a glass sample. For instance, annealing can be used to strengthen the glass, erase the effect of photodarkening and photoinduced-anisotropy and increase the transparency of glass ceramics.[14], [61], [62]

The minimum cooling rate for the glass formation, also known as critical cooling rate (R_c), is often used as a parameter to probe the glass forming ability of a glass forming liquid.[63] A low R_c is characteristic of liquid with a strong glass forming ability. This parameter can be estimated from thermal analysis applying the equation:

$$\ln \alpha = \ln R_c + \frac{d}{(T_L - T_x)^2}$$

Equation 8

where α is the heating rate, T_L is the liquidus temperature, T_x is the crystallisation temperature and d is a constant specific to the glass.[63] The general trend of the change in R_c caused by the substitution of S by heavier chalcogens has been object of several studies.[47], [64] It was found that for As-S-Se-Te the glass forming ability was reduced for binary systems with increasingly heavy chalcogens (i.e. As-S>As-Se>As-Te). However, for a larger number of components the opposite trend was exhibited (As-Se-Te>As-Se). These observations are related to the size of the anions ($S^{2-}<Se^{2-}<Te^{2-}$) and the complexity of the glass network. In particular, the bulkier the ions the smaller the number of possible bonding configurations. At the same time, increasing the number of components in the alloy decreases the tendency to crystallise.

Other than crystallisation, devitrification may occur during glass melting due to liquid-liquid phase separation. This phenomenon results from the limited miscibility of the components of a melt and takes place at a temperature between T_g and T_m. Ideally, if the quenching rate is fast the phase separation can be avoided. However, thermal treatments such as annealing can cause phase separation after the glass is formed. This mechanism of phase separation is named as spinodal decomposition and arise from the lack of an energy barrier between the single and double phase configurations. In fact, the formation of two phases is known to decrease the free energy of the system improving its stability.[59]

2.3.1 Glass formation of GLS glass system

The glass forming ability of the La_2S_3-Ga_2S_3 was first observed in 1976 by Lozac'h et al.[29] Their extensive study demonstrated that a variety of rare earth sulphides combined with Ga_2S_3 can be used to obtain glass. The largest glass-forming region was observed for La_2S_3 ranging between 15 mol% and 50 mol% of La_2S_3. Thermal studies over the whole range of compositions remarked the occurrence of a eutectic for a concentration of La_2S_3 of 16 mol%, where the T_g and T_x reached local maxima at that composition.

Chalcogenide glasses manufacture

Further studies were carried out on the analogous La_2Se_3-Ga_2Se_3 reporting the lack of glass formation for this binary system. This observation was explained considering the reduced ionic character of La-Se with respect of La-S which could not be stabilised by Ga-Se as a network former. Furthermore, attempts to achieve glass formation with the system La_2Se_3-$GeSe_2$ had the same outcome despite the stronger covalent character of Ge-Se. Therefore, the study tackled the issue starting from the glass forming system Ga_2Se_3-$GeSe_2$ and probing the glass formation as La_2Se_3 was added.[65] Glass formation was achieved following this route for samples containing up to 30 mol% La_2Se_3. However, the glass forming region did not include any germanium-free sample.

A study reported by Shephard et al. observed glass formation of GLS added with small quantities of GaSe, up to 10 mol%. For these new compositions, an expansion of the transmission window towards longer wavelengths was expected. The study highlights how GLS is capable to accept Se which, however, does not appear to have any major effect on the optical properties.[66] The unchanged properties could arise from several factors. Firstly, the unchanged IR cut-off and the blue-shifted UV cut-off suggest that the GaSe used contained a considerable amount of oxygen. Since Ga-O and Se-O both absorb at longer wavelengths than the observed IR cut-off, effect of Se was not visible. Secondly, the increase of refractive index and density were observed as a consequence of the increase in concentration of Se. However, since the stoichiometry of the GaSe is different from Ga_2S_3 the amount of Se added was sub-stoichiometric. Therefore, the amount of selenium added may have not been large enough and the different oxidation state of Ga (3+ in Ga_2S_3, 2+ in GaSe) could have changed the chemistry and the dielectric properties of the glass.

Section 2.4 describes the glass formation of the system La_2S_3-Ga_2S_3-Ga_2Se_3 aiming to give a comprehensive description of the conditions of the glass formation. In addition, glass formation for Ga_2Te_3, In_2S_3 and CsCl will be described giving insight about future developments of those optical materials.

2.4   Glass formation of modified GLS glasses

2.4.1   Se-GLS glasses

The glass forming region for the system La_2S_3-Ga_2S_3-Ga_2Se_3 was determined by synthetising samples with different concentrations of the three components and assessing their phase via Raman spectroscopy and X-Ray Diffraction (XRD). The samples were melted in a cylindrical crucible and quenched in air as described in Section 2.2.1. The precursors were batched aiming for a weight around 30 g to ensure the repeatability of the process adopted. Readers are referred

to Appendix B and Appendix C where principles of Raman spectroscopy and XRD are reported. The ternary phase diagram for the system is shown in Figure 5. The predicted glass forming region (segmented line) is delimited by samples forming glass ceramics after quenching and the glass forming region of the La_2S_3-Ga_2S_3 as reported by Bastock et al.[67] For the tie line representing 30 mol% La_2S_3 the largest glass formation was observed up to full substitution of Ga_2S_3 by Ga_2Se_3. However, the composition 30 mol% La_2S_3 - 70mol% Ga_2Se_3 did not form a glass when the melting system described above was used.
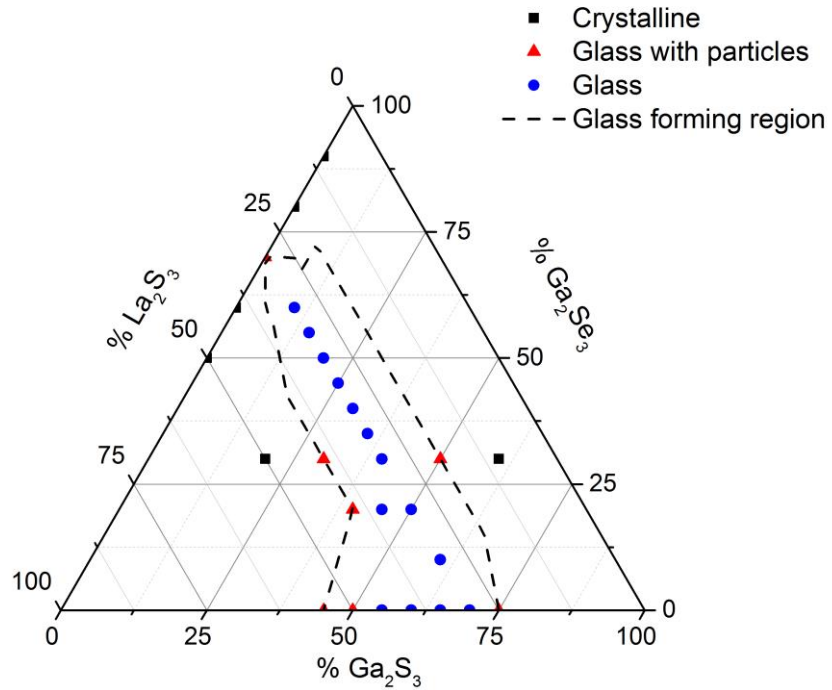
Figure 5: Glass formation of Ga-La-S-Se system.

In order to observe glass formation in this sample, an RF furnace had to be used instead of a split tube furnace. As shown in Figure 6, the RF coil was used to heat up a carbon crucible placed in inert open atmosphere. This system allowed the heating to be localised within the crucible resulting in faster quenching rates and glass formation.

Chalcogenide glasses manufacture
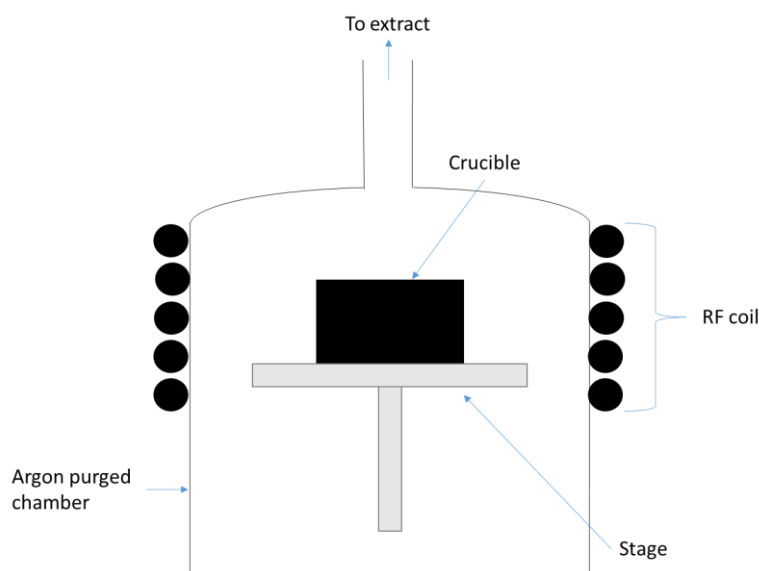
Figure 6: RF furnace used for melting glass with composition 30mol% La$_2$S$_3$ - 70mol% Ga$_2$Se$_3$.

Samples containing high La:Ga ratios exhibited a much narrower glass formation region. The largest glass formation was observed for contents of lanthanum between 20 and 40 mol% on the 30 mol% Ga$_2$Se$_3$ tie line. For concentrations higher than 40 mol% and lower than 20mol% concentrations of Ga$_2$Se$_3$ the glass formation region showed the tendency to form glass ceramics. These observations were found in good agreement with previous studies mentioned above.[63], [65] The addition of heavier chalcogens results in an increased tendency to crystallise. Initially this character is buffered by the additional degree of freedom added by a fourth component (i.e. Se) which enlarges the glass formation. Subsequently, for concentrations of Ga$_2$Se$_3$ exceeding 30 mol% the tendency to crystallise becomes the predominant character. In addition, the strong glass formation observed for 30 mol% La$_2$S$_3$ can be due to the optimal S:Se ratios which can counter balance the ionic character of La$_2$S$_3$.

Raman spectroscopy was used for an initial assessment of the phase of the samples then confirmed by powder XRD. In principle, the Raman spectrum for an amorphous material should consist of broadened peaks representing the range of angles assumed by a given oscillator. On the contrary, a crystalline material will give a spectrum with sharp peaks.[68] The Raman spectra for the glass forming samples containing 30 mol% La$_2$S$_3$ are shown in Figure 7. The spectra show three broad shifts merged over a large range from 150 to 350 cm^{-1}. The shift centred at 325 cm^{-1} belongs to high frequency vibrations which could be assigned to sulphur-coordinated metals. The intensity of this band gradually fades as Ga$_2$S$_3$ is replaced by Ga$_2$Se$_3$. Therefore this peak can be assigned to the symmetric vibration of GaS$_4$ tetrahedra. Although previous studies on Ga$_2$S$_3$-based glasses reported this peak to be centred around 350 cm^{-1}, variations on the glassy host can lead to slightly different positions of the peak on the spectrum.[69] Indeed, maximum intensity of the shift varies for all the samples according to the ratio between the precursors. The second band

centred at 225 cm^{-1} corresponds to heavier elements. This peak increases in intensity and moves towards lower frequencies as the content of Ga_2Se_3 is increased. Therefore, this peak may be analogously assigned to the vibration of $GaSe_4$ tetrahedra. The shoulder peaks around 150 cm^{-1} is a feature registered in all the spectra. The origin of this peak may be due to La_2S_3 as it is the only invariant component through the range of compositions. In addition, previous works on La_2S_3 reported several Raman-active modes around 150 cm^{-1} for this compound.[70]
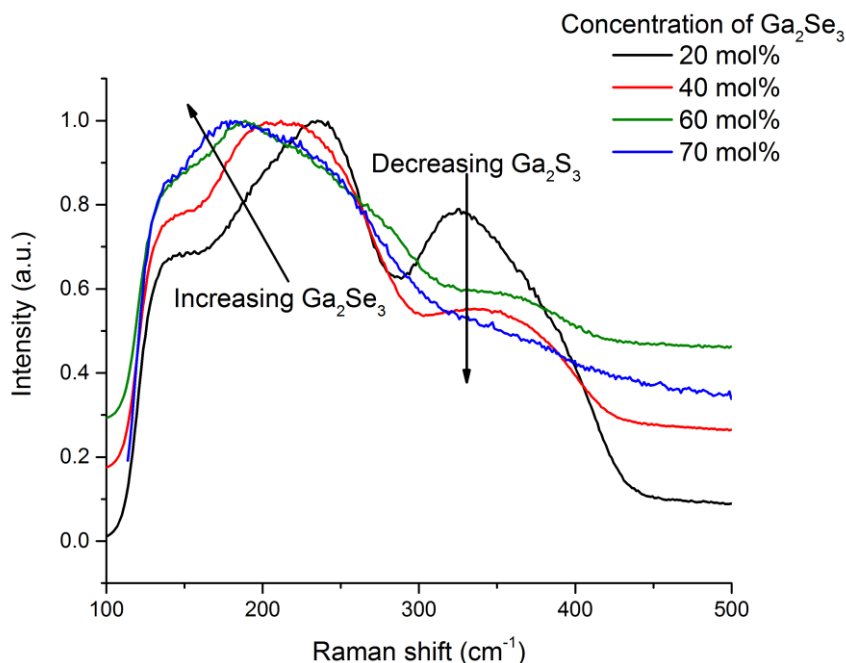
Figure 7: Raman spectra of samples containing 30 mol% La_2S_3.

The Raman spectra of samples in which the content of La_2S_3 was varied did not exhibit significant differences. Indeed, for constant concentrations of Ga_2Se_3 the band at 225 cm^{-1} does not undergo substantial shifts or changes of shapes, except for the case of the sample with composition 20mol% La_2S_3 - 50mol% Ga_2S_3 - 30mol% Ga_2Se_3 (Figure 8b, red line). For this sample, the spectra exhibited a $GaSe_4$ band characterised by multiple peaks with the peak shape deviating from the usual Gaussian profile. This sample was noticeably opaque as a result of phase separation during the glass formation. The presence of crystalline particles can be excluded since no signs of sharp peaks was found. The results of further investigations on the thermal properties are considered to support the hypothesis of phase separation.
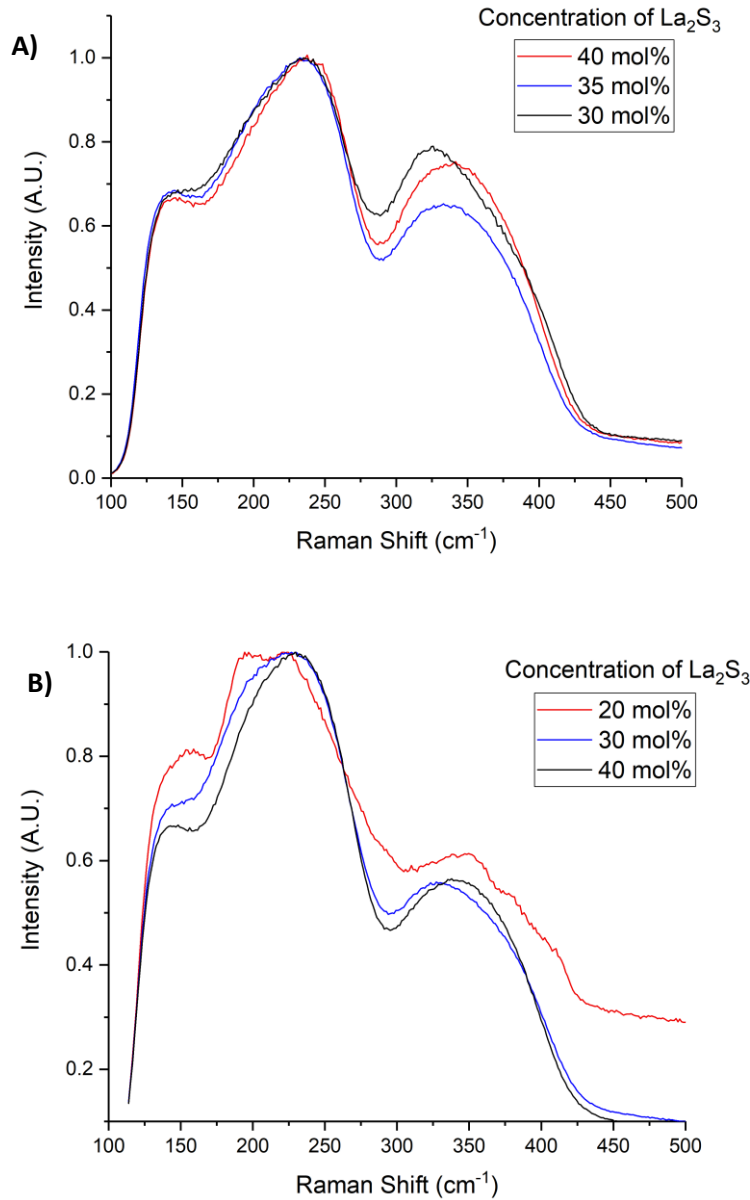
Figure 8: Raman spectra for samples containing A) 20 mol% Ga_2Se_3 and B) 30 mol% Ga_2Se_3

The comparison between the Raman spectra and XRD for amorphous and glass ceramics is represented in Figure 9A. As mentioned above, the difference between the two phases consists of the shape of the peaks. The XRD spectrum for amorphous sample containing 20 mol% Ga_2Se_3 does not show any sharp feature whilst the sample containing 70 mol% Ga_2Se_3 clearly has a peak at $2\theta = 48°$ corresponding to GaSe.[71] Similarly, Raman spectra (Figure 9B) for the sample consisting of 40mol% La_2S_3 - 40mol% Ga_2S_3 - 20mol% Ga_2Se_3 synthetized as both glass and glass ceramics shows that the crystalline form is characterised by sharp peaks. The peak corresponding to GaS_4 neatly exhibited three distinct sharp contributions confined within the range of the broad glassy peaks. This result agrees with fundamental studies on Raman spectroscopy in which the

glassy peaks were found to be the "envelop" of the sharp peaks of crystals. As this composition is found at the edge of the glass forming region, the melting process adopted produced both glass and glass ceramics. In particular, the position of the crucible within the system changed the quenching conditions. Therefore, the formation of crystals occurred when the crucible was positioned in areas of the system in which low quenching rates were achieved.
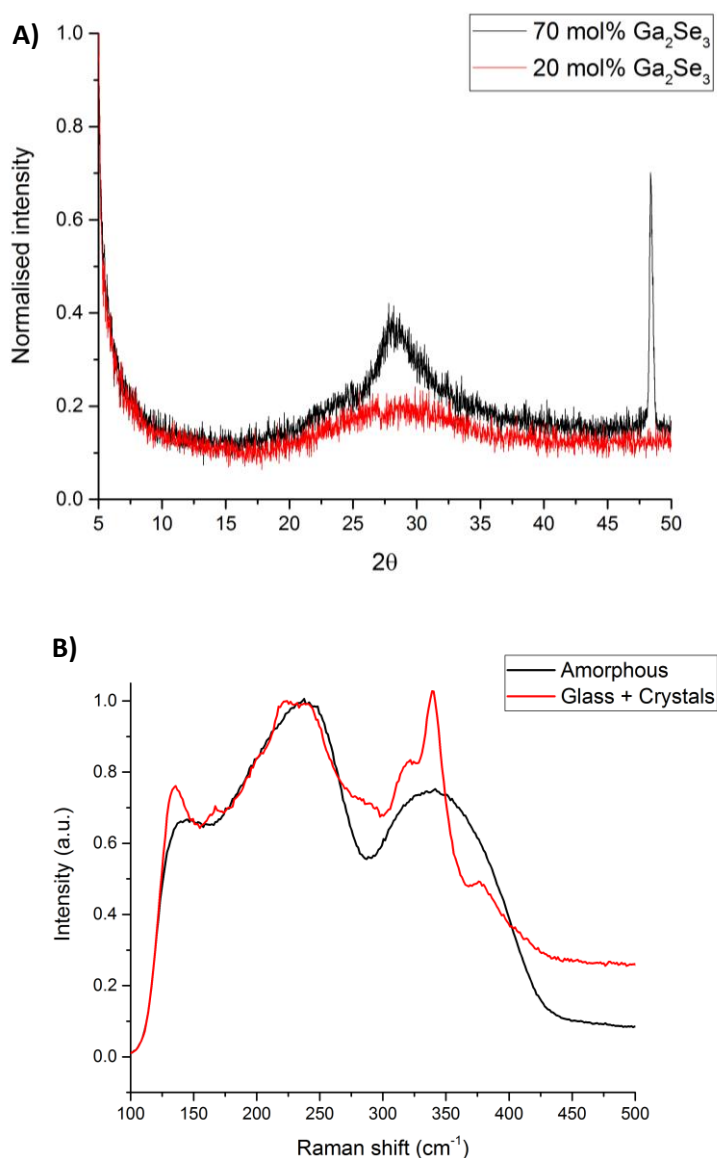
Figure 9: Assessment of amorphous phase in the samples. A) Comparison of XRD spectra of a fully amorphous sample and a glass ceramic sample; B) Comparison of Raman spectra of the amorphous and crystalline part for the sample containing 40mol% La_2S_3 -40mol% Ga_2S_3 - 20mol% Ga_2Se_3.

Both analysis agree on the amorphous phase of the samples for which glass formation was recognised. However, XRD required the samples to be crushed into fine powder making the glass more reactive towards atmospheric moisture and changes to the sample can be caused. Raman

spectroscopy was preferred for the characterisation of the samples because it is a non-destructive technique which does not require any pre-processing of the sample.

2.4.2   In, Te, CsCl modifications

The glass formation of Te-modified GLS was attempted by substituting Ga_2S_3 with Ga_2Te_3 up to 30 mol%. The fabrication of these glasses with an open system led to a loss in mass of 10%, which is considerably higher than Ga_2Se_3 and modifies the composition of the final sample. However, this work was useful to study the effect of increasingly high amounts of Te to GLS. Four samples containing 5, 10, 20 and 30 mol% of Ga_2Te_3. Within these, glass formation was observed for the samples up to 10 mol%Ga_2Te_3, whilst formation of glass ceramics and full crystallisation was observed for 20 and 30 mol% Ga_2Te_3, respectively.

The Raman spectrum for the sample containing 10 mol% Ga_2Te_3 was compared to the sample containing 20 mol% Ga_2Se_3 (Figure 10). As a result, the addition of tellurium shifted the band at 230cm^{-1} towards lower wavenumbers even for a smaller degree of substitution. However, due to the larger content of Ga_2S_3, this sample exhibit a higher intensity for the band centred at 330 cm^{-1}. The peaks of the spectrum are broad and does not present any sharp feature, indicating the amorphous nature of the sample as confirmed by XRD. The glass formation of samples containing larger amounts of tellurium was weaker as the level of substituent was increased. This effect could be the result of the strong covalent character Ga_2Te_3 which can be balanced by La_2S_3 only for low concentrations. It could be possible to form glasses adjusting the Ga_2S_3/La_2S_3 ratio to counter balance the effect of tellurium. However, detailed studies necessitate the use of sealed systems to prevent the large losses of mass mainly due to the high vapour pressure of Te.
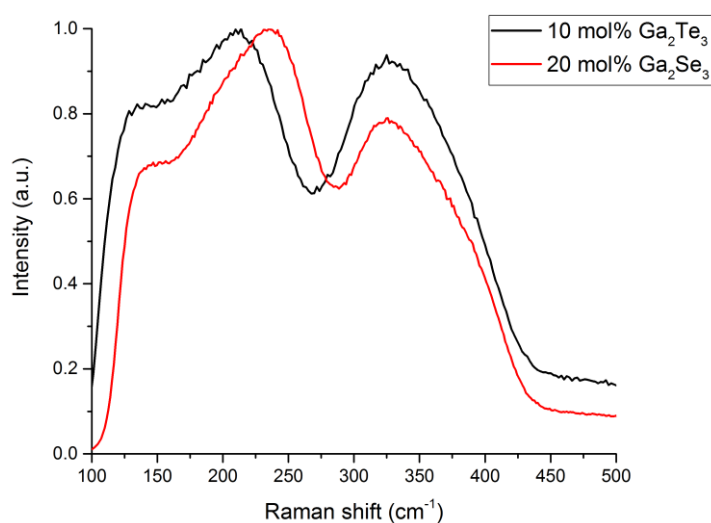
Figure 10: Comparison of Raman spectra for samples of Se-GLS and Te-GLS.

The substitution of gallium by indium was attempted replacing Ga_2S_3 by In_2S_3 in Se-GLS. Figure 11 shows the Raman spectra for samples containing up to 30 mol% In_2S_3. The samples showed broad peaks up to 20 mol% In_2S_3, while sharp features are predominant in the sample containing 30 mol% of In_2S_3. However, the nature of this sample could be glass ceramic since a peak corresponding to the T_g was found in the thermal characterisation (see Section 4.3). According to previous works, the sharp features may be due to the limited solubility of In_2Se_3 in the melt, leading to the formation of different phases when the melt was solidified. Indeed, studies on $Ge_xSe_{1-x-y}In_y$ glass demonstrated the formation of In_2Se_3 clusters event at low concentrations of In about 8 mol%.[72] Other works on $In_x(Se_{0.75}Te_{0.25})_{100-x}$ (x = 0 – 10) also reported the propensity of the In-Se glass to form crystals. In addition, the crystallisation of Se-Te was reported to have an activation energy even lower than In-Se.[73] Therefore, the simultaneous introduction of Se and Te in GLS glass may not lead to the formation of glasses.
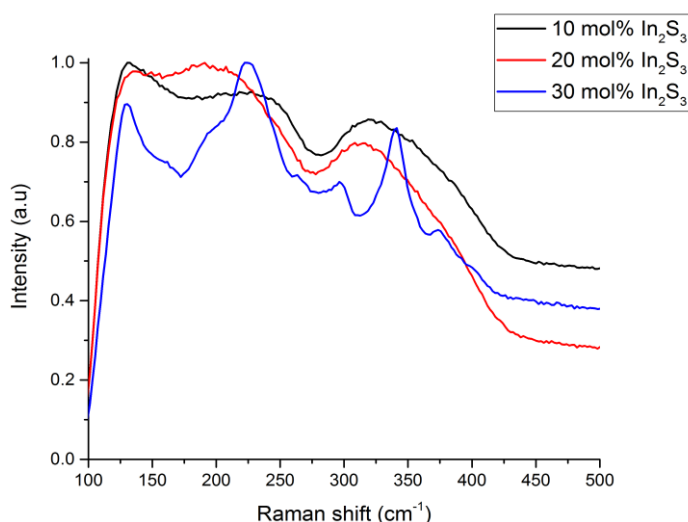
Figure 11: Raman spectra of samples containing In_2S_3.

The effect of CsCl in GLSSe glass was investigated by replacement of La_2S_3 with the halide. In general, the addition of alkali halides to glasses is carried out to increase the width of the transmission window. For instance, glass formation in CsCl-GLS was demonstrated aiming to form a stable multispectral material.[74] Other chalco-halide glasses such as Ga_2S_3-GeS_2-CsCl glass were studied aiming to expand the transmission window of Ga_2S_3-GeS_2 over shorter wavelengths.[75] It must be considered that alkali halides results in samples that are hygroscopic, increasing the level of OH^- in the glass. As a result, the optical attenuation of OH^- at 3 μm increases which could make the sample unusable in the IR region.

A quantity of 10 mol% CsCl was added to samples containing 20 mol% and 40 mol% Ga_2Se_3. For both compositions it was not possible to measure any meaningful transmission spectrum probably due to the large amount of particles. The formation of particles in the produced samples

may be due to an insufficient quenching rate. The crystallisation mechanism of CsCl in chalcogenide glasses has been reported for the system GeS_2-Sb_2S_3.[61] The glass in the homogeneous form consisted of Cs^+ bonded to sulphur and Cl^- ions bonded to Ge and Sb. The crystallisation of CsCl was activated at a temperature of 290 ^oC at which Cs^+ and Cl^- were recombined and Ge-S and Sb-S bonds formed the glass network. This description supports the hypothesis of an insufficient quenching rate during the fabrication of CsCl-GLSSe. Indeed, the cooling rate decreases as the temperature of the sample approaches room temperature. The quenching rate may have been excessively slow so that the crystallisation of CsCl was not avoided.

2.5   Conclusions

The manufacture of GLS glass with compounds to form novel compositions has been described. The melting apparatus employed consisted of an open system suitable for melting chalcogenide glasses from mixtures of high melting precursors. Such precursors were high purity compounds composed of chalcogens and metal or semiconductors (i.e. La_2S_3, Ga_2S_3, etc.). The modification of GLS glass was attempted following different routes.

Firstly, the substitution of sulphur by heavier chalcogens was studied substituting Ga_2S_3 by Ga_2Se_3 and Ga_2Te_3. The addition of Se resulted in a larger glass formation than the addition of Te. In fact, the introduction of Ga_2Se_3 was possible up to complete replacement of Ga_2S_3 in samples with composition 70 mol% Ga_2Ch_3 - 30mol% La_2S_3 (Ch = S, Se). For this glass forming system, the modification of the Ga_2S_3/La_2S_3 ratio produced a small number of fully amorphous samples which indicated that 30 mol% La_2S_3 was the optimal concentration. The addition of Ga_2Te_3 exhibited a loss in mass of 10% during the melt-quench. Thus, the concentration of Te was not known in the samples. However, for samples nominally containing over 10 mol% of Ga_2Te_3 crystallisation was observed. These results can be useful for future studies on this family of glasses which necessitate of a sealed system.

The second study route was focused on the substitution of Ga by In in Se-GLS. For this study, In_2S_3 was added replacing Ga_2S_3. As a result, only 20 mol% of Ga_2S_3 could be replaced in order to form a fully glassy sample. The phase separation may have occurred due to the lack of solubility of In_2S_3 in Ga_2S_3 and the strong tendency to crystallise of In-Se forming In_2Se_3.

The third route was focused on the substitution of La_2S_3 for CsCl. As a result, all the samples contained a large amount of particles making the samples opaque within the whole visible to IR range. Further studies may be addressed to attempt the introduction of other compounds such as NaCl or Na_2S as reported in previous studies.[76]

The results obtained on the glass fabrication and glass formation demonstrated the possibility of producing selenide glasses using open systems with low losses in mass during melting. The system is particularly advantageous in terms of safety and ease of fabrication with respect of sealed systems, which often result in explosions. The chemistry of the precursors must be chosen to satisfy the requirements of high melting point and vapour pressure. Future work could focus on the improvement of the manufacture process described above in order to improve the quality of the precursors and the glasses. In addition, systems reaching higher quenching rates could show expanded glass forming regions for the Se and In materials.

Chalcogenide glasses manufacture

Chapter 3

Optical characterisation

In this chapter, the optical properties of modified-GLS glasses are described including the transmission window and the refractive index (n) in the visible to LWIR region (0.5 to 20μm), the THz range (0.3 to 3 THz, corresponding to 100μm and 1mm in wavelength), the non-linear refractive index (n_2) and dn/dT. Generally, upon a change in composition of a given glass, the optical and dielectric properties of the new material can be predicted from the fundamental properties of the elements such as the bonding type, bond strength and polarizability of the individual elements. Although this approach could be simplistic, it can be used to qualitatively make predictions on the properties of the materials.

Firstly, the type of bonding within the atoms in the glass defines the value of the band gap and position of the electronic edge in the transmission spectrum. The bonding type can be predicted from the difference in electronegativity between anions and cations measured on the Pauling's scale. In particular, ionic bonds are formed when the difference in electronegativity is greater than 1.7, whilst covalent bonds are formed for lower values. The difference in electronegativity is proportional to the value of band gap, which is large for ionic solids and lower for covalent solids. This aspect explains the difference in bandgap between oxide and chalcogenide glasses and the limited transmission of the latter in the visible spectrum.[77], [78] In order to extend the transparency of chalcogenides further into the visible range, ionic compounds such as Na_2S and CsCl can be added to the melt.[28], [75], [76] However, alkali metals are well known to be hygroscopic, thereby compromising the IR transparency and causing in some cases the devitrification of the sample. Lanthanum sulphide can be used to effectively tackle the issue combining an ionic character to a low affinity to moisture. In GLS glass, La_2S_3 determines the position of the optical band gap at around 500nm.[29] The addition of the more ionic La_2O_3 and LaF_3 increased the value of the bandgap moving the electronic edge towards shorter wavelengths.[79], [80]

Secondly, the bond strength is a key property to understand IR spectroscopy of glass. In this spectral range, the absorption bands occur as a result of light absorption exciting molecular vibrations (Section 3.1.2). The chemical bond emulates the role of a spring connecting two spheres. The bond strength can be seen as the spring constant, hence proportional to the energy required to provoke the vibration. Therefore, the bond energy is proportional to the energy of the light absorbed. In addition, multiple vibration can be excited as optical phonons determining the

43

occurrence of the multiphonon edge. In general, the substitution of a given element with a heavier one leads to weaker bonds, lower phonon energy and improved transmission in the IR region.[81] These principles explain the opacity in the IR of the oxide glasses and the transparency of chalcogenide in this range. Thirdly, the polarizability of each atom in the material can account for the dielectric properties such as the refractive index and the dielectric constant. The polarizability is defined as the capability of an ion to form instantaneous electric dipoles. According to the frequency of the radiation interacting with a material, the total molecular polarizability derives from different contributions.[82] In particular, the electronic polarizability arise from the displacement of electrons by UV-visible and near IR radiations causing a disruption of the local distribution of the charges. Analogously, the ionic polarizability involves the displacement of ions and can be caused by LWIR and THz radiation. Predictions on the optical properties of glasses can be made considering the trend of polarisability across the periodic table. Particularly, the polarisability of atoms tend to decrease along the periods of the periodic table (left to right) and to increase along the groups (top to bottom).[83] With knowledge of the polarisability, it is easy to explain why the refractive index of chalcogenide glasses is much higher than that of silica. For example, in this work the refractive index of Se-GLS to be larger than regular GLS due to the higher polarisability of Se with respect to S. However, larger effects can be achieved by substituting La, which is the most polarizable element in GLS-based glasses. Therefore, to tailor the properties of the glass, the effect of a given component on bandgap, phonon energy and refractive index must be taken into account while substituting the components of a glass forming system.

Table 2: Range of the transmission windows for some glasses

Glass	UV-Visible cut-off (μm)	Multiphonon edge (μm)	Reference
Silica	0.19	3.5	[84]
AsS	0.62	11.5	[85]
AsSe	0.85	17.5	[85]
$Ge_{21}Te_{76}Se_3$	2.00	20	[85]
$Ge_{25}As_{15}Se_{60}$	0.78	15.40	[86]
$Ga_5Ge_{25}As_{15}Se_{60}$	0.96	15.67	[86]
Ge-Sb-S	0.64	11.00	[85]
As-Se-Te	2.00	16.00	[85]
GLS	0.50	13.4	[67]
$La_2O_3 - GLS$	0.47	11.8	[87]
$LaF_3 - GLS$	0.50	11.9	[88]
$CsCl - GLS$	0.41	-	[74]

In GLS glass, the presence of ionic La_2S_3 in a covalent matrix of Ga_2S_3 results in a large transmission window ranging from visible to LWIR. The addition of Se, Te and In to the glass aimed to expand the transmission window of the glass towards longer wavelengths as a result of the reduced phonon energy. The substitution was expected to have the effect of reducing the bandgap and increasing the refractive index as heavier elements were increasingly added. As a result, it was observed that the visible transparency of the glass decreased but it was not completely obscured whilst the multiphonon edge shifted towards 16μm. These results represent one of the few reported multispectral materials that can cover such a large spectral range. Amongst the commercially available chalcogenide glasses, As_2S_3 is the material that includes both visible and LWIR transmission from 0.6 to 12μm. Other materials are still under development from a laboratory readiness level. Recently a Ga_2S_3-GeS_2-CsCl glass has been reported with a transmission window ranging from 0.5 to 12 μm.[75] However, the comparison between this material and the regular Ga_2S_3-GeS_2 glass brings up some of the disadvantages of CsCl. In particular, the water absorption obscuring some of the IR bands and oxidising the material with subsequent emission of H_2S.[89] These materials were used to benchmark the key optical properties in order to compare the performance of the glass and plan future works on the improvement of the material.

3.1 Mechanism of light attenuation in transparent media

3.1.1 Intrinsic factors

The physical phenomena causing light attenuation due to the intrinsic properties of the material are those determining the width of the transmission window. At short wavelengths, the electronic edge limits the transparency as a result of the band gap absorption, whereas at long wavelength the multiphonon edge occurs from light exciting optical phonons.

In the ideal case, the electronic edge is a sharp delimitation corresponding to the energy of the transition of an electron from the highest energy state of the valence band to the lowest energy state in the conduction band.[33] As a result, the interaction produces an electron-hole pair and the photon is absorbed. The pair is then recombined through a non-radiative phonon assisted steps.[90] In amorphous materials, deviations from the ideal case are caused by the structural disorder giving additional contribution to the electronic absorption. The disorder can result in a perturbation of the band structure, causing the localisation of the density of states in the bandgap. For this reason, the electronic edge assumes the shape of a tail, also known as Urbach tail, mathematically described as:[91]

$$\alpha_{bg} = A e^{g(h\nu - h\nu_0)}$$
Equation 9

where h is the Planck's constant, ν is the energy of the incident photon, A, g and ν_0 are material-dependent fitting parameters. A third factor contributing to the electronic edge is commonly observed in amorphous semiconductors. It arises from topological imperfections within the material such as homonuclear bonds (e.g. $S-S$ bond) or impurities producing a weak absorption over an elongated spectral range. This effect is known as "weak absorption tail" and it is strictly dependent on the fabrication process.[92]

In theLWIR, the intrinsic absorption of the material is caused by a multiphonon mechanisms.[90] A phonon is a discrete quantum of vibrations describing the energy relative to a given molecular vibration.[93] Phonons can be seen as a collective movement of atoms moving out of their equilibrium position in the lattice. Acoustic phonons occur if the atoms move in-phase (i.e. along the propagation direction) resembling the propagation of acoustic waves in air. Optical phonons are out-of-phase movements and are excited by IR radiations. The combination of multiple phonons is responsible for the opacity of materials in the infrared region and for the tailed shape of the edge. Glasses with a low phonon energy such as chalcogenides can transmit at longer wavelengths than oxides, due to the combination of heavier atoms and weaker chemical bonds.

Mathematically, these factors contribute to the absorption coefficient as:[33]

$$\alpha_{mp} = Be^{-\frac{b}{\lambda}}$$ Equation 10

$$b \propto \left(\frac{\mu}{F}\right)^{1/2}$$ Equation 11

where μ is the reduced mass of the oscillator and F is the electrostatic force constant related to the bond strength. Materials with heavy atoms and low force constant (i.e. oxides > sulphides > selenides > tellurides)are characterised by a low value of the factor b leading to $\alpha_{mp} \cong B$, which represents the theoretical minimum loss due to multiphonon excitation.

The phonon energy of materials can be determined with Raman spectroscopy and has an important role in the prediction of non-radiative phenomena and other non-radiative energy transfers in rare earth-doped glasses. It also has relevance in several thermal properties such as the specific heat capacity and thermal conductivity.[94]–[96]

Signal losses due to Rayleigh scattering arise from the fluctuation of relative permittivity within the material. These fluctuations can be caused by changes in local concentration of a given component, change in density and the presence of particles. Thus, scattering is a significant source of losses in homogeneous glasses and optical fibres. The local compositional inhomogeneity is related to the fictive temperature of the glass which can be changed annealing the glass at different temperatures. The decrease of the fictive temperature towards values close to the T_g of the glass was found to reduce the scattering losses.[97] The impact of the density fluctuation, α_d, can be estimated as:[98]

$$\alpha_d (cm^{-1}) = \frac{8\pi^3}{3\lambda^4} n^8 p^2 \beta_c K_B T_g$$ Equation 12

where λ is the wavelength of the incident radiation, n is the refractive index of the material, p is the photo-elastic coefficient, βc is the isothermal compressibility at T_g, K_B is the Boltzmann constant and T_g is used as approximation of the fictive temperature. On the other hand, the scattering caused by changes in local composition, α_c, can be estimated as:[99]

$$\alpha_c (cm^{-1}) = \frac{32\pi^3 MW}{3\lambda^4 N\rho} \left(\frac{\delta\varepsilon}{\delta c_i} - \frac{\delta\varepsilon}{\delta c_m}\right)^2 \left(\frac{c_i + c_m}{c_i c_m} - \frac{2zW}{K_B T}\right)^{-1}$$ Equation 13

where MW is the average molecular weight of the glass, N is the Avogadro's number, ρ is the density of the glass, ε is the dielectric constant of the glass, c_i is the concentration of the ith component defined as the molar ratio $c_i = \frac{n_i}{n_{tot}}$, z is the coordination number of the component in the system and W is the heat of formation of the glass.

3.1.2 Extrinsic factors

The group of extrinsic sources of attenuation includes all the contributions coming from contaminants, topological defects and particles causing absorption or scattering of light. The spectral region subjected to attenuation varies according to the phenomenon causing loss of signal. The absorption peaks of rare earth ions are widely distributed from middle IR to UV. The ions absorb light undergoing a f-f electronic transition (Chapter 5) characterised by a weak dependency on the crystal field. Therefore, the attenuation is located within relatively fixed spectral bands.[100], [101] However, it should be noted that hypersensitive transitions in rare earths can have large variations in intensity and a blue or red shift according to the chemistry of the host. On the other hand, the absorption bands of transition metals heavily depend on the host and the symmetry of the crystal field. In disordered materials, the absorption of transition metals can be extended over a large range affecting dramatically the transparency.[33] The improvements made to the melting system prior to this work confirmed the impact of transition metals on the optical properties of the glass. In particular, the addition of filters on the argon line improved the purity of the glass eliminating a substantial amount of chromium coming from the gas pipes. As a result, the transparency of the glass in the visible region was extended and the loss within the transmission window decreased.
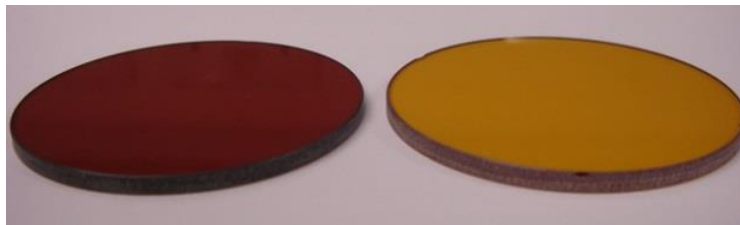
Figure 12: GLS glass produced before (left) and after (right) the installation of gas filters.[102]

Light absorption in the IR region is mainly observed due to molecular vibrations. Impurities such as H_2O, OH and SH cause absorption in the IR range (Table 2: Range of the transmission windows for some glasses) undergoing bond stretching and bending upon interaction with infrared light.[103] The quantum mechanical description of this phenomenon considers the molecule as a single particle being of mass µ corresponding to:

$$\frac{1}{\mu} = \sum_n \frac{1}{m_n}$$

Equation 14

where µ is the reduced mass and m_n is the mass of each atom of the molecule. The absorption occurs when the displacement changes dipole momentum of the molecule following an anharmonic potential energy curve from which the energy of the transition can be calculated as:

$$E = h\omega_e \left(v + \frac{1}{2}\right) - h\omega_e x_e \left(v + \frac{1}{2}\right)^2 + \cdots \qquad \text{Equation 15}$$

$$\omega_e = \frac{1}{2\pi c}\left(\frac{K}{\mu}\right)^{1/2} \qquad \text{Equation 16}$$

where h is the Planck's constant, ω_e is the wavenumber of the vibration, $\omega_e x_e$ is a anharmonicity constant, υ is the vibrational quantum number and K is the force constant of the vibration. The selection rule for molecular vibrations is $\Delta\upsilon = \pm 1$, although transitions with larger $\Delta\upsilon$ called overtones are observed due to the anharmonicity of the vibration. Generally, the first two terms of Equation 16 are sufficient to accurately describe the energy of the vibration.[103]
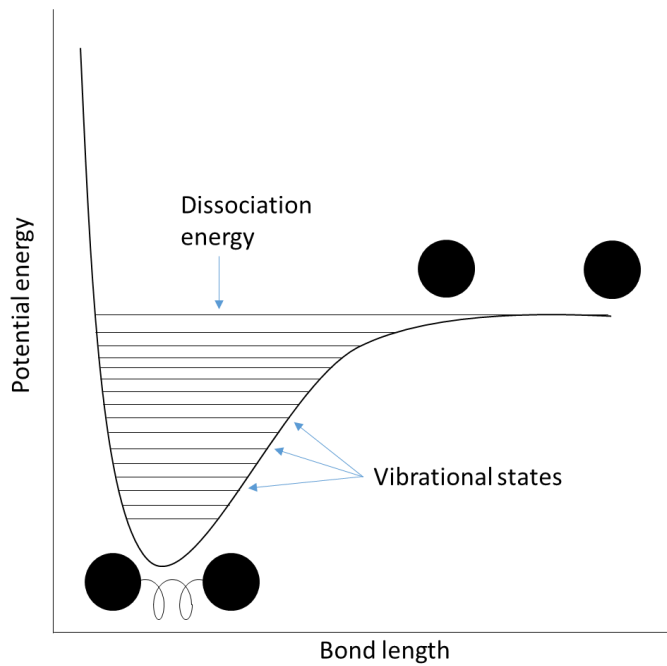
Figure 13: Graphical representation of the anharmonic potential energy curve describing molecule vibrational states.

The scattering of light by crystalline particles depends on the size of the particle and the refractive indices of the particle and the glass.[104] A relative refractive index can be defined as $m = \frac{n_p}{n_g}$, where n_p and n_g are the refractive indices of the particles and the glass, respectively. Similarly, a relative size of the particles can be defined as $x = \frac{2\pi r n_p}{\lambda}$, where r is the radius of the particle. For small particles, the scattering efficiency parameter, Q, follows a Rayleigh regime and can be calculated as:

$$Q = \frac{8}{3}x^4 \frac{(m^2 - 1)^2}{(m^2 + 2)^2} \qquad \text{Equation 17}$$

The growth of particles can be avoided providing the glass melt with appropriate homogenisation arrangements and quenching at a fast cooling rate. These aspects are crucial since crystals may not be dissolved by simply heating the glass during the fabrication of optical components. In addition to optical attenuation, the presence of particles can cause fractures during the machining of the glass and the finished component. However, crystals can have beneficial effects to the mechanical properties if grown appropriately like in the case of glass ceramics reaching superior performances than basal and granite.[105] Since the optical properties of the glasses were of upmost interest, the formation of crystals was unwanted and the glasses containing particles were not considered for optical applications.

3.2 Techniques of characterisation

3.2.1 Transmission and reflection spectra

The transmission spectra of polished samples were measured combining the plots obtained by a Varian 670 FTIR between 1667nm to 25000nm, and a Cary 50 UV-Visible spectrometer between 200 and 1700nm. For both instruments, the measurements required a background run (i.e. no sample in the spectrometer) and sample run. The final spectrum resulted from the subtraction of the background from the sample run. Furthermore, the FTIR measurements were carried out in a nitrogen atmosphere to eliminate the absorption caused by CO_2 and moisture. From the measurement of samples with different thickness, the attenuation coefficient α could be calculated as:[33]

$$\alpha \ (cm^{-1}) = \frac{-ln\left(\frac{I}{I_0}\right)}{t}$$

Equation 18

where I is the intensity of the signal though the thick sample, I_0 is the signal through the thin sample and t is the difference in thickness between the two samples. This method was employed to recognise impurities and normalise the intrinsic loss of the material by the thickness. The attenuation coefficient for the OH impurity for different compositions was compared to observe any trend in the concentration as the concentration of the precursors was varied. This approach should reveal whether the presence of OH and oxide-related impurities is strictly due to the quality of the initial precursors or if the melting system was not optimally set up.

For the measurement of high temperature transmission and reflection spectra a Nicolet 6700 FTIR equipped with a high temperature cell was used (Figure 14a). The reflectance spectra were measured for an angle of incidence close to 90° for which an ad-hoc apparatus was designed (Figure 14b). The high temperature cell was inserted in the spectrometer sacrificing the purge of

the sample chamber. Hence the presence of strong CO_2 and H_2O peaks in the spectra becoming more significant as the temperature increased. The procedure to calculate n and k was followed as described elsewhere.[106] The sample with composition 20 mol% Ga_2Se_3 - 50 mol% Ga_2S_3 - 30 mol% La_2S_3 was the only Se-GLS glass analysed within the framework of the collaborative work with Qinetiq Inc.

A
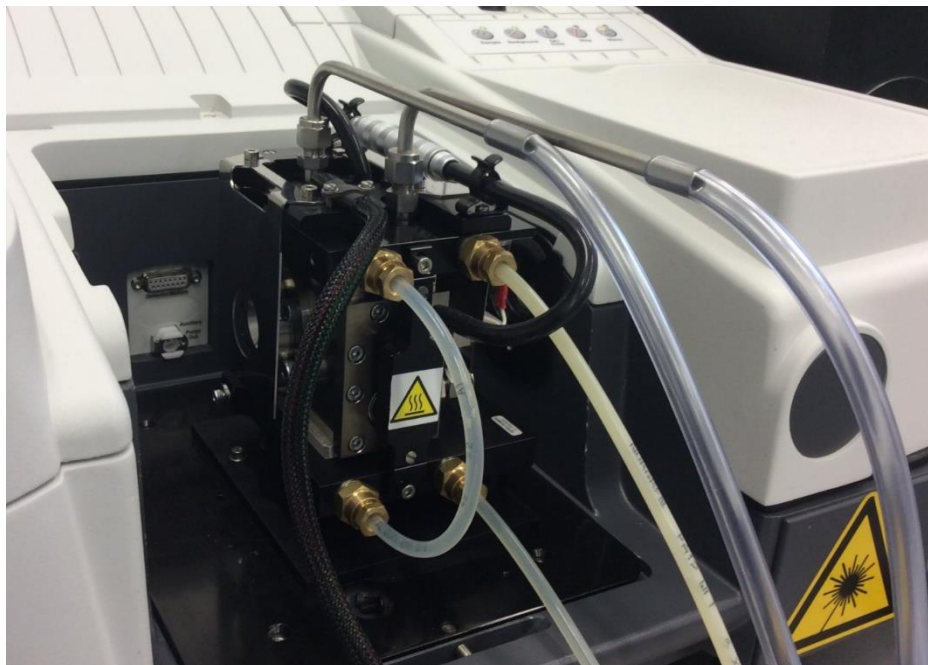
B
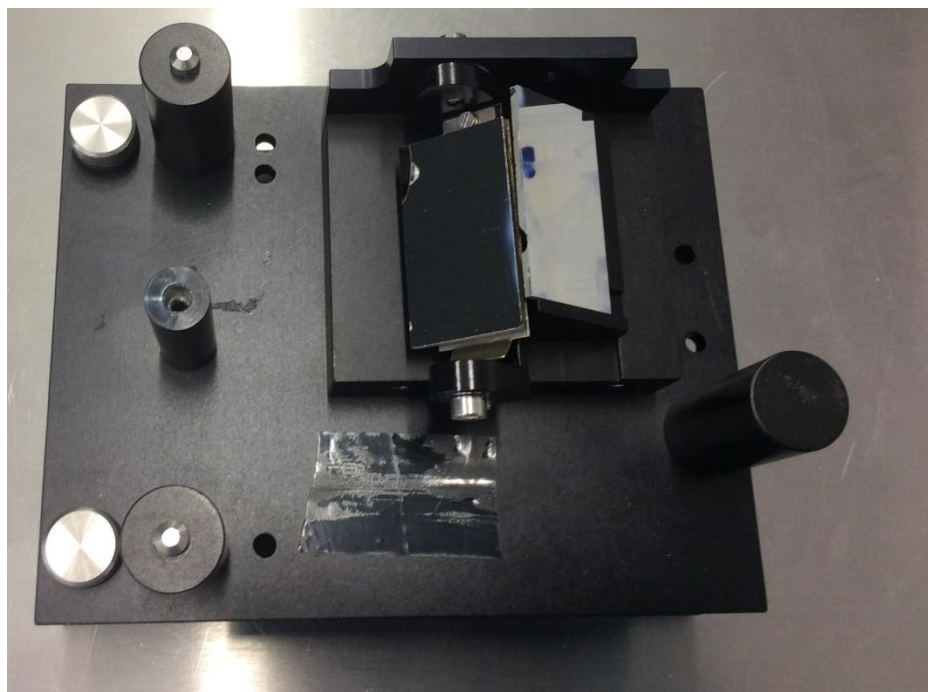
Figure 14: (A) Heating cell adopted for transmission measurements; (B) Apparatus for reflectance measurements. In this configuration, the heating cell was laying on top of this apparatus.

3.2.2   Determination of the linear and non-linear refractive index

Measurement of the refractive index was carried out to probe the effect of different substituents and components on GLS glass. It is a routine analysis for optical materials to assess the quality and the suitability for optical applications. The determination of the refractive index dispersion for the samples under investigation was carried out combining the results obtained by ellipsometry and prism coupling.

The dispersion curve of the refractive indices was obtained with a Woollam M-2000 ellipsometer over a range of wavelengths between 0.193 and 1.690μm. Ellipsometry probes the change in polarization of a beam of light reflected from the surface of a sample. The ratio between the horizontal (R_h) and vertical (R_v) components of the polarisation is used to determine the ellipsometric angles Δ and Ψ as:[107]

$$\rho = \frac{R_h}{R_v} = \tan(\Psi)\, e^{i\Delta}$$

Equation 19

The ellipsometric angles are related to the complex refractive index $\tilde{n}(\lambda)$ following the equation:

$$\tilde{n}(\lambda) = \frac{[1 - 4sin^2(\theta_0)\tan(\Psi)\,e^{i\Delta} + 2\tan(\Psi)\,e^{i\Delta} + \tan^2(\Psi)\,e^{i\Delta}]^{1/2}\,\tilde{n}_0 \sin(\theta_0)}{\cos(\theta_0)\,[1 + \tan(\Psi)\,e^{i\Delta}]} = n(\lambda) + ik(\lambda)$$

Equation 20

where ϑ_0 is the incident angle and $\tilde{n}_0$ is the refractive index of the air. The real part of $\tilde{n}$ represents the real refractive index $n(\lambda)$ while the imaginary part gives the value of the extinction coefficient $k(\lambda)$.[107]

The data measured between the electronic edge and 1.7 μm was then fitted to the Sellmeier equation in the form:[108]

$$n(\lambda)^2 = \frac{A\lambda^2}{\lambda^2 - A_1} + \frac{B\lambda^2}{\lambda^2 - B_1} + \frac{C\lambda^2}{\lambda^2 - C_1} + 1$$

Equation 21

where n(λ) is the refractive index at a given wavelength, A, A_1, B, B_1, C, C_1 are fitting parameters. The parameters were fitted with the least squares method. The determination of the fitting parameters allowed to predict the refractive index at wavelengths longer than 1.7μm.

The use of ellipsometry for the determination of optical constants in bulk samples produces accurate results if the surface is not rough and not oxidised. In the case of GLS-based glasses, the presence of La leads to a quick oxidation of the surface from which a passivation effect is observed. Therefore, the results found deviated from the expected values being underestimated. To compensate for this underestimation, the curves were normalised to the value of refractive

index found with a Metricon 2010/M prism coupler at 1550 nm and the accompanying software. In the prism coupling technique, the polished surface of the sample is kept in contact with the surface of a prism. A laser beam with a wavelength of 1550 nm is then shone on the prism with a given incident angle θ. The beam is then reflected from the surface of the prism in contact with the sample reaching the detector. The sample is then rotated changing the incident angle until the critical angle θ_c is found. In this condition, some of the modes of the incident beam leak from the prism to the sample resulting in a sudden drop of the signal at the detector. From the value of θ_c, the software was employed to calculate the value of the refractive index.
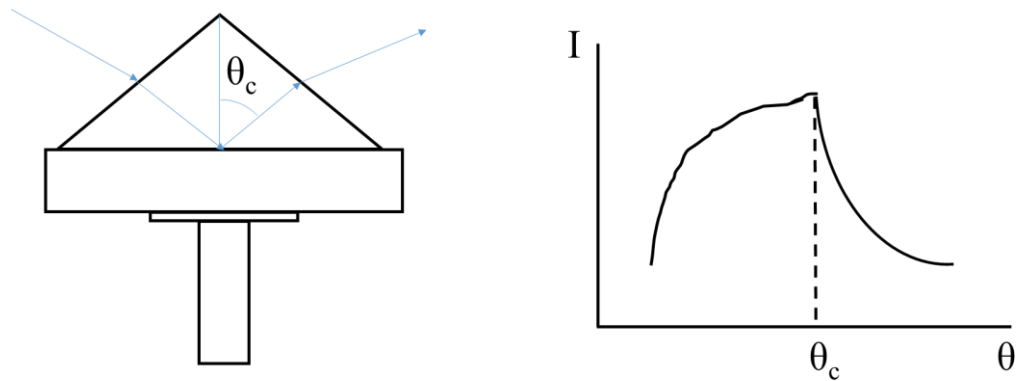
Figure 15: Principles of the prism coupling technique

The determination of the non-linear refractive index n_2 was carried out with the setup provided by Heriot-Watt University shown in Figure 16.[109] A tuneable source optical parametric amplifier (OPA – Spectra Physics) was pumped by a Ti:Sapphire pump laser emitting 100 fs pulses with 1 mJ pulse energy at a 1 kHz repetition rate. The OPA output wavelength range was between 1.2-2.4 µm. A spatial filter was used to provide a Gaussian beam profile for the Z scans. A reflective ND filter was used to attenuate the input pulse energy monitored by a power meter recording the average power of the beam. The sample was translated parallel to the focused beam axis (Z axis) and the intensity was measured as a function of the position. Three detectors capture coincident readings which allow for simultaneous measurement of the samples n_2 (closed aperture, D2) and nonlinear absorption coefficient (open aperture, D3) corrected for laser pulse to pulse variations (reference, D1). The samples investigated were expected to have a positive non-linear refractive index.[109] Therefore, as the sample translated from the component L3 towards the focal point a drop in signal followed by an increase was expected as a result of the initial defocussing followed by beam collimation.[110]

Data analysis of the experimental results was performed following the procedure outlined by Sheik-Bahae et al and reported elsewhere.[109], [111] The normalised transmittance through the closed aperture (component D3, Figure 16) was fitted to the equation:

$$T(z, \Delta\Phi_o) = 1 + \frac{4x\Delta\Phi_o(1-S)^{0.25}}{(x^2+9)(x^2+1)}$$

<div align="right">Equation 22</div>

where

$$x = \frac{z - zoffset}{z_0}$$

<div align="right">Equation 23</div>

$$\Delta\Phi_o = \frac{2\pi L n_2 I_0}{\lambda\sqrt{2}}$$

<div align="right">Equation 24</div>

$\Delta\Phi_0$ is the change in phase of the incident beam after the sample from which the value of n_2 can be calculated, L is the sample thickness, λ is the wavelength of incident laser beam, S is aperture (Iris) linear transmittance; z offset is the offset of centre of Z scan feature (i.e. beam focus) from 0 position of stages and I_0 is the intensity at focus.
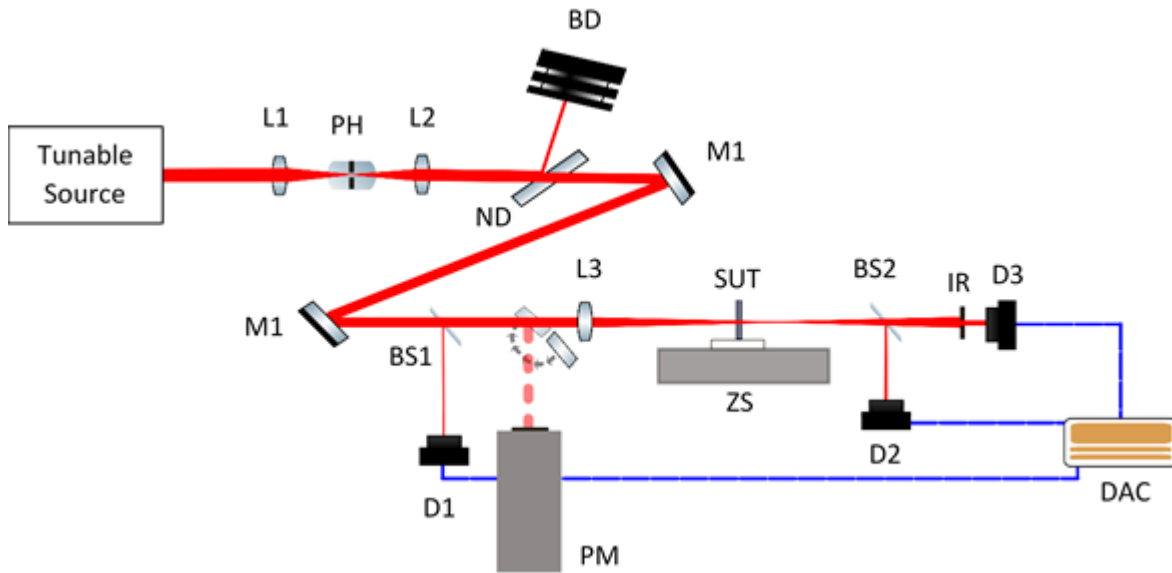
Figure 16: Z-scan setup used for experiment. Lx – lens, PH – pin hole (spatial filter), ND – reflective variable neutral density filter, Mx – mirror, BSx – beam splitter, D1 – reference detector, PM – power meter, SUT – sample under test, ZS – Z stage, D2 – open aperture detector, IR – iris, D3 - Closed aperture detector, DAC – data acquisition and control. Picture printed with the permission of Prof. Ajoy Kar, Dr. Mark Mackenzie and Dr. James Morris.

3.2.3   Terahertz time-domain spectroscopy

The refractive index and absorption coefficient in the terahertz region of GLS and Se-GLS were measured along with other commercial chalcogenide glasses, namely IG2 and IG5 produced by Vitron GmbH. For this study, a laboratory-built setup was provided by the National Physical Laboratories (NPL). It included a Ti:Sapphire femtosecond laser, four off-axis parabolic mirrors, a biased GaAs emitter, and electro-optic detection with a ZnTe crystal and balanced Si photodiodes. A detailed description of the setup and of the data analysis can be found elsewhere.[112]

3.3   Results and discussion

3.3.1   Transmission and reflection spectra

The measured transmission windows for the selenide samples were carried out on flats of 1mm in thickness against blank background. The effect of selenium on GLS glass was assessed examining the electronic edge and the IR edge. In particular, compositions with increasing concentration of Ga_2Se_3 and composition with fixed amount of Ga_2Se_3 ratio were compared. In the first case, the extent of improvement for incremental concentration of selenium was probed. In the second case the effect of La_2S_3/Ga_2S_3 variations were investigated. Figure 17 summarises the cut-off wavelengths in both visible and IR ranges in the format of a phase diagram to compare different compositions. The cut-off wavelength was determined as the wavelength at which the transmittance was 0%. Two main observations were made through this compositional analysis. Firstly, for increasingly high levels of Se, the transmission window shifted towards longer wavelengths. In particular, along the 30 mol% La_2S_3 tie-line the IR cut-off moved from 13.36 to 16.62 μm whilst the Visible cut-off moved from 494 to 575 nm. This observation was expected as a result of less energetic phonons and smaller value of bandgap associated with the substitution of S by Se. The retention of visible transmission was unexpected as the most of the selenide glasses studied in literature exhibit visible cut-off in the near-IR region except As_2Se_3, which is commercially produced with a transmission window from 0.90 to beyond 14 μm.[16] In addition, this observation was unexpected as other substitutions (Ga_2S_3 for Al_2S_3 and In_2S_3) were reported to cause dramatic shifts to the transmission window.[81] Other compositional studies in chalcogenide glasses reported the substitution of sulphur for selenium to result in an expansion of the IR edge and a shrinkage of visible edge of the same magnitude.[12], [53] The modest contraction of the transmission window observed for Se-GLS glasses could be due to the preservation of the ionic character of La_2S_3 despite the addition of Se. This behaviour suggests that La-Se bonds are not prominently formed as a consequence of the stronger bonds formed between La-S. Secondly, compositional changes across the 20 and 30 mol% Ga_2Se_3 tie-lines did

not have significant effects on any of the cut-off edges. Furthermore, the same behaviour was reported in the past in some compositional studies on GLS glasses (0 mol% Ga_2Se_3 tie-line).[67] This observation may suggest the S/Se ratio as the most important factor governing the optical properties.
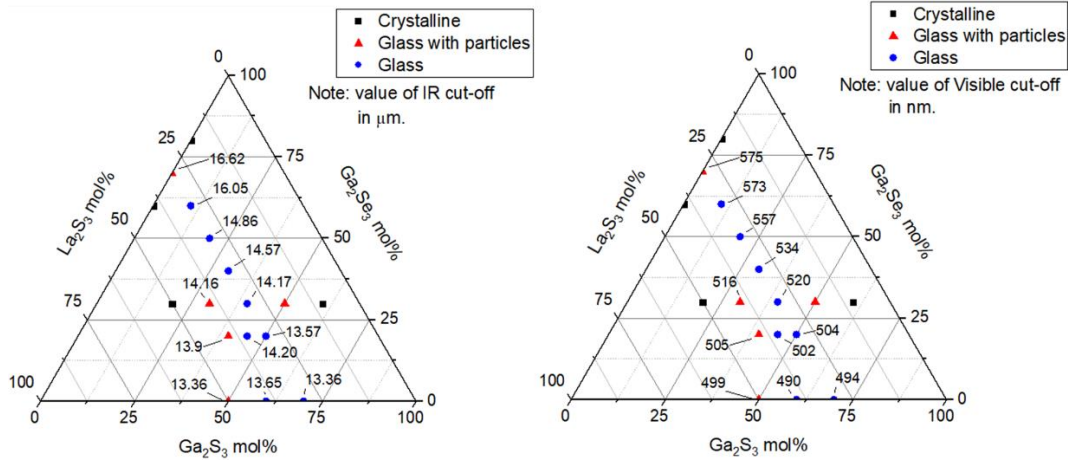
Figure 17: Compositional dependence of UV (left) and IR(right) cut-off edges.

Figure 18 depicts the transmission window for the compositions falling onto the 30 mol% La_2S_3, 20 and 30 mol% Ga_2Se_3 tie-lines, respectively. For clarity, some of the spectra have been omitted but the full collection of spectra can be found in Appendix B. Strong peaks at 8.6, 10.8 and 11.6 μm could be observed representing the residual impurities after the fabrication process. According to previous studies, the peaks at 10.8 and 11.6 μm are due to the presence of Se-O bonds in the glass.[113] The other peak at 8.6 μm was assigned to S-O vibration as reported in other studies.[52] This peak appeared to decrease in intensity as the concentration of Ga_2Se_3 increased and remains stable for a fixed amount of Ga_2Se_3. This effect was expected as the energy of the Ga-O bond is lower than the Se-O bond making Ga less likely to form bonds with oxygen during the melting stage.[57] The formation of further La-O bonds could not be proved since the vibrational ground state absorption is found within multiphonon edge of the samples at 21.64 μm.[55]
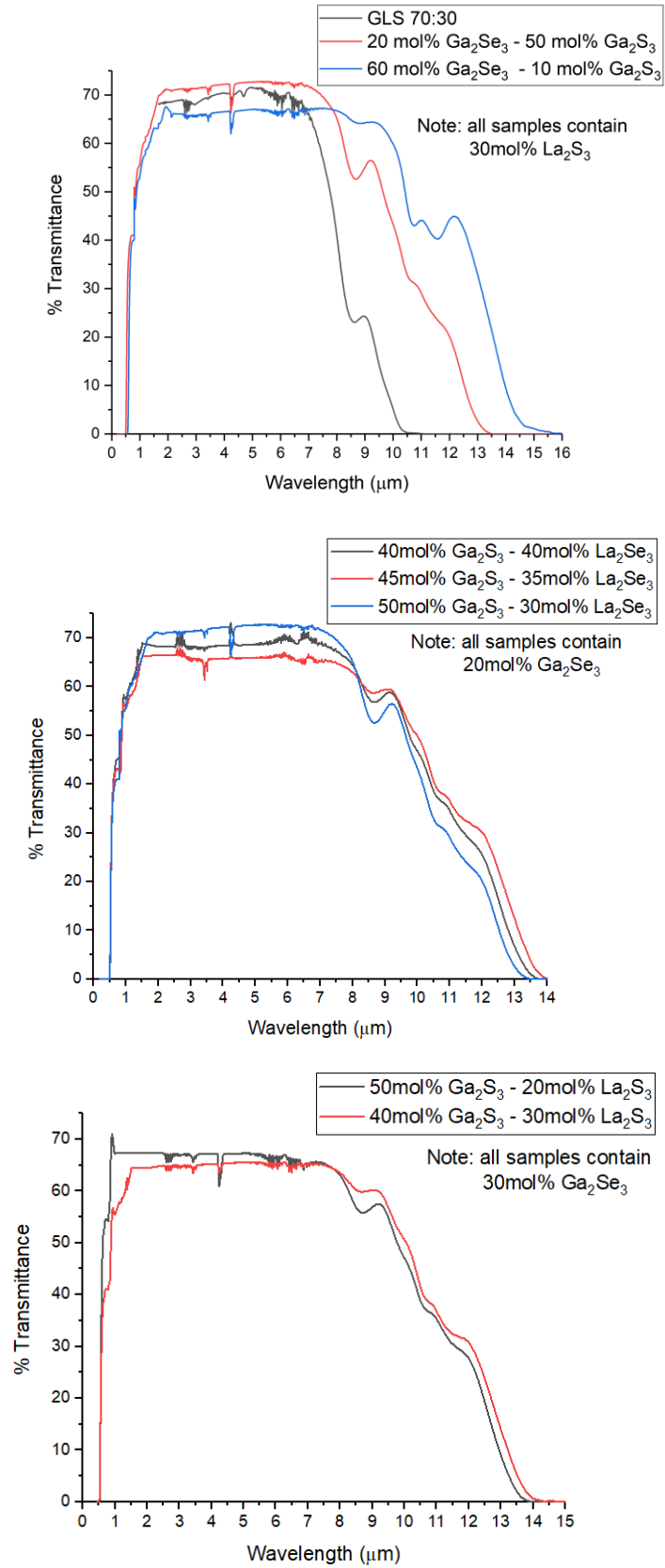
Figure 18: Transmission windows for samples containing 30 mol% La$_2$S$_3$ (top), 20 mol% Ga$_2$Se$_3$ (middle) and 30mol% Ga$_2$Se$_3$ (bottom). Curves are un-corrected for Fresnel reflections and scattering loss.

The presence of other impurities with a smaller impact can be observed within the 2–8 µm region. Particularly, the OH absorption peak is of particular interest since it falls around 1.90 and 2.92 µm and it can compromise the performance of the glass in fibre form. In addition, the absorption level of this peak can give hints on the presence of moisture during the fabrication process. The level of moisture within the melting system also promotes the increase in intensity of SH peaks between 2-4 µm. Carbon-based contaminations such as CO_2, CS_2 and CSe_2 vibrations predominantly derive from the crucibles used for the glass melts. A high level of these impurities results in absorption peaks in the 4-8 µm range and generally corresponds to the use of a vitreous crucible with surface damage. The absorption peaks of OH, SH and C-based impurities are shown Figure 19 where a magnified version of the transmission spectrum of the sample with composition 35 mol% Ga_2S_3-35 mol% Ga_2Se_3-30 mol% La_2S_3 is shown. The spectrum was registered with an FTIR spectrometer with a sample of 1 mm in thickness. The OH absorption peaks are the most prominent whilst the SH absorption peak was found to be very weak falling below the intrinsic absorption of the material. Within the carbon region, two peaks at 5.72 and 6.11 µm were observed. These peaks did not match with the absorption bands of impurities in other chalcogenide glasses, therefore the correct assignment of these bands requires further investigation. However, despite carbon impurities in chalcogenide glasses are not yet fully characterised, the spectral region between 4-8µm is known to confine the carbon absorption peaks.[56] From the spectrum below it can be concluded that the conditions of the carbon crucible were sufficiently good for glass melting and it did not release a measurable amount of carbon. Furthermore, the comparison of the absorption coefficient of the OH peak at 2.92 µm found in various glasses was carried out and results are shown in the inset of Figure 19. The intensity of the OH peaks was calculated from the FTIR spectra of 1 mm thick samples containing 30 mol% La_2S_3 without corrections for Fresnel reflection and scattering loss. The value of the OH peak intensity was calculated subtracting the baseline value to the peak value of absorption. The comparison suggested that the manufacturing process was repeatable leading to similar amounts of impurities.
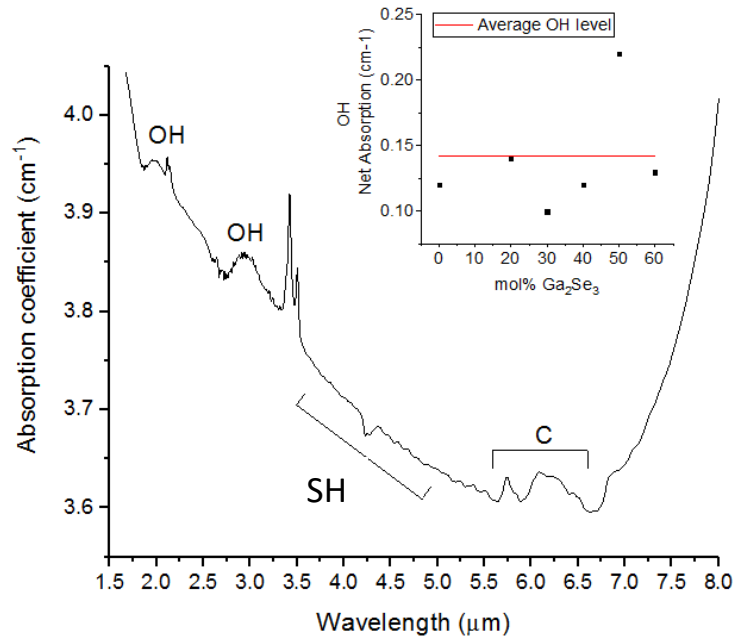
Figure 19: Absorption peaks founds in a sample with composition 35 mol% Ga_2S_3-35 mol% Ga_2Se_3-
30 mol% La_2S_3.The spectrum is not corrected for Fresnel reflection and scattering
loss.

The effect of selenium on the optical features was tested taking a series of pictures in both visible
range and thermal imaging range (8-14 μm) of a hot object seen through GLS and Se-added GLS.
As shown in Figure 20:, the selenide composition retains both LWIR and visible transparency while
regular GLS has a much limited transmission between 8-14 μm. The capability of Se-added GLS to
transmit over visible and thermal range may enable the future development of novel optical
components to integrate IR and visible imaging in a single solution.
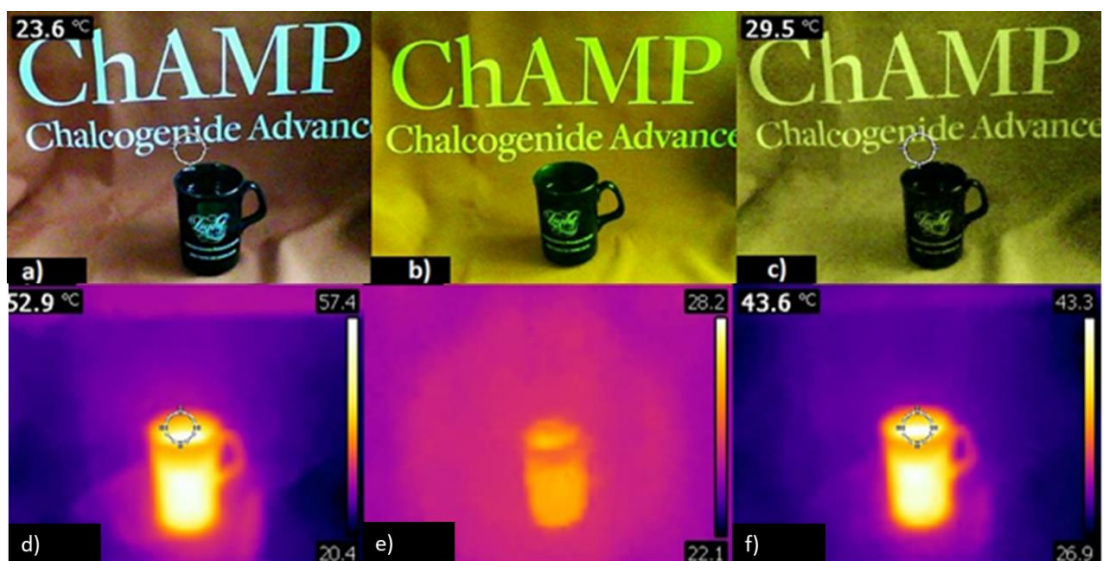
Figure 20: top row, visible range pictures with no filter (20a), Ga-La-S glass filter (20b) and 35
mol% Ga_2Se_3 sample filter (20c); bottom row, thermal pictures with no filter (20d),
Ga-La-S glass filter (20e) and 35 mol% Ga_2Se_3 sample filter (20f).

Further investigations were carried out on the samples containing Te and In. The impact on the optical properties of these elements resulted in a limited visible transmission even for small levels of substitution. The addition of 10 mol% Ga_2Te_3 to GLS glass moved the visible cut-off from 512 nm of regular GLS to 550 nm and 640 nm for 10 mol% In_2S_3. On the other hand, a small improvement in the IR transmission was also observed as shown in Figure 21. Particularly, the largest improvement was observed for the sample containing 10 mol% Ga_2Te_3 for which the IR cut-off moved by 500 nm clearing a larger portion of the 8-14 µm region. It is worth noting that these optical features exhibited by the samples with 10 mol% In_2S_3 and 10 mol% Ga_2Te_3 were comparable to those for the sample containing 20 mol% Ga_2Se_3. Furthermore, for concentrations of Te higher than

10 mol% the improvement of the IR transmission was found to be even more pronounced. The observation of similar improvements at a lower modifier level (i.e. 10 mol% Ga_2Te_3 against 20 mol% Ga_2Se_3) suggested that the addition of Te could push the IR cut-off even further than Se. Therefore, future works could tailor the manufacturing process to maximise the IR transmission of GLS-based glasses.
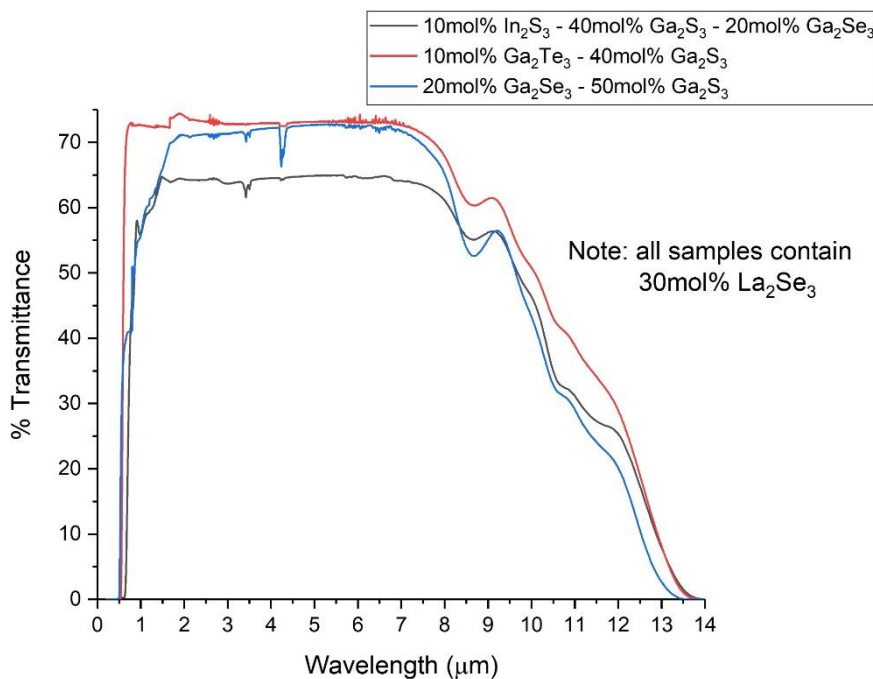
Figure 21: Transmission spectra for samples containing 10mol% In_2S_3 (thickness = 1.09mm), 10mol% Ga_2Te_3 (thickness = 0.77mm) and 10mol% Ga_2Se_3 (thickness = 1.11mm). Curves are un-corrected for Fresnel reflections.

3.3.2   T-depentent spectra and dn/dT

The spectra in transmission and reflection of a sample with composition
20 mol% Ga_2Se_3 - 50 mol% Ga_2S_3 - 30 mol% La_2S_3 are shown in Figure 22 and Figure 23. In both

cases the spectra were taken from a sample of 4mm in thickness which did not show substantial changes in the region between 2 to 5 μm. However, drastic worsening in the region between 7 to 12 μm was observed. This can be explained considering the mechanism of attenuation taking place in each region. In particular, the spectral range 2 - 5 μm is mainly affected by Rayleigh scattering and it does not undergo a dramatic increase in intensity at higher temperatures. For this reason, the transmission in this range was found almost unchanged. Furthermore, the fluctuation observed did not give raise to a consistent trend. On the other hand, the region 7 - 12 μm exhibited a clearer behaviour. In this region, the multiphonon absorprion is the main factor of attenuation and it strongly depended on the temperature of the experiment. It was observed that in this range both transmission and reflection decreased indicating an increase in light absorption. The measurements could be used to calculate accurately the dn/dT as reported in Table 3. The value of dn/dT was determined taking the values of the refractive index at each temperature and calculating the slope of the line best fitting the data points. The value found at 10.60 μm was significantly higher than that for other chalcogenides. However, it must be considered that the presence of the S-O, Se-O and Ga-O absorption peaks was detrimental to this measurement. Usually the experimental determination of dn/dT is carried out at cryogenic temperatures for wavelengths where the absorption coefficient is lower than 1 cm^{-1} at room temperature, expecting this value to decrease with the temperature.[114] Analogously, the determination of dn/dT at high temperatures would give accurate measurements if the absorption coefficient at the highest temperature was below 1 cm^{-1}. The absorption coefficient at 10.6 μm for the sample was calculated with Equation 18 resulting in 0.70 cm^{-1} at room temperature and 4.00 cm^{-1} at 500°C. This observation confirmed that the value calculated for Se-GLS was not accurate and that the content of oxides is limiting the performance of the glass at this wavelength.
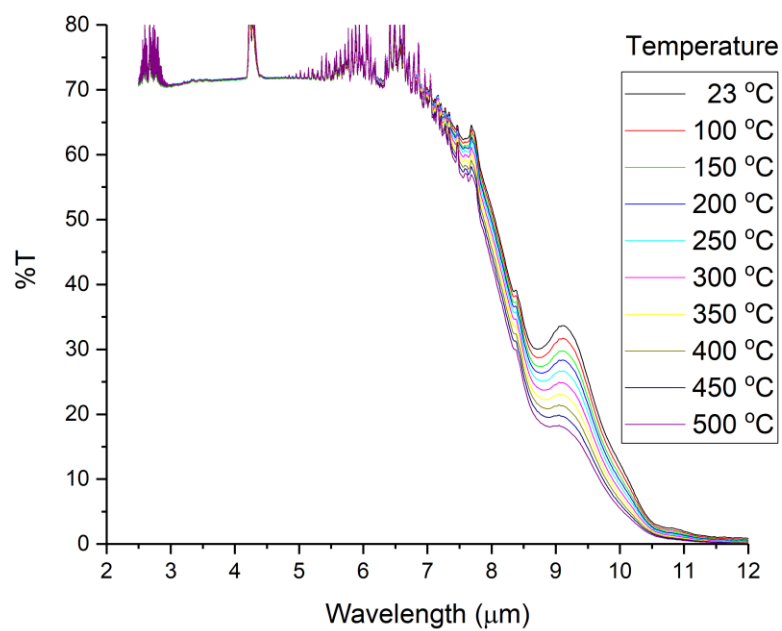
Figure 22: Transmission spectra of the sample with composition 20 mol% Ga_2Se_3 - 50 mol% Ga_2S_3 - 30 mol% La_2S_3 between 23 and 500 ^{o}C.
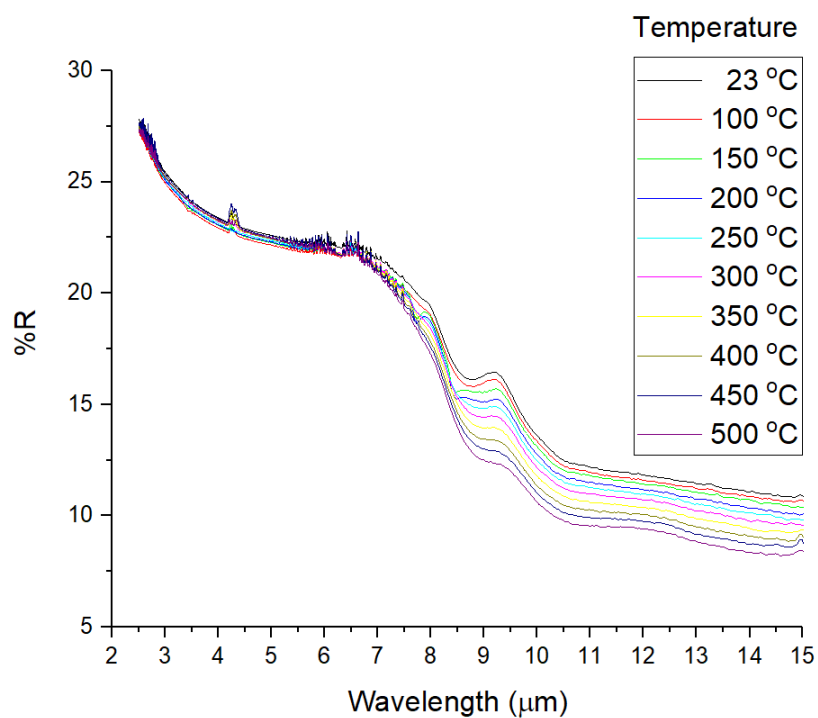
Figure 23: Reflectance spectrum of the sample with composition 20 mol% Ga_2Se_3 - 50 mol% Ga_2S_3 - 30 mol% La_2S_3 between 23 and 500 ^{o}C. Note: incident angle ~90°.

Table 3: Values of dn/dT at 8 and 10 μm for the sample with composition 20 mol% Ga_2Se_3 - 50 mol% Ga_2S_3 - 30 mol% La_2S_3

Glass	n Room Temperature	n 250°C	n 500°C	Wavelength (μm)	dn/dT (°C^{-1})	Reference
Se-GLS	2.3833	2.5511	2.7624	8	$0.7 \cdot 10^{-3}$	This work
Se-GLS	2.6083	3.0004	3.3147	10.6	$1.1 \cdot 10^{-3}$	This work
$Ge_{33}As_{12}Se_{55}$	2.4946	-	-	10.6	$0.067 \cdot 10^{-3}$	[21]
$Ge_{30}As_{13}Se_{32}Te_{25}$	2.7853	-	-	10.6	$0.103 \cdot 10^{-3}$	[20]
$Ge_{10}As_{40}Se_{50}$	2.6076	-	-	10.6	$0.020 \cdot 10^{-3}$	[22]
$Ge_{28}Sb_{12}Se_{60}$	2.6010	-	-	10.6	$0.060 \cdot 10^{-3}$	[17]
$As_{40}Se_{60}$	2.7764	-	-	10.6	$0.032 \cdot 10^{-3}$	[16]

3.3.3   Determination of the linear and non-linear refractive index

The refractive index dispersion of samples with composition 30 mol%La_2S_3 – 70 mol% Ga_2Ch_3 (Ch = S, Se) is shown in Figure 24. The determination of the refractive index was limited to this set of samples since it allowed an extensive assessment of the impact of selenium. In addition, in light of possible applications in multispectral imaging, this set of samples also demonstrated the largest glass formation region and thus deeper investigations were carried out. The fitting parameters resulting from the fitting of the raw data to Equation 21 are listed in Appendix E. As expected, the refractive index was found to increase with the amount of Se as a consequence of the higher polarisability of Se with respect of S.
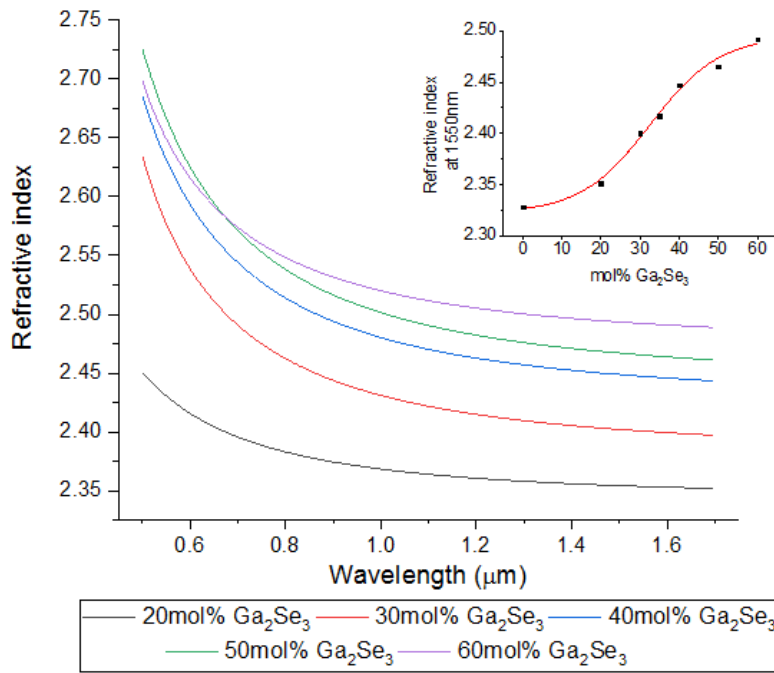
Figure 24: Refractive index dispersion for samples with composition 30mol% La_2S_3:70mol% Ga_2Ch_3 (Ch = S, Se).

The non-linear refractive index was measured for two samples containing 20 mol% and 35 mol% Ga_2Se_3 and one sample of regular GLS (65mol% Ga_2S_3 - 35mol% La_2S_3) for comparison. An example of the fittings carried out with Equation 22 is shown in Figure 25. As expected, the plots depicted the typical behaviour of $n_2 > 0$. The value of n_2 calculated for GLS was as high as $1.07 \cdot 10^{-18} m^2/W$ close to what reported for previous works.[115] In addition, growing values of n_2 were calculated for growing content of Se as a result of the increased polarisability of the system. Particularly, the fitting resulted in $n_2 = 1.20 \cdot 10^{-18} m^2/W$ for 20 mol% Ga_2Se_3 and $n_2 = 1.67 \cdot 10^{-18} m^2/W$ for 35mol% Ga_2Se_3. However, previous studies reported the influence of other factors on the change in n_2. In particular, studies on Ge-As-Se glasses pointed out two main contributions to the variation of refractive index. Firstly, it was found that the number of electron lone pairs of the elements contributed to increase n_2 (e.g. substitution Ge by As increasing the number of electron lone pairs from 0 to 1). Secondly, changes in the structure of the glass in terms of number of $GaSe_4$ tetrahedra affected the electron distribution, hence the inconsistent trend when As was added.[116] Both these observations are related to the change in the electron distribution in the glass and can be related to our case study. For starters, the substitution of S by Se did not change the number of electron lone pairs. However, the increased ionic radius changed the charge/radius ratio and thus the spatial distribution of the electrons. In addition, the larger radius of Se resulted in lengthened Ga-Se and La-Se bonds accentuating the effect on the charge distribution. The clarification of the impact of each contribution could an interesting starting point for future works.
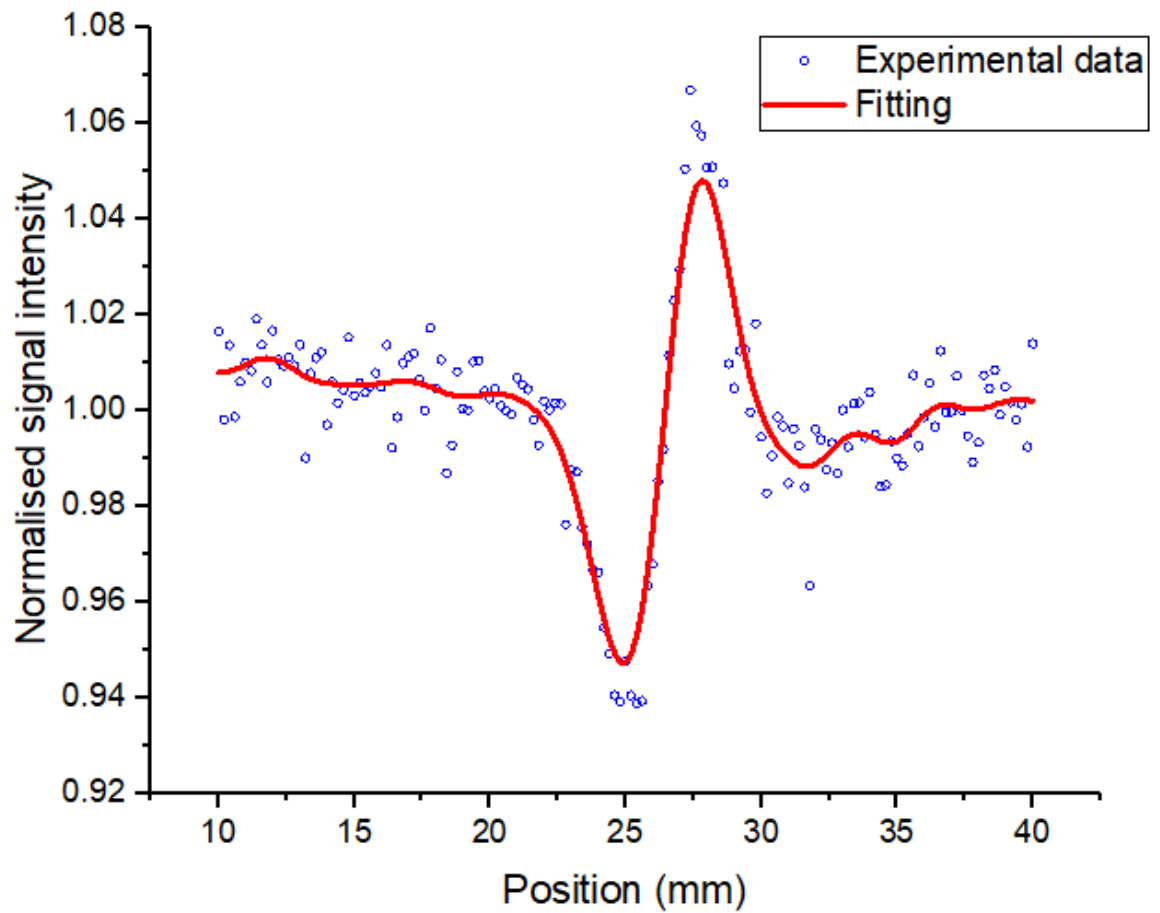
Figure 25: Z-scan plot for the sample containing 35 mol% Ga_2Se_3.

3.3.4 Terahertz time-domain spectroscopy

The absorption spectra and refractive index dispersion was investigated over a frequency range of 0.1 and 1 THz (Figure 26). As reported in Table 4, the THz refractive index of every sample is higher than the respective index at 1.50 μm. This is due to the ability of THz radiations to interact with both th electronic and ionic polarizability of a material. As a result, the material exhibits dielectric properties as the sum of the two contributions.[117] The mechanism the electronic polarizability consists of the distortion of the electron charge distribution within the lattice caused by an oscillating electric field. The timescale of this interaction is short (10^{14}-10^{15} Hz) making radiations belonging to the optical regime sensitive to the electronic polarizability. In particular, the polarizability experienced by optical radiations can be denoted as the average molecular polarizability. On the other hand, ionic polarizability is observed when an oscillating electric field interacts with the chemical bonds exciting higher lying vibrational states (e.g. optical phonons). The ionic relaxation time is significantly slower than the electronic. Therefore, radiations with lower frequencies (i.e. THz radiations) are responsible for the interaction with the ionic polarizability of materials.

Table 4: THz absorption coefficients and refractive indices

Sample number	Composition	Density (g/cm)	Optical refractive index @ 1.5 µm	Refractive index @ 0.8 THz	Absorption coefficient @ 0.8 THz (cm^{-1})
1	$La_{20}Ga_{20}S_{60}$	4.27	2.37 ± 0.04	3.93 ± 0.01	52 ± 2
2	$La_{16}Ga_{24}S_{60}$	4.48	2.38 ± 0.04	3.80 ± 0.01	46 ± 2
3	$La_{12}Ga_{28}S_{60}$	4.11	2.37 ± 0.04	3.63 ± 0.01	40 ± 2
4	$La_{12}Ga_{28}S_{48}Se_{12}$	3.99	2.35 ± 0.04	3.54 ± 0.01	51 ± 2
5	$La_{12}Ga_{28}S_{39}Se_{21}$	4.21	2.42 ± 0.04	3.66 ± 0.01	60 ± 3
6	$Ge_{28}Sb_{12}Se_{60}$ (IG5)	4.41	2.60 [17]	3.17 ± 0.01	31 ± 1
7	$Ge_{33}As_{12}Se_{55}$ (IG2)	4.66	2.73 [21]	2.85 ± 0.01	9 ± 0.5

The relationship between polarizability and refractive index is represented by the Lorentz-Lorenz equation in the form:[117]–[119]

$$\frac{n(v)^2 - 1}{n(v)^2 + 2} = \frac{4\pi}{2} Np(v)$$

Equation 25

where n(v) is the refractive index, p(v) is the polarizability and N is the molecular density of the material calculated as:

$$N = \frac{\rho}{MW} N_A$$

Equation 26

where ρ is the density, MW is the average molecular weight of the material and N_A is the Avogadro's number.
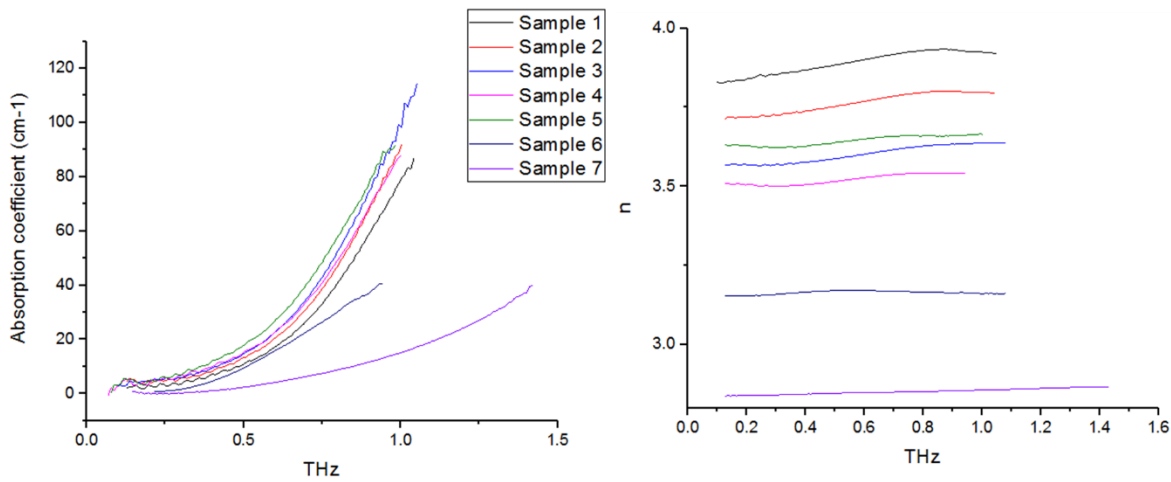
Figure 26: Absorption spectra and refractive indices of the samples listed in Table 4.

The polarizability of the investigated glasses was estimated from Equation 25 and it is reported in Table 4, along with the average molecular polarizability (i.e. electronic polarizability) calculated from data found in literature. As shown, the value of polarizability is calculated to bes larger than the mean atomic value for GLS-based samples, whilst for GeSe-based samples the difference was not as pronounced. This observation suggested that samples containing no La have low ionic polarizability. As a result, these samples exhibit an absorption coefficients and lower THz refractive indices than GLS-based glasses. The high ionic polarizability of GLS and GLSSe glasses could be caused by the large content of La. Indeed, La^{3+} in GLS glass was found to coordinate up to 7 S^{2-} anions in its outer shell.[120] In addition, the intrinsic polarizability of La^{3+} is large due to the size of the ion, which also results in a low electronegativity. These properties of La^{3+} increased the complex of the glassy network with many ionic bonds with high polarisability.

Figure 26 depicts the attempt to establish a relationship of direct proportionality between absorption coefficient and refractive index. Two linear trends were found with different slopes. The first group includes Se-based glasses, whilst the other consists of pure GLS glasses containing only S. The substitution of S by Se resulted in an increase of the polarizability of the glasses, due to the larger ionic radius and the weaker bonds established. Moreover, the presence of both Se and S contributed to an increase of the charge disorder and thus increased absorption coefficient. Therefore, the samples containing Se fall on a steeper absorption slope than those containing only S. The same trend can be attributed the presence of La^{3+} increasing the complexity and the charge disorder of the lattice.
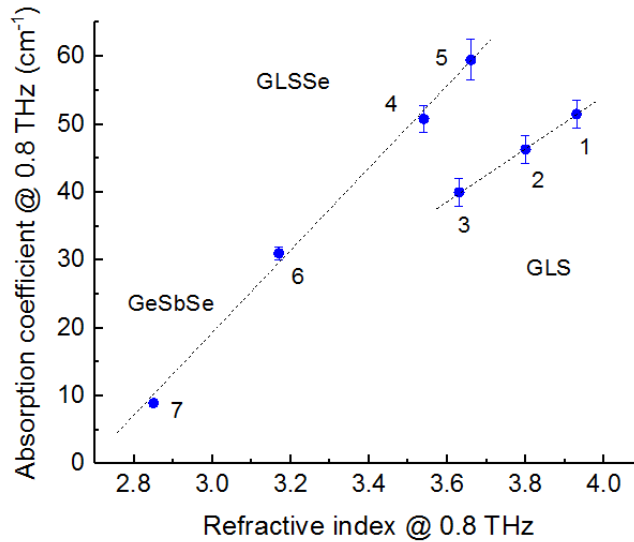
Figure 27: Correlation between the absorption coefficient and refractive index at 0.8 THz

The frequency dependence of absorption coefficient and refractive index in THz regime can be correlated to the charge disorder induced by the radiation as:[121]

$$n(v)\alpha(v) = Kv^{\beta} \qquad\qquad \text{Equation 27}$$

where n(v) is the refractive index, α(v) is the absorption coefficient, and K and b are material-dependent parameters. In particular, multicomponent glasses were found to have larger values of K, which is the coefficient related to pronounced charge fluctuations, and therefore could represent the disorder in the glass structure.[12], [118] In previous works, the exponent β was consistently found to be around 2 for amorphous materials and an alternative model to Equation 27was formulated assuming a square relationship.[121], [122] However, the squared law resulted in poor fittings (Figure 28) and Equation 27 was preferentially used. The fittings showed that higher values of K correspond to materials with higher polarizability.
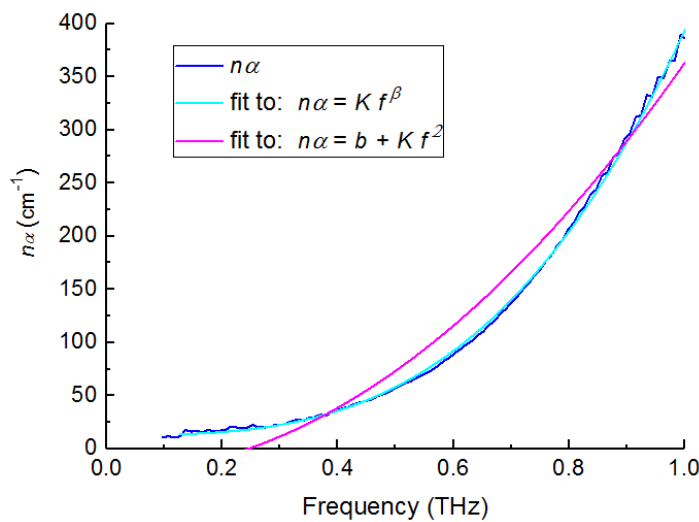
Figure 28: Results of fittings to squared law (violet) and Equation 27.

Figure 29 shows the trends found to correlate the refractive index and the fitting parameters. As expected, the correlation between K and n(v) is similar in trend to that between β and n(v). These linear trends could be a consequence of the La content in the glass which affected the charge spatial disorder. The large coordination number of La^{3+} resulted in a large number of possible spatial arrangements in the glassy lattice, hence the increase of K to 2 (as predicted) to 3. In the case of GLSSe glasses, the formation of Se-O and O-Se-O due to the presence of oxygen impurities could have an impact in the measurements. Indeed, Se ions can cover a range of oxidation states from 2- to 2+, thus also contributing to increase the charge disorder and higher values of K in Se-GLS glasses than regular GLS. The relationship between β and n and the unexpectedly large value of β are still not fully clear and require further investigation as this behaviour has never been observed before. One hypothesis was formulated relating β and the degree of disorder of the glass network, since β depicts the amorphous arrangement of the atoms.

Table 5 compares the value of β for other glasses. It must be noted that for some of those β was fixed as 2.[121], [123] Most of those materials (e.g. silica, quartz, GeGaAsSe, pyrex) contain cations with a coordination number as high as 4, which appear to relate to β=2. However, a value of β=2.3 for the BK7 glass containing 9 mol% Na and β=2.8 for SK10 glass containing 48 mol% BaO and 12 mol% B_2O_3. It could be possible that β>2 could be plausibly assigned to glasses with cations high in coordination number. For instance, Na^+ can have a coordination number of 8 in chalcogenide glasses and lanthanum up to 7.[120] Hence the value of β=3 for GLS and GLSSe glasses.
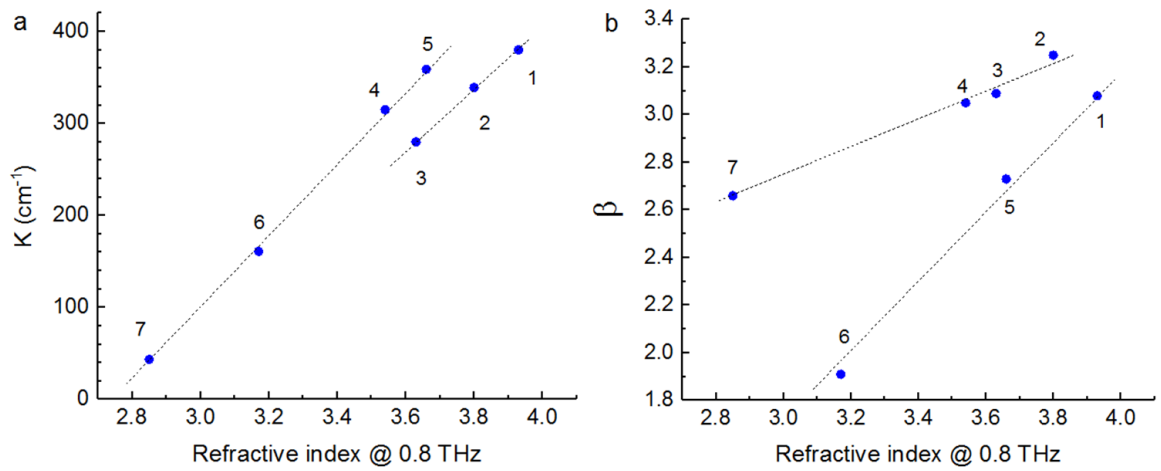
Figure 29: a) Relationship between K and refractive index at 0.8 THz; b) Relationship between β and refractive index at 0.8 THz. Numbers denote sample numbers.

Table 5: Value of β reported for glasses

Composition	β	Reference
$La_{12}Ga_{28}S_{60}$	3.09	This work
$La_{16}Ga_{24}S_{60}$	3.25	This work
$La_{20}Ga_{20}S_{60}$	3.08	This work
$La_{12}Ga_{28}S_{48}Se_{12}$	3.05	This work
$La_{12}Ga_{28}S_{39}Se_{21}$	2.73	This work
$Ge_{28}Sb_{12}Se_{60}$ (IG5)	1.91	This work
$Ge_{33}As_{12}Se_{55}$ (IG2)	2.66	This work
$As_{40}S_{60}$	1.95	[119], [124]
$As_{40}Se_{60}$	2.0	[119]
$Ge_{30}As_8Ga_2Se_{60}$	2.0	[125]
$Ge_{35}Ga_5Se_{60}$	2.0	[125]
$Ge_{10}As_{20}S_{70}$	2.0	[125]
$Tl_2SeAs_2Te_3$	1.9	[119]
Amorphous silica SiO_2	2.0	[119], [126]
Pyrex	2.0	[119]
BK7	2.28	[123]
	2.80	[123]

3.4   Conclusions

In this chapter, the effect of Se, Te and In to the optical properties of GLS have been studied explaining the observed changes by considering physical-chemical parameters such as bond strength, electronegativity and polarisability. In particular, the elements used to substitute S and Ga possessed a higher molecular weight, a larger ionic radius, a lower electronegativity and a higher ionic polarisability than the elements they replaced. As a result, the chemical bonds within the modified glasses were expected to be weaker and longer than those in unmodified GLS. The implications of these changes were probed measuring the transmission window, the linear and non-linear refractive index in the visible-to-infrared range, whilst in the THz range the absorption coefficient and the refractive index were measured.

The weaker and longer bonds caused a shift of the IR cut-off towards longer wavelengths following the prediction made with the harmonic oscillator model widely used in IR spectroscopy.[103] The shift in Se-modified GLS became more prominent as the amount of S substituted by Se increased, pushing the cut-off edge from 13.36 to 16.62 μm. This extension of the transmission window was accompanied by a modest shift of the electronic cut-off edge from 494 to 575nm as a result of a narrower bandgap. In the THz region the width of the transmission window did not undergo significant changes except for a decrease in absorption coefficients for 20 mol% Ga_2Se_3. However, more evident changes were observed in the refractive index. In particular, the increase in ionic and electronic polarisability provoked an increase in refractive over the whole spectral range from visible to THz. In addition, the content of La had a significant impact to the THz refractive index since the optical properties in this spectral region are strictly dependent on the ionic polarisability. The measurement of n_2 resulted in an analogous growing trend following the amount of Se in the glass.

The retention of transmission in the visible range was an unexpected observation since similar compositional studies reported a more dramatic change in the Visible range. To date, only few materials with a transmission window ranging from visible to LWIR have been reported. The only one commercially available is As_2S_3, which is produced with high purity but has many disadvantages with respect of Se-GLS, in particular the lower melting point and toxicity (Section 3.3.1). Other materials are produced only at a laboratory level and are mainly chalcogenide glass ceramics containing CsCl.[27], [43], [75], [127] The main disadvantage of CsCl-based glasses is their affinity to moisture, which increases dramatically the OH absorption. Therefore, the optical properties of Se-GLS glasses make this class of materials a promising candidate for multispectral imaging applications. However, further efforts should be spent on increasing the purity of the glass in order to eliminate the Ga-O and Se-O absorption peaks. The larger transmission window and increased the non-linear effects in Se-GLS could be an interesting starting point for studies on supercontinuum generation. Proof of principle of supercontinuum generation are currentlwith GLS glasses reported an emitted spectrum with a bandwidth of 3250 nm.[128] The increased nonlinearities in Se-GLS could be beneficial to supercontinuum generation and larger spectra could be plausibly expected.

Chapter 3

Chapter 4

Thermal and thermo-mechanical characterisation

Thermal analysis usually refers to a set of experimental techniques that allow to characterise the chemical and mechanical behaviour of a glass as a function of the temperature. The thermal characterisation is of fundamental importance to develop a deep understanding of the structure and properties of the glass and the effect of these factors on the performance of the glass in specific application areas. In this chapter, the determination of the thermal and thermo-mechanical properties of modified GLS glasses and the techniques used for the characterisations are described. The results were interpreted in order to assess the effect of each modifier added to GLS and to draw clearer conclusions on the structure of the glasses. In addition, the results were compared to the data reported for commercially available glasses in order to evaluate the capabilities of the glasses and their potential applications.

The properties studied for the glasses under investigations included the Vickers hardness (H_v), the viscosity curves, the coefficient of thermal expansion (CTE), the specific heat capacity (c_p) and the characteristic temperatures, namely glass transition temperature (T_g), crystallisation temperature (T_x) and melting temperature (T_m). As a result of the addition of Se, Te and In to GLS glass, the properties of the modified samples were expected to reflect the change of chemical bonds.[57] In particular, the additives were expected to form weaker chemical bonds with a subsequent decrease of the characteristic temperatures, H_v and c_p of the glass. On the other hand, based on the increase in CTE substituting La_2S_3 for La_2O_3, the coefficient of thermal expansion (CTE) was expected to undergo a minor growth upon addition of Se.[129], [130] The thermal stability of the glass was also determined as outlined in previous works.[131] Generally, a large difference between T_g and T_x is desirable for processes in which the glass is shaped into optical components such as lenses or optical fibres. Furthermore, since the range of viscosities required for fibre drawing is between 10^4 and 10^5 Pa·s, it is particularly important to correlate any change in the phase of the material and the viscosity profile. Other processes such as precision moulding and extrusion can be carried out at temperatures much closer to T_g within a wider range of viscosities.[85] In light of the novelty of these materials and their optical properties, the results of the thermal characterisation were compared to the data available for commercial chalcogenide glasses aiming to compare the properties of well-developed materials and the materials produced in this work. The results showed superior mechanical and thermal properties for GLS-based glasses which make these material good candidates for a variety of applications from thermal imaging optics to optical fibre sensing and communication.

4.1   Thermal behaviour of glass

The study of the behaviour of glasses in response to changes in temperature produces similar observations across all the glass forming materials, leading to the establishment of significant temperatures called characteristic temperatures (Section 4.2).[85] Among these, the characteristic temperature most distinctive trait of glass forming materials is the glass transition temperature T_g, defined as a reversible change occurring to amorphous materials transitioning from a hard and brittle state to a more viscous and rubbery state.[132] The temperature at which glass transition occurs observed is strictly dependent on the cooling rate reached during the manufacturing process and the thermal history of the glass. However, the observed T_g also depends on the heating rate used in the experiment of thermal characterisation. This parameter tends to shift the value of T_g towards higher temperatures as the heating rate applied is increased. It is well known that as-quenched glasses retain a significant amount of internal stress and need to be annealed in order to improve the mechanical properties and the stability of the glass. The annealing process also results in a change in T_g which can be observed at lower temperatures after this heat treatment. However, the release of structural stress can occur only above the so-called strain point (T_s) where the viscosity of the glass is above 10^{13} Pa·s. Glass annealing is usually carried out between T_g and the strain point in order to avoid the devitrification of the samples.

The melting point is another important parameter generally determined with the thermal analysis. In this work the melting point was observed after the glasses crystallised due to the features of DTA machine. Therefore, the melting point was assigned as the temperature at which the crystals started to melt corresponding to the onset of the melting peak. The endset of the peak represents the liquidus point above which crystals cannot be stably formed. [59]

The thermal devitrification of glass is usually manifested as a phase transition from amorphous to crystalline structure. Crystallisation of glass melts and solid glasses is a transformation having Gibb's free energy (ΔG) as driving force but disfavoured by the kinetics of the process. In particular, crystallisation is a two-step process requiring crystallisation centres to be formed with nucleation first, followed by crystal growth.
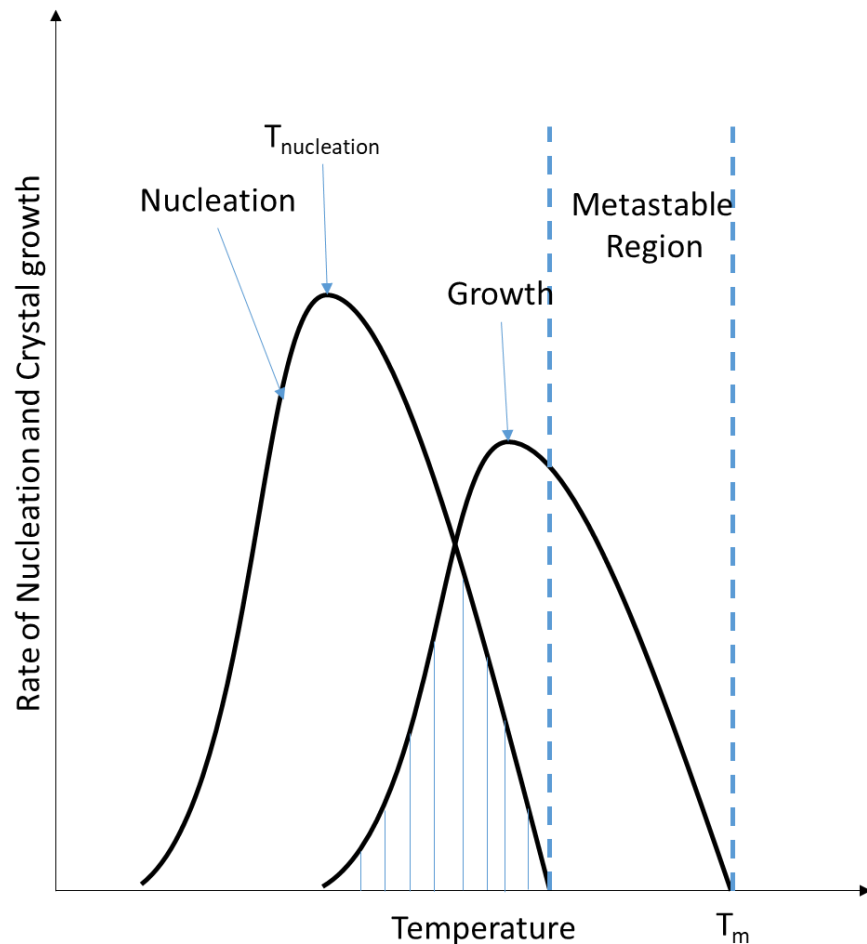
Figure 30: Variation of the rates of nucleation and crystallisation according to the temperature.[133]

The nucleation step tends to occur at higher rates and lower temperatures than crystal growth (Figure 30). Ideally, a sufficiently fast quenching rate is reached within the metastable temperature range (Figure 30), the melt quench can prevent both nucleation and crystal growth. In this way, the amorphous structure will be retained. If the high quenching is not optimal, two main outcomes can be expected. Firstly, the quenching rate allowed to avoid crystal growth but not nucleation and the glass will form with a large amount of small crystals. It must be noted that devitrification can occur from the nuclei in thermal treatments in which the temperature exceeds T_g (e.g. annealing). Secondly, the quenching rate is substantially slower than the ideal case with the nucleation and crystallisation steps can occur within in the temperature region were these two overlap (dashed region, Figure 30). This leads to the formation of large crystals or full crystallisation. For both glass melts and re-heated glass, two types of crystallisation can be defined according to the nature of the crystallisation centre. Firstly, the heterogeneous nucleation occurs when the crystallisation centre is a foreign particle or is formed by impurities modifying the local thermal profile of the glass melt. The crystals formed through this mechanism are generally distributed along the surface between the melt and foreign bodies and is more frequent

75

than homogeneous nucleation. Since this process requires the presence of extrinsic defects, the small ΔG difference cannot prevent the crystal from growing even within the metastable temperature range. Heterogeneously-grown crystals are generally large, isolated particles with an uneven distribution. [59] Secondly, the homogeneous crystallisation occurs when the crystallisation centres are formed via nucleation of the glass melt. In particular, during glass melting regions with spatial long-range order continuously form and dissolve during glass melting as a result of the competition between the decrease in ΔG of the system and the high surface energy of the nuclei. When the temperature is decreased the nuclei become increasingly stable as their diameter increases over a critical value. This growth mechanism is diffusion limited and terminates once the viscosity of the glass melt does not allow the movement of atoms and particles. This crystallisation mechanism is less common and is usually observed in glasses melted without any homogenisation apparatus (e.g. stirring apparatus or rocking furnace). However, this mechanism is usually exploited for the production of glass ceramics with improved mechanical features.[134]

4.2   Thermal and thermo-mechanical properties of glass

The characterization of thermal and mechanical properties of glass are essential for an effective design and manufacturing processes of optical components. The accurate determination of temperature-dependent parameters enables a detailed analysis to understand the behaviour of a glass forming system upon changes in composition. One of the most important features to investigate is the thermal stability of the glass. This is usually estimated with a figure of merit correlating T_g, T_x and T_m.[135] The most common parameters found in literature include the Hruby parameter (K_H), the Weinberg parameter (K_W) and the Lu-Liu parameter (K_{LL}), calculated as:[136]–[138]

$$K_H = \frac{(T_x - T_g)}{(T_m - T_x)}$$

Equation 28

$$K_W = \frac{(T_x - T_g)}{T_m}$$

Equation 29

$$K_{LL} = \frac{T_x}{(T_m + T_g)}$$

Equation 30

Since all these parameters aim to allow the comparison of the thermal stability of glasses regardless the compositions, it is important to understand the sensitivity of each parameter to small changes in composition of a known glass. Indeed, if the variation of the parameter with the

composition is small, this may not be the best to represent changes in compositions and important details on the thermal stability could be missed. This aspect has been investigated in a comparative study on K_H, K_W and K_{LL} carried out on the system Ag_2Te-As_2Se_3-$CdTe$.[131], [139] As a result, K_{LL} was revealed to have the smallest change even for large variations in compositions. The comparison of K_H and K_W resulted in the two parameters exhibiting similar behaviours with high rates of change after compositional variations. In order to determine the parameter best representing the changes resulting from Se, Te and In addition to GLS glass, both parameters have been investigated and compared.

Along with the thermal stability, the determination of the temperature-dependent viscosity curve for glass is generally required to develop the thermal profile of the fabrication process of optical components (e.g. fibre drawing). In particular, the determination of the working range of viscosities is the starting point to tailor the temperature according to the component wanted. The viscosity of glass at temperatures about T_g follows the same behaviour of Newtonian liquids, described as:[140]

$$\sigma_{yx} = \eta + \frac{dv_x}{dy}$$

Equation 31

where σ_{yx} is the shear stress, η is the dynamic viscosity of the moving liquid and $\frac{dv_x}{dy}$ is the velocity gradient across the liquid front. The relationship between viscosity and temperature can be described by the Boltzman relation as:[141]

$$\eta = K \cdot e^{\left(\frac{E_\eta}{RT}\right)}$$

Equation 32

where K is a constant in units of viscosity (Pa·s or dPa·s), E_η is the activation energy for molecules to become mobile, R is the Universal gas constant and T is the temperature. In order to describe the behaviour of glass melts, Equation 32 has to account of the gradual disruption of the glass network with temperature and with a temperature-dependent activation energy changing according to the local composition of the glass. A good approximation of this mechanism is provided by the Vogel–Fulcher–Tammann (VFT) equation, defined as:

$$\eta = K_{VFT} \cdot e^{\left(\frac{E_0/R}{T-T_0}\right)}$$

Equation 33

where K_{VFT}, E_0 and T_0 are fitting parameters.[142]

As mentioned above, the determination of the viscosity curves of glasses highlighted similarities between all the amorphous materials. In particular, it was noticed that for specific values of

viscosity, all glasses have analogous properties regardless the composition. The temperatures corresponding to each value were defined as characteristic temperatures. These characteristic temperatures are usually taken as guidelines while developing thermal treatments for glass to avoid unwanted effects. Some examples are given by the strain point (temperature below which structural stress cannot be released, $\eta = 10^{13}$ Pa·s), the glass transition ($\eta = 10^{12}$ Pa·s), the softening point (temperature at which a specimen of glass sags under its own weight, $\eta = 10^{6.7}$ Pa·s) and the working temperature (temperature at which glass can be modelled in a desired shape, usually $\eta = 10^{3}$ Pa·s).[59], [85]

An alternative route to determine the T_g is to observe the thermal expansion of a glass specimen. Indeed, when the T_g is reached the glass exhibits an abrupt change in the coefficient of thermal expansion (CTE). [59] The coefficient of linear thermal expansion is defined as:[143]

$$\alpha(T) = \frac{1}{l_0} \cdot \frac{l(T) - l_0}{T - T_0} \qquad \text{Equation 34}$$

where l_0 is the initial length of the specimen, $l(T)$ is the length of the specimen at the temperature T, T_0 is the initial temperature of the experiment. The determination of this parameter is frequently done along with the determination of the specific heat capacity (c_p). The c_p represents the amount of energy to supply to a material in order to have a change in temperature.[144] Chalcogenide glasses tend to have a low c_p corresponding to a small amount of energy required to observe a change in temperature. Therefore, these materials should also undergo a fast heat exchange during thermal processes. The combination of CTE and c_p gives good information about the probability of the material to suffer from thermal damages due to inhomogeneous expansion and contraction due to a slow heat exchange. The formation and propagation of cracks is often observed during the fabrication of large items such as bottles and windows as a result of the inhomogeneous cooling and the composition of the glass has to be tailored to minimise the occurrence of these defects. The occurrence of thermal damages during the fabrication of small optical components is less frequent. However, these parameters are needed to tailor applications and devices working at high temperature.

4.3   Techniques of characterisation

4.3.1   Instruments for thermal analysis

The techniques to carry out the thermal characterisation of novel materials are predominantly Differential Scanning Calorimetry (DSC), Differential Thermal Analysis (DTA) and Thermo-Mechanical Analysis (TMA). [59] The results from these three techniques are often combined in

order to depict a comprehensive picture of the properties of a new material and fully understand its capabilities. DSC is generally used to carry out calorimetric investigations from which parameters such as the c_p can be calculated. In addition, the characteristic temperatures and the enthalpy of the relative thermodynamic events can be determined. The fundamental equation of DSC is:

$$\text{Signal}\left(\frac{W}{g}\right) = c_p\left(\frac{J}{K \cdot g}\right) \times R\left(\frac{K}{s}\right)$$

Equation 35

where R is the ramping rate. The DSC used for the characterisation of the glass samples was functioning in flux mode. A schematic of the machine is depicted in Figure 31. In this configuration, the reference and samples are positioned in the same furnace with two (or more) sensors measuring the respective temperature.
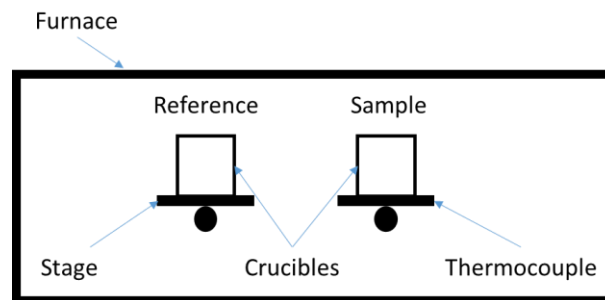
Figure 31: Configuration of DSC.

The shape of the DSC curve (thermogram) depends on the specific heat capacity of the sample as shown in Equation 35. When a given thermodynamic event takes place, the difference in temperature between the two sensors increases in absolute value. The sign of the difference is positive or negative according to the transformation taking place (Table 6). The difference in temperature is then converted in heat flow by mean of a calibration preceding the sample scan. The design of the DSC analyser shown in Figure 31 was the same as the one of the DTA adopted to determine the characteristic temperatures of the samples. The main difference between DSC and DTA stands in the design of the machine. In particular, DTA is usually not calibrated for calorimetric measurements and it is suitable for sensing changes in temperature which cannot be accurately converted in heat flow. Therefore, the thermograms recorded by DTA are usually in units of µV. The DTA system used during this work was combined to a Thermo-Gravimetical Analyser (TGA) to sense the losses of mass and relate them to the thermogram. The loss of mass by the sample is usually sign of desorption processes (e.g. moisture desorption from the surface) or decomposition processes. This tool simplifies the distinction between peaks relative to phase changes (e.g. melting, glass transition, crystallisation, etc) and degradative processes and can be used to optimise the manufacturing operations.

Table 6: Classification of the main thermodynamic phenomena observed with thermal analysis.

Endothermic	Exothermic
Melting	Crystallisation
Desorption	Adsorption
Vaporisation	Condensation
Sublimation	Deposition
Reduction	Oxidation
Glass transition	Chemisorption

A schematics of the set up used for TMA is shown in Figure 32, depicting the analyser used for the determination of the CTE and the viscosity (η) curve. This technique is generally employed to observe linear or volumetric changes occurring to the specimen in relation to time, temperature and applied force. In order to examine the changes the specimen is undergoing, the machine needs to be set up with different probes. In particular, a flat-tip probe was used to measure the linear expansion whilst a knife-edge probe was used for the viscosity curve. The following section describes the models adopted to extrapolate the thermal parameters for some of the glasses manufactures.
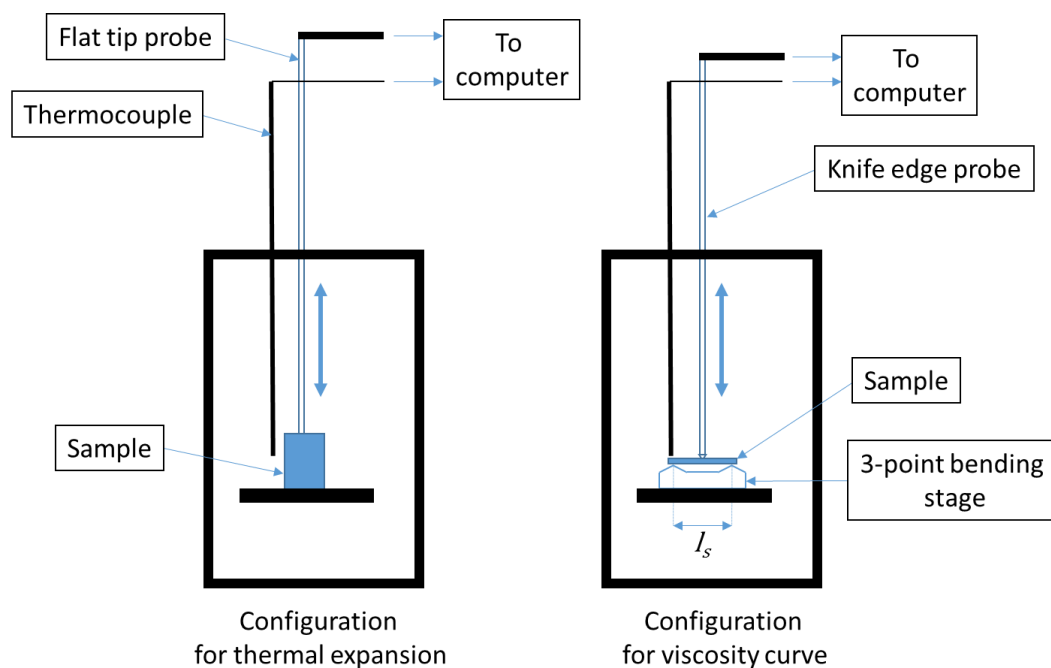
Figure 32: Schematics of the configuration adopted for TMA for thermal expansion (left) and viscosity curve (right).

4.3.2   Models for data analysis

The determination of the characteristic temperatures T_g, T_x and T_m were carried out with a TG-DTA covering a range of temperatures between room temperature and 950°C. The peaks observed as the temperature (Figure 33, left to right) was increased were T_g, T_x and T_m, respectively. The peaks pointing downwards corresponded to endothermic transformations whilst peaks pointing upwards represented exothermic transformations. In both cases, the relative characteristic temperature was determined as the offset of the peaks since it represents the temperature at which the transformation began. The offset was taken as the intersection point between the tangent to the baseline and the initial slope of the peak. From the values obtained, the Hruby parameter and the Weinberg parameter for thermal stability were calculated with Equation 28 and Equation 29, respectively.
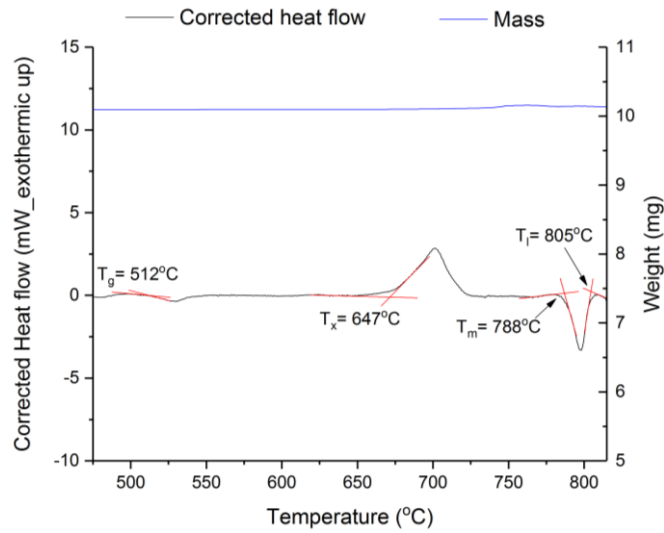
Figure 33: TG-DTA thermogram for sample with composition 30mol% La_2S_3 – 50mol% Ga_2S_3 – 20mol% Ga_2Se_3

The c_p was measured following the procedure adopted for plastic materials as outlined by the standard ISO 11357-4 2014.[144] The standard method required the use of DSC to acquire calorimetric curves for a blank run (i.e. both reference and sample slots empty), a calibration run (e.g. aluminium) and a specimen run. Applying the continuous scan method, the c_p of the sample under investigation can be calculated as:

$$c_p^{sample} = c_p^{Al} \cdot \frac{m^{Al}(P_{sample} - P_{blank})}{m^{sample}(P_{Al} - P_{blank})}$$

<div align="right">Equation 36</div>

where c_p^{cal} is the specific heat capacity of the calibration specimen of aluminium in J/(K·g), m^{Al} and m^{sample} are the respective masses of the Al specimen and the sample, P_{sample}, P_{Al} and P_{blank} are

the temperature-dependent heat flows measured of each run.[145] The results were expressed as the average of three measurements with the standard deviation as absolute error.

The determination of the CTE was carried out in accordance to the standard ISO 11359-2 1999 with the TMA configure as depicted in Figure 32.[143] The temperature-dependent elongation of a cuboidal specimen was measured as the displacement of the flat-tip probe along its mechanical axis. In order to keep the tip of the probe and the top of the specimen in touch, a force of 100mN was applied. The CTE was then calculated with Equation 34. The temperature boundaries were taken according to the noise of the dataset, which was often found to be high at temperatures close to room temperature.

The measurement of the viscosity curves was carried out with a 3-point-bending configuration in which the TMA was equipped with a knife-edge probe and the sample was loaded on a bending stage (Figure 32). The procedure followed was the standard ISO 7884-4:1987.[146] A load of 500mN was applied on the specimen in order to neglect the effect of gravity within the calculation. As reported in the ISO standard, the viscosity was calculated as:

$$\eta = 681 \cdot \frac{l_s^3 m \Delta t}{I_c \Delta f}$$

Equation 37

where η is the viscosity, l_s is the span of the bending stage in millimetres, Δt is the measured time in seconds, m is the applied load in grams, Δf is the sag of the sample in millimetres during the time Δt and I_c is the cross-sectional momentum of inertia for a cuboidal sample measured as:

$$I_c = \frac{h^3 b}{12}$$

Equation 38

where h and b are the height and the width of the specimen in millimetres, respectively. The data points obtained with Equation 37 were then fitted to the Vogel–Fulcher–Tammann equation in the form:[142]

$$\log_{10} \eta = k + \frac{A}{T-B}$$

Equation 39

where T is the temperature whilst k, A and B are fitting parameters obtained with a least-squares fitting method. The value of k was reported to represent the logarithm of the viscosity of a theoretical free particle of the material and it was fixed as -5 as reported in previous works.[147]

The mechanical hardness of the materials was measured at room temperature determining the value of Vickers hardness (H_v). The H_v was measured by mean of a Matsuzawa microindenter functioning as shown in Figure 34. The indentation was made by a diamond tip in the shape of a

squared-base pyramid. After the indentation, a microscope was used to measure the two diagonals of the printed square. The value of H_v was then calculated with the formula:[148]

$$H_V = 1.8544 \cdot \frac{F}{d^2}$$

Equation 40

where F is the load applied and d is the average measure of the diagonals of the printed square. The value obtained represented a figure of merit to compare the mechanical strength at room temperature of the samples.
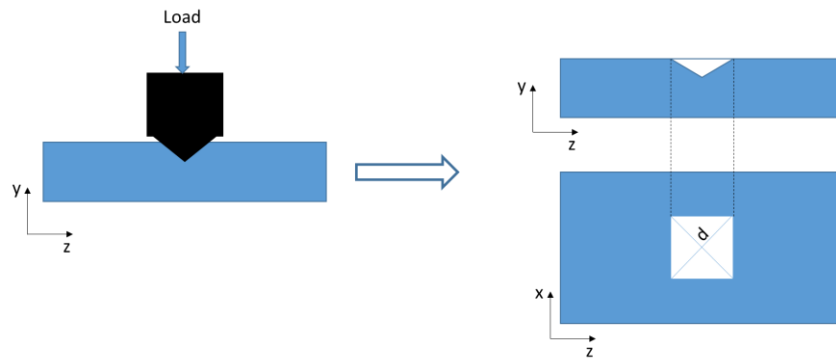
Figure 34: Schematics of Vickers test for the determination of the Vickers hardness.

4.4   Results

4.4.1   Characteristic temperatures and thermal stability

The TG-DTA analysis carried out on all the samples exhibiting an amorphous structure revealed that the addition of Se to GLS glass did not decrease the characteristic temperatures dramatically (Table 7). In general, all the samples exhibited lower characteristic temperatures than the regular GLS glasses as a consequence of the lower melting temperature of Ga_2Se_3 replacing the higher melting Ga_2S_3.[57] In addition, for the compositions along the tie-line corresponding to 30mol% La_2S_3 the thermal stability parameters decrease in value as the weaker Ga-Se bonds replaced Ga-S bonds. However, the melting temperature of all Se-added sample exhibited a melting point above 750°C with a minimum of 766°C for 70 mol% Ga_2Se_3. Furthermore, almost all the compositions are characterized by improved thermal stability indicators compared to GLS glass.[67] The range of compositions between Sample 3 to Sample 6 showed T_g to reach a plateau where no significant changes were observed, while for complete substitution of Ga_2S_3 by Ga_2Se_3 caused pronounced changes. This proved that Ga_2Se_3 had the strongest effect on the chemistry of GLS glass at low and high concentration. The largest drop in T_g was observed for Sample 9 for which the glass transition was observed at 87 °C lower than the regular GLS glass previously reported as high as 553 °C.

Along the 20mol% and 30mol% Ga_2Se_3 tie-lines where only the Ga/La ratio was varied, the glass transition temperature was found to undergo significant variations. The largest change was observed between Sample 1 (50 mol% Ga_2S_3) and Sample 10 (40 mol% Ga_2S_3), for which the T_g decreased from 512 to 540°C as the amount of Ga_2S_3 was increased. This observation could be explained by the formation of stronger covalent bonds belonging to La_2S_3 increasing the T_g.

The thermal analysis of Sample 13 was characterised by two glass transition temperatures. This observation was reported in previous studies on glasses undergoing phase separation within the melt or spinodal decomposition.[59], [149] The characteristic temperatures could indicate the presence of the two phases. In particular, a phase with low T_g and T_x (330 and 556 °C, respectively) could be formed with a low concentration of La and high concentration of Se resulting in weak bonds. The second phase showed higher T_g and T_x (512 and 747 °C, respectively) was found to undergo glass transition at a temperature similar to Sample 2, indicating a possible concentration of Se of 20mol%. As shown in Table 7, a number of samples possessed multiple crystallization peaks in agreement with previous works on crystallized GLS glasses where two possible crystal phases were recognised.[120]

Table 7: Summary of results of thermal analysis.

Sample number	Ga_2S_3 [mol%]	La_2S_3 [mol%]	Ga_2Se_3 [mol%]	T_g [°C]	T_x [°C]	T_m [°C]	K_W	K_H
1	60	30	10	526	646	797	0.151	1.258
2	50	30	20	512	674	788	0.206	0.704
3	40	30	30	516	661	785	0.185	0.855
4	35	30	35	505	654	775	0.192	0.812
5	30	30	40	500	655	773	0.201	0.761
6	25	30	45	496	649	773	0.198	0.810
7	20	30	50	494	634	769	0.182	0.964
8	15	30	55	496	633	768	0.178	0.985
9	10	30	60	497	627	767	0.169	1.077
10[1,3]	0	30	70	466	602	766	0.178	1.206
11[1]	40	40	20	540	658	790	0.149	1.119
12	45	35	20	538	664	789	0.160	0.992
13[2]	50	20	30	320 / 513	556 / 747	780	-	-
14[1]	30	40	30	534	648	779	0.146	1.149

1(Contained particles); 2(Phase separation); 3(Produced with RF furnace)

The results of the thermal characterization of Ga_2Te_3-added samples are reported in Table 8. Samples 15 and 16 exhibited glass transition at higher temperatures than Se-added GLS glass. The glass ceramic nature of sample 16 could also contribute to a higher T_g than sample 15. On the other hand, the crystallization was observed at temperatures comparable to samples containing large amounts of Se. An analogous observation was made in commercial AsSe glass when Te was added. As a result, the T_g was increased by 30 °C from 103 °C to 133 °C.[150] This behaviour could be due to an increase of the activation energy required for glass transition to occur as described in some studies on Te-added AsSe glasses.[151] Analogously, the observation of higher melting temperatures of Sample 15 and 16 compared to Se-added glasses may have followed the same principle. The introduction of In in Se-added GLS glass (Samples 17-19) produced a considerable reduction of all the characteristic temperatures as the concentration of In was increased. For the three samples, the T_g was registered below 500 °C and the melting temperature above 700 °C for Samples 17 and 18. These effects could be due to the formation of weak In-Se bonds within the

Chapter 4

glassy network which may have affected also the optical, mechanical and thermo-mechanical properties.[117]

Table 8: Comparison between Se, Te and In GLS glasses.

Composition	Modifier	Tg (°C)	Tx (°C)	Tm (°C)	K_W	K_H
70:30 GLS*	-	553	660	816	0.154	0.686
Sample 2	20 mol% Ga_2Se_3	512	674	788	0.206	0.704
Sample 3	30 mol% Ga_2Se_3	516	661	785	0.185	0.855
Sample 5	40 mol% Ga_2Se_3	500	655	773	0.201	0.761
Sample 9	60 mol% Ga_2Se_3	497	627	767	0.169	1.077
Sample 10**	70 mol% Ga_2Se_3	466	602	766	0.178	1.206
Sample 15	10 mol% Ga_2Te_3	529	635	811	0.131	0.602
Sample 16**	20 mol% Ga_2Te_3	535	638	816	0.126	0.579
Sample 17	10 mol% In_2S_3	499	638	775	0.179	1.015
Sample 18	20 mol% In_2S_3	453	601	706	0.210	1.410
Sample 19**	30 mol% In_2S_3	420	607	646	0.289	4.795

*(Reference [67]); **(Contained particles).

From the results of the thermal characterisation in Table 7 and Table 8 it could be observed that K_W and K_H follow trends with some similarities. Firstly, both figures of merit confirm the thermal stability of the modified glasses to be improved. This observation is mainly due to the decrease in T_m and in the subsequent narrowing of the T_m-T_x gap resulting in higher figures of merit. Secondly, for the Se-GLS glasses series both parameters oscillate between local maxima and minima. However, K_W exhibited a constant decrease after reaching a local maximum at 40mol% Ga_2Se_3 (Table 7) whilst K_H constantly increased along with the concentration of Se. Thirdly, K_W and K_H exhibited the same trend for Te and In. However, K_H increases dramatically with the content of In because the T_m-T_x gap was narrowed (Equation 28). In particular, K_H for sample 20 assumes this glass to be more than 3 times thermally stronger than Sample 19. On the other hand, K_W had a more modest increase since only T_m appears at the denominator (Equation 29). The abrupt increase in K_H of Sample 19 could be due to the glass-ceramic nature of the material, which would also explain the difference between Sample 8 and Sample 9. Nonetheless, K_W exhibited more clear

trends in agreement with other mechanical and thermo-mechanical characterisations and had more contained variations. Therefore, K_W was preferred as parameter to describe the thermal stability of the samples under investigation, for comparison with other glasses and for general considerations about the structure of the materials.

4.4.2   Thermo-mechanical and mechanical characterisations

The results of the determination of the viscosity curve, CTE, C_p and H_v for Se-GLS glasses are summarised in Table 9 and plotted on ternary phase diagrams (Figure 36 and Figure 37). Figure 35 shows result of the fitting of the experimental viscosity curves to Equation 39 for samples containing 30 mol% La_2S_3. The fittings resulted in a good agreement between the T_g and the theoretical viscosity of $10^{13} dPa \cdot s$ characteristic of glasses at T_g. [59] In order to compare the effect of Se in the range of compositions, the softening point defined as $T_{\eta = 10^{6.7}}$ was considered. It was noticed that as the concentration of Ga_2Se_3 increased the softening point followed the same trend observed for K_W with a local maximum located at 40 mol% Ga_2Se_3. A wider analysis revealed this trend consistently for CTE and H_v. The trends observed for CTE, viscosity, Hv and K_W at low levels of Ga_2Se_3 may be due to the substitution of La-S by La-Se bonds that weakened the properties of the material. However, as the concentration approached 40 mol% all the features studied reached a local maximum. To explain this observation different aspects where considered. This trend could result from the formation of Se-S bonds known to be stronger than Ga-S and Ga-Se bonds.[57] However, this hypothesis could not account for the CTE of all the samples being larger than regular GLS glass. Since the formation of stronger bonds should reduce the CTE the contribution of metal–selenium bonds played a major role in the observation of the thermal expansion.
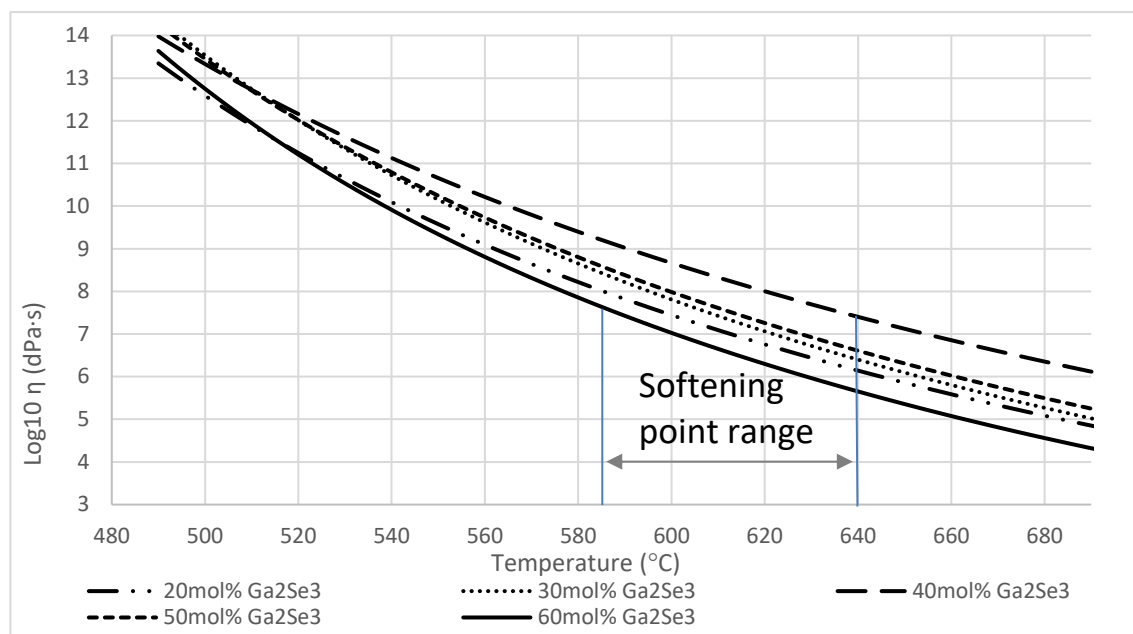
Figure 35: Viscosity curves resulted from fitting to Equation 39.

Table 9: Softening point, CTE, Cp and Hv for Se-GLS glasses.

Sample number	$T_{\eta=10^{6.7}}$ [°C]	a	b	CTE [10^{-6} °C^{-1}]	Cp [KJ/(g·°C)]	Hv [Kg$_f$·mm^{-2}]
1	651	5697	199	6.69	0.39	334
2	631	4993	235	9.94	0.38	316
3	625	4346	280	9.92	0.30	274
4	589	4755	212	10.4	0.34	303
5	660	5919	190	1.06	0.38	334
6	599	5252	182	9.70	0.31	-
7	604	4252	267	9.78	0.30	286
8	591	4927	200	8.97	0.34	-
9	586	3729	290	9.56	0.33	251
10[1,3]	567	3479	291	8.47	0.25	308
11[1]	596	5145	187	7.76	0.39	335
12	607	5597	163	12.9	0.43	383
13[2]	691	8712	0	9.61	0.35	270
14[1]	622	4494	265	1.06	0.37	274

1(Contained particles); 2(Phase separation); 3(Produced with RF furnace)

A more comprehensive description of the Ga-S and Ga-Se systems and how their properties vary with composition can be presented using a binary phase diagrams.[152], [153] Both systems are characterised by several eutectic points and one distectic point corresponding to the transition from GaSe to Ga_2Se_3. The distectic point is defined as the point in a phase diagram where a given composition has a higher melting point than the elements taken separately and usually occurs as a maximum point. In theory, a locally increased melting point may explain the local maxima found for the thermal and thermo-mechanical properties of Se-GLS glasses. However, the melting point of the glass forming samples did not follow the same trend not supporting this hypothesis. Therefore, in order to confirm this hypothesis deeper compositional studies are necessary since many other features appear within the binary phase diagrams. In addition, the binary plots did not take into account the effect of the presence of multiple elements within the same system and they could represent only a local behaviour within the glass.
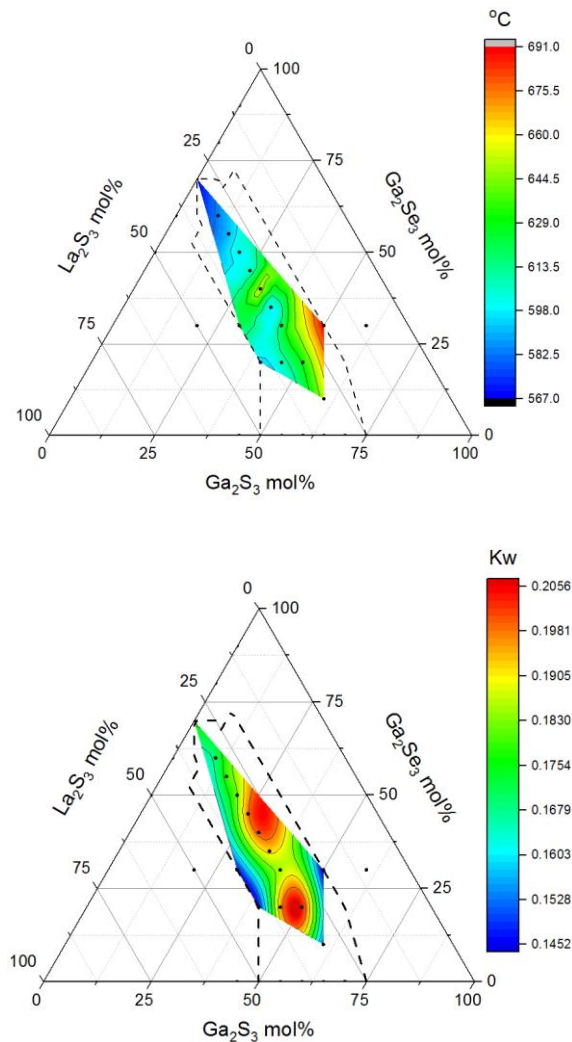
Figure 36: Phase diagrams representing the trends of the softening point and Weinberg parameter.
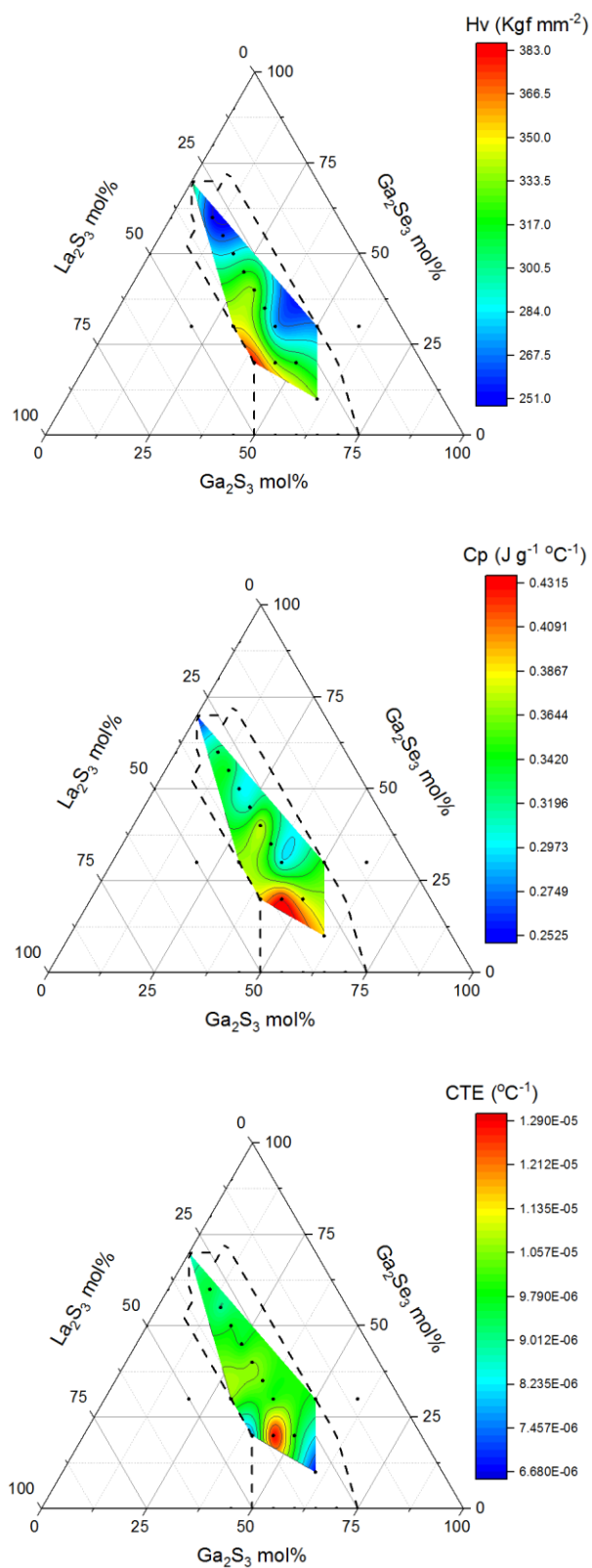
Figure 37: Phase diagrams representing the trends of the Hv, c_p and CTE.

4.4.3   Comparison of modified GLS glasses and commercial chalcogenides

In this section, the results obtained from the characterisation of the modified-GLS glasses are compared to commercial glasses with the aim of achieving a comprehensive understanding of the capabilities of the glasses with well-established materials as benchmarks. In particular, commercial chalcogenide glasses represent the materials about which a sufficient level of knowledge has been developed to allow large scale production and distribution. This comparison is needed to understand the requirements of users within research environments and eventual commercial uses of these glasses. For glasses with compositions that are still at a laboratory-level of development a comparison would not be as reliable since the results found in literature often lack of repeatability. Particular focus is put on the thermal, mechanical and thermo-mechanical properties since they determine the type of manufacturing processes and the possible applications. Table 10 summarises the data available from manufacturers of chalcogenide glasses and the glasses of this study.

Table 10: Summary of thermal, mechanical and thermo-mechanical properties for commercial chalcogenide glasses and modified-GLS glasses. * = composition not disclosed.

Glass	Source	T_g (^{o}C)	$T_{\eta=10^{6.7}}$ Pa·s	H_v Kgf/mm^2	C_p J/(g·cm^3)	CTE 10^{-6} ^{o}C^{-1}
1	This work	512	595	316	0.38	9.94
4	This work	500	605	274	0.30	9.92
8	This work	497	586	286	0.30	9.78
16	This work	529	-	354	-	12.9
18	This work	499	602	320	-	12.7
19	This work	453	-	329	-	-
$Ge_{33}As_{12}Se_{55}$	Amorphous materials Inc.	362	405	157	0.29	12.0
AsSe	Amorphous materials Inc.	167	188	96	0.28	22.4
$As_{40}S_{60}$	Amorphous materials Inc.	180	208	95	0.46	21.4
GASIR 1*	Umicore EOM NV	292	-	170	0.36	17.0
GASIR 5*	Umicore EOM NV	180	-	144	0.36	23.5
$Ge_{33}As_{12}Se_{55}$	VITRON GmbH	368	445	127	0.33	12.1
$Ge_{30}As_{13}Se_{32}Te_{25}$	VITRON GmbH	275	360	122	0.32	13.4
$Ge_{10}As_{40}Se_{50}$	VITRON GmbH	225	310	98	0.37	20.4
$Ge_{28}Sb_{12}Se_{60}$	VITRON GmbH	285	348	99	0.33	14.0
$As_{40}Se_{60}$	VITRON GmbH	185	236	93	0.36	20.7

The data provided by the manufacturers of commercial products showed a variability due to the purity of the glass and the techniques used to measure each parameter. For instance, the glass with composition $Ge_{33}As_{12}Se_{55}$ produced by two different manufactures had minor differences in T_g (362 °C and 368 °C) and CTE (12.0 and 12.1) mainly caused by the different amount of impurities contained and the experimental error associated with the measurements. However, a major difference can be observed in the softening point (405 °C and 455 °C) and Vickers hardness (157 Kgf/mm^2 and 127 Kgf/mm^2) which would need further details to be comprehensively explained. Therefore, the comparison between these glasses and the modified-GLS samples was done from a general perspective and not considering the glasses singularly.

The comparison of the thermal performance was done considering T_g and the softening point. Both these characteristic temperatures were found to be substantially higher than those for the commercial chalcogenides. This could due to the content of La in GLS glass, forming stronger bonds with S and Se than those between the semimetals and chalcogens forming the other chalcogenide glasses.[57] The same principle could explain the significantly higher Vickers Hardness and the smaller expansion coefficient. However, the results obtained for the specific heat capacity are close to the values supplied for industrial glasses which could be due to a less pronounced impact of La to this feature. In general, the comparison shows that GLS-based glasses could have a comparable performance to commercial glasses and could match the features required for the production of optical components with the current manufacturing techniques. The higher characteristic temperatures could be suitable for applications at high temperatures, whilst the improved strength suggest the possibility for this glass to be shaped into lenses and prisms. These results could be the incipit for future research on the optics and photonics of this glass.

4.5   Conclusion

The results obtained from the thermal and mechanical characterisation of modified GLS glasses have been discussed and compared to well-developed chalcogenide glasses available in the market. The modification to the chemistry of regular GLS glass mainly consisted of the substitution of Ga-S and La-S bonds with weaker Ga-Se and La-Se bonds. As a result, the thermal analysis revealed a decrease of the characteristic temperatures when any of Se, Te and In were added to GLS glass. The addition of selenium did not affect the characteristic temperatures dramatically as almost all the compositions exhibited glass transition above 500°C. A more pronounced variation was observed for high levels of Ga_2Se_3 with the minimum T_g observed at 466°C for full substitution of Ga_2S_3 by Ga_2Se_3. On the other end, significant changes were found when In_2S_3 replaced Ga_2S_3 up to 30 mol% with a minimum T_g of 420°C. Nevertheless, the thermal

stability of the glasses represented as the Weinberg parameter showed an improvement from regular GLS glass. This was due to the increase in T_x-T_g gap and the decrease in melting temperature. Further investigations on the Weinberg parameter, viscosity and CTE on Se-added GLS revealed these properties to follow analogous trends with all the parameters exhibiting a local maximum at 40 mol% Ga_2Se_3 content. This behaviour was found to be consistent with phase transitions highlighted in the phase diagrams of GaS and GaSe systems. However, further investigations are needed to clarify the occurrence of this behaviour.

Finally, the results were compared to the commercial benchmarks reported in Table 10. In general, GLS-based glasses showed comparable or better characteristics than commercial glasses. These features could make these investigated compositions promising materials for future applications such as lenses moulding and fibre drawing. However, as discussed in Chapter 3 further efforts have to be spent on the improvements of purity of the glasses in order to match the optical performance of commercial glasses.

Chapter 5

Spectroscopy of Rare Earth-doped Se-GLS glasses

5.1   Introduction

The development of rare earth doped glasses attracted significant interest and research efforts after Er^{3+}-doped silica glass was employed in optical fibre amplifiers.[154], [155] Particularly, alternative amplifiers at wavelengths outside the C-band of fibre telecommunication were sought due to the large chromatic dispersion associated with this band.[156] For instance, glasses comprised of Pr^{3+}, Dy^{3+} and Bi^{2+} were studied for their emission at 1.3 μm corresponding to the less dispersive O-band of SiO_2 glass.[157]–[159] However, the low loss of silica glass at 1550 nm was the factor determining the success of the EDFA for telecommunications in spite the higher dispersion. Buk glasses with lower optical losses than silica include fluoride-based materials, but these lack robust mechanical properties and exhibit moisture sensitivity.[33] Therefore, silica glass combines physical and chemical properties making this the dominant material for applications in telecommunications. However, the high phonon energy of silica around 1150 cm^{-1} represents a limitation for IR devices.[160] In particular, in RE-doped materials the middle-IR and LWIR emissions are due to electronic transitions over small energy gaps and molecular vibrations can bridge these transitions very efficiently with a non-radiative mechanism. The low phonon energy of chalcogenides decreases the rate of these non-radiative decays allowing the observation of IR emissions. In addition, it determines the transparency in the mid-IR and LWIR, which is essential for an efficient light emission. The high refractive index and density of chalcogenide glasses results in large absorption and emission cross-sections helping to increase the intensity of the light emitted.[161]

The applications of IR devices comprised of RE-doped chalcogenides span over a wide number of fields including sensing, environmental monitoring, range finding and medical treatment.[161] However, the investigation on the spectral properties of REs in chalcogenides are required prior to the development of mid-IR emitting devices.[45] Since the last century, the emissions in the mid-IR by several RE-doped glasses have been reported but the only glass with which lasing was achieved is Nd^{3+}-doped GLS fibres.[30], [32], [162]–[165][30][30][30][30] The device consisted of a core-clad fibre pumped at 815 nm and exhibiting laser emission at 1080nm. The observed lasing threshold obeyed the equation:[166]

$$P_{th} = \frac{h\nu_{em} A I_{RT}}{\eta_p \sigma_{em} \tau}$$

<div align="right">Equation 41</div>

where *A* is the beam cross-sectional are corresponding to the diameter of the core of the fibre, I_{rt} is the round-trip power loss, $h\nu_{em}$ is the energy of the pumping radiation, η_p is the pump efficiency, σ_{em} the emission cross section and τ is the excited state lifetime. The strong covalent character of chalcogenides is known to affect the excited state lifetime increasing the pump power threshold.[26], [100] Since $P_{th} \propto A$, this issue was tackled manufacturing glasses in fibre form reducing the beam area. The geometry of the fibre can be engineered to achieve good pump intensity in the fibre core overcoming the issue of weak absorption bands.[32] As a result, a pump power threshold ranging between 50 mW and 200 mW was applied using output couplers with a reflectivity of 93% and 99.5%, respectively.

The superior thermal and mechanical properties of Se-GLS with respect to many chalcogenide glasses have been discussed in the previous chapters. Similarly to GLS glass, Se-GLS glass has the capability to host a large amount of rare earth but it also has the potential to be drawn into fibres with extended IR transmission compared to GLS glass. These factors are expected to play in favour of the observation of emission bands in the LWIR. However, the spectroscopy of the bulk material has to be characterised prior to the design of optical devices. In particular, the wavelengths and width of the emitted bands, the excited state lifetime and the effect of the concentration have to be determined. The goal of this study was to determine the optimal concentration of Nd^{3+} and Er^{3+} in Se-GLS glasses containing 20 mol% Ga_2Se_3. As will be described in Section 5.2.1, high concentrations of dopant promote cross-relaxation in Nd^{3+} decreasing the excited state lifetime with detrimental effects on the efficiency of the emission. Similarly, high concentrations of Er^{3+} cause the clustering of the ions reducing the radiative lifetime. However, the Er^{3+}-doped samples presented a more complex emission mechanism which included co-operative up-conversion and radiation trapping. Each effect contributed to the measured excited state lifetime as will be described in the following sections. For both the dopants, the optimal concentration of dopant could be assumed as the one maximising the excited state lifetime and minimising the pump power threshold according to Equation 41. Future work may follow-up to this investigation attempting to achieve lasing in Nd^{3+}-doped Se-GLS as done with regular GLS. Furthermore, the understanding of the dynamics involved in the spectroscopy of Er^{3+}-doped Se-GLS could enhance works to exploit the many IR bands emitted by this ion.

5.2   Properties of rare earths and doped glasses

The electronic configuration of lanthanides gives rise to a unique combination of chemical and spectral properties. Lanthanide ions (Ln) are commonly observed with the oxidation state +3 as this is most stable configuration.[167] Different oxidation states such as in Eu^{2+} have been reported but are known to be less stable.[168] In their triply ionised form (Ln^{3+}), lanthanides are characterised by the same electronic configuration of xenon. The 3+ charge arises from the removal of electrons from 6s, 5d and 4f orbitals. As a result, the Ln^{3+} ions possess an unfilled 4f shell shielded by 6s and 5p orbitals. The shielding of 4f electrons is responsible for several effects, including the so-called "Lanthanide contraction" and the chemical inertia of 4f electrons, which makes the spectral properties of Ln^{3+} sharp, well defined and virtually independent from the Crystal Field (CF) of the host.[169] However, a deeper analysis of the distribution of the energy levels of 4f orbitals reveals CF to have a stronger influence than expected. This can be observed considering a Ln^{3+} ion as an impurity immersed in the glass host. From a quantum mechanical perspective, the Hamiltonian of the ions corresponds to that of the free ion perturbed by the electric field of the CF. This results as:

$$H = H_K + H_e + H_C + H_{SO} + H_{CF}$$

Equation 42

where H_K is the kinetic energy of the electrons, H_e is the potential energy of the electrons in the field of the nucleus, H_C is the Coulomb repulsion between pairs of electrons, H_{SO} is the spin-orbit interaction and H_{CF} is the perturbation of the CF.[170] The first four terms of this equation represent the Hamiltonian of the free ion. The Coulomb interaction is responsible for removing the degeneracy between the spin angular momentum (S) and the orbital angular momentum (L) producing different SL states. On the other hand, the spin-orbit coupling allows the interaction between SL states removing the degeneracy in the total angular momentum (J). The impact of the host material is contained in the factor H_{CF}. Indeed, the electric field resulting from the CF provokes further splitting known as the Stark effect.[170] In addition, when the host is comprised of elements with orbitals that overlap strongly with those of Ln^{3+}, the neuphelaxetic effect is observed. Due to this effect, the f orbitals tend to expand resulting in a decrease in energy of the f-f transitions. This effect is more pronounced in covalent materials.[167], [171] Generally, strongly covalent materials such as chalcogenides are also characterised by a high refractive index to which corresponds a short excited state lifetime.[32]
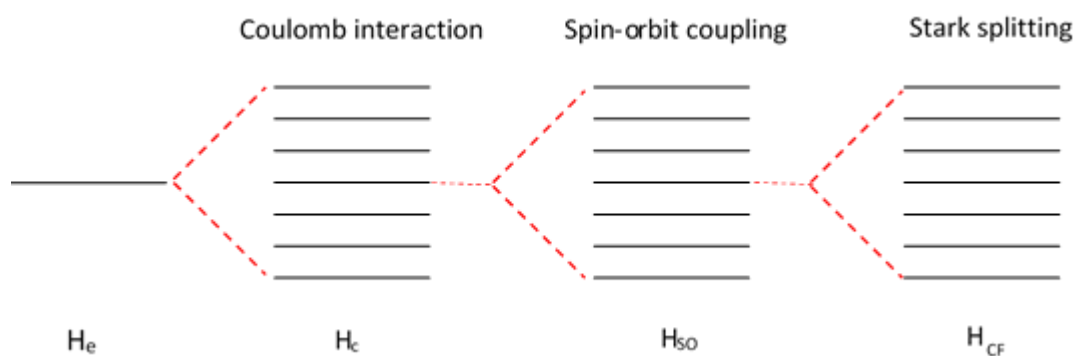
Figure 38: Schematics of the splitings occurring in RE-doped materials.

The absorption bands observed in Ln^{3+}-doped materials are mainly due to electronic transitions of electrons in 4f orbitals. Both Magnetic Dipole (MD) and Electric Dipole (ED) sources can excite these transitions. According to the selection rules, the MD transitions are parity-allowed whilst ED transitions are parity forbidden. Therefore, ED transitions within energy states of 4f orbitals are formally forbidden and low in intensity. Since ED intensity are weak, MD transition become observable in Ln^{3+}. The intensity of ED transitions can be increased if the coordination sphere of the ion has not a centre of symmetry, causing asymmetry of the molecular vibrations and a change in the parity of the ED transitions. The f-f transition in rare earths follow additional selection rules binding S, L and J as outlined in Table 11.[172]

Table 11: Selectrion for the electronic transitions in RE.

Transition	ΔS	ΔL	ΔJ
ED	0	≤ 6	≤ 6
MD	0	0	0, ± 1

A third type of transitions obeying to the selection rules for quadrupole transitions ($\Delta S=0$, $\Delta L \leq 2$, $\Delta J \leq 2$) can be observed. These transitions are called "hypersensitive" due to the large variation in Absorption cross-section they exhibit in different hosts.[173] This effect is known to be originated by the combined contribution of the geometry of the Ln site, the covalency and the inhomogeneous polarizability of the host. These interact with the electric field of the incident radiation increasing the intensity of the quadrupole transition.[101], [174] Some examples of hypersensitive transition can be $^4I_{15/2} \rightarrow {}^4G_{11/2}$ and $^4I_{15/2} \rightarrow {}^2H_{11/2}$ of Er^{3+}, as well as the transition $^4I_{9/2} \rightarrow {}^2G_{7/2}$ of Nd^{3+}.[175], [176] These transitions are usually not observed in chalcogenide glasses as these align with the band gap. In oxide materials, these absorption bands are excluded from the calculation of the Judd-Ofelt parameters since the large variation in intensity often give raise to a significant error.[175], [177]

5.2.1   Optimisation of Rare Earth glass for optical applications

In order to tailor the properties of active optical devices such as fibre and waveguide lasers and amplifiers, preliminary studies of the doped material are needed. Indeed, it is necessary to investigate the characteristic of the electronic transitions in the host and to determine the occurrence of detrimental side effects. This is usually done measuring the refractive index of the host, absorption spectrum of doped glass and the excited state lifetime of an emissions of interest. The results are then adopted in a loop scheme for Rare-Earth host optimisation formulated by Tanabe (Figure 39).[178], [179] The absorption cross-section can be calculated from the absorption spectrum whilst the theoretical radiative lifetime can be calculated carrying out the Judd-Ofelt analysis (Section 5.4.1). Comparing the calculated radiative lifetime and the measured radiative lifetime, the impact of non-radiative mechanisms and other side effects can be estimated. In addition, the Radiative Quantum Efficiency can be calculated. The data are then interpreted to have an overview of the properties of the material to subsequently proceed to modify the composition as necessary.
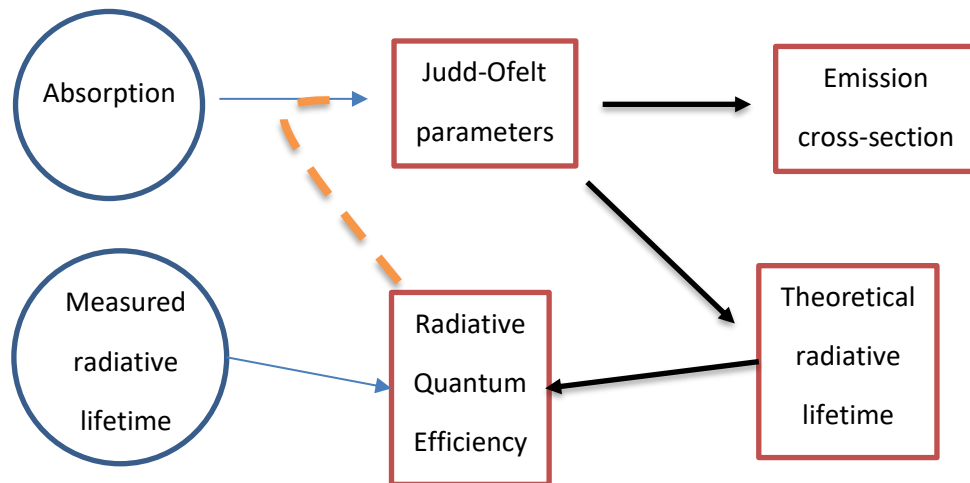
Figure 39: RE-doped optimisation algorithm formulated by Tanabe.

This research scheme is often associated with a systematic investigation on the impact of the concentration to the performance of the doped material. An excessive concentration of the dopant affects the radiative lifetime promoting the cross-relaxation of the excited electrons and clustering of dopant ions. The mechanism of cross relaxation is shown in Figure 40 taking Nd^{3+} as an example.[100] Generally, it involves one ion populating an excited state transferring part of its energy to neighbouring ion in a lower energy state. This mechanism has a significant impact on the transition $^4F_{3/2} \rightarrow {}^4I_{11/2}$ of Nd^{3+} as the ion excited to the level $^4F_{3/2}$ donates energy to another ion in the ground state. As a result, both ions end to the energy level $^4I_{15/2}$ possessing an energy around 6148 cm^{-1} quickly decaying to the ground state through non-radiative transitions.[100] As the concentration of the dopant increases, the distance between dopant ions decreases

facilitating the occurrence of cross-relaxation. The cross relaxation rate is found to be independent from the pump power since it can be initiated by just one non-excited ion. Additionally, cross-relaxation is manifested as a non-exponential fluorescence decay for extremely high concentrations of dopant.[100]

In Er^{3+}-doped materials, clustering has been recognised as the prominent process causing the quenching of excited state lifetimes.[180] Furthermore, co-operative up-conversion was observed. This occurs when a donor ion in a given excited state transfers energy to an acceptor ion lying in the same energy level. It results in the acceptor ion being doubly excited and the donor ions converted to the ground state. In Er^{3+}-doped materials co-operative up-conversion followed the mechanism in Figure 41 and exhibited the emission of green light at 533nm. Since rate of this mechanism depends on the population in the excited state, co-operative up-conversion was not significant for a low pump power. However, for a high pump power the rate of up-conversion significantly accelerated dramatically affecting the performance of optical devices.[180] The low phonon energy of chalcogenides also enhances the co-operative up-conversion. Indeed, the transition $^4I_{11/2} \rightarrow {}^4I_{13/2}$ occurs over a small energy gap. Although in oxide glasses it is quickly bridged non-radiatively by phonons, in chalcogenide glasses this transition occurs with a much slower rate. This is due to the lower phonon energy of chalcogenides decreasing the efficiency of non-radiative decays and increasing the lifetime of the excited states. The net result of this effect is to enhance the interaction between ions in the level $^4I_{15/2}$. Furthermore, the Er^{3+} donor ions that decayed to the ground state can re-absorb part of the emitted light released by radiative transitions. This effect is known as radiation trapping (Figure 41) and is manifested as a delayed discharge of the energy from excited states and extended measured excited state lifetimes.[181], [182]
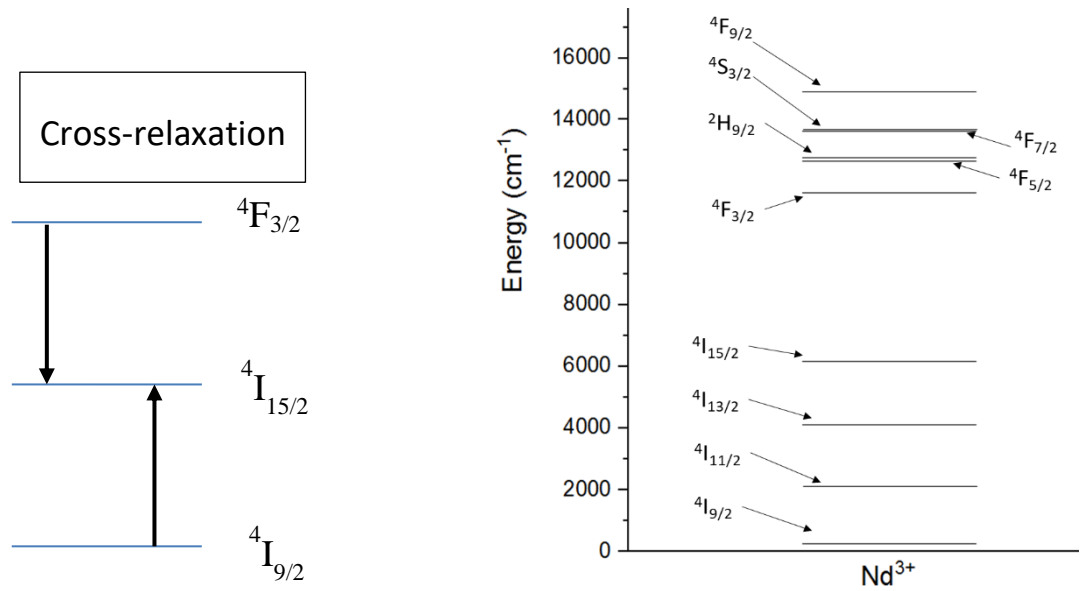
Figure 40: Energy level diagram and mechanism of cross-relaxation of Nd^{3+}.
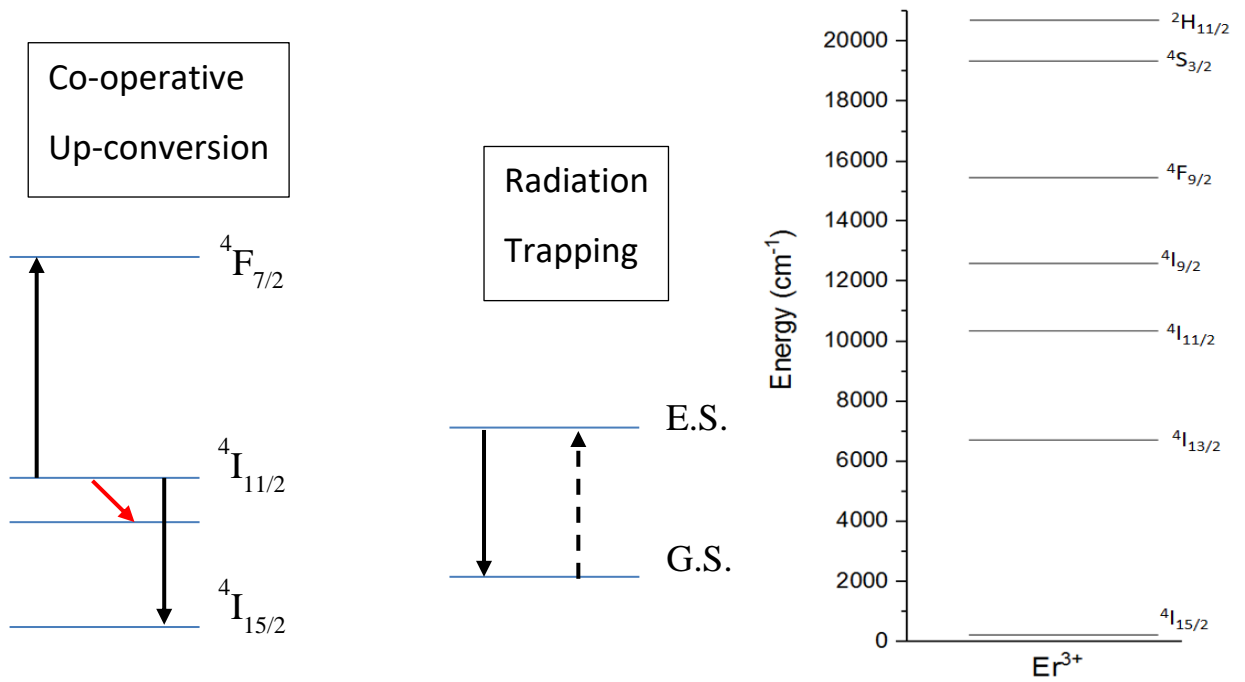
Figure 41: Energy level diagram, mechanism of co-operative up-conversion and radiation trapping of Er^{3+}. Note: the red arrow represents a non-radiative transition; the dashed arrow represents absorption of light by ions in the ground state.

In this work, two approaches have been adopted to investigate the features of Se-GLS glass as rare earth host. In the case of Nd^{3+}, the quenching effect of the concentration has been investigated fitting the experimental radiative lifetime of the transition $^4F_{3/2} \rightarrow {}^4I_{11/2}$ to the equation formulated by Auzel as described in Section 5.4.2.[182] In this way, the critical concentration of Nd^{3+} was determined as well as the theoretical lifetime. For the transition $^4I_{13/2} \rightarrow {}^4I_{15/2}$ of Er^{3+}-doped samples

a different version of the same equation was employed to account for the effect of the radiation trapping. The theoretical lifetime was compared to the value obtained with the Judd-Ofelt analysis to assess the quality of the fitting.

5.3   Experimental

The RE-doped Se-GLS samples were synthesised following the procedure described in Section 2.2 and the compositions are reported in Table 12: Composition, characteristic temperatures, Weinberg parameter, density and dopant ionic density of the studied samples.. The glass hosts were manufactured mixing high purity Ga_2S_3 (99.999%), Ga_2Se_3 (99.999%) and La_2S_3 (99.9%). The mixtures were added of Nd_2S_3 (99.9%) and Er_2O_3 (99.999%) in growing concentration substituting La_2S_3. In this way, the total concentration of RE sites in the samples was maintained almost constant. The samples containing 40 mol% Ga_2Se_3 and 60 mol% Ga_2Se_3 were doped with Er^{3+} to investigate the effect of Se on the re-absorption and the width of the emitted spectral band. The Raman spectra, characteristic temperatures, refractive index and transmission spectra were measured for each sample. This was done in order to assess any change in the structure of the glasses compared to the correspondent non-doped glass. The Raman spectra should reveal whether the maximum phonon energy of the glasses changed upon introduction of the dopant. Moreover, in case of changes in the structure of the glass network, the thermal characterisation should report substantial changes in the position of the onset of T_g, T_m and T_x. The density of the samples was measured in order to calculate accurate values of absorption and emission cross-sections. This was determined by the Archimedes' method using distilled water as immersion fluid. The ionic concentration of the dopant was calculated as:

$$N = \frac{m_{dopant}}{mw_{dopant}} \cdot N_A \cdot \frac{d}{m_{tot}}$$

Equation 43

where m_{dopant} is the mass of the dopant in the glass, mw_{dopant} is the molecular weight of the dopant, N_A is the Avogrado's Number, d is the density of the glass and m_{tot} is the total mass of the glass.

The spectral properties of the samples were investigated measuring the refractive indices, transmission spectra and the fluorescence spectra. For some of the emitted bands the P^n curves were measured correlating the incident pump power and the intensity of the emissions. In principle, these two parameters are correlated by an exponential relationship with the exponent n representing the number of photons involved in the emission.[183] In particular, for n = 1 the emission required the absorption of one photon without any interference of co-operative up-conversion. For n=2 the energy of two photon is required to observe the emission, which may result from two-photon absorption or the exchange of energy between neighbouring dopant ions.

Table 12: Composition, characteristic temperatures, Weinberg parameter, density and dopant ionic density of the studied samples.

Sample	Ga_2S_3 (wt%)	Ga_2Se_3 (wt%)	La_2S_3 (wt%)	Dopant (wt%)	Density (± 0.001 $g \cdot cm^{-3}$)	Dopant ionic density ($10^{19} cm^{-3}$)
20Se-GLS	38.60	24.66	36.74	-	-	-
$01Nd_2S_3$	38.31	24.77	36.78	0.14	4.249	1.91
$05Nd_2S_3$	38.57	25.00	35.82	0.60	4.228	8.06
$1Nd_2S_3$	38.40	25.02	35.30	1.26	4.245	16.10
$2.5Nd_2S_3$	38.71	24.49	33.70	3.11	4.233	21.70
$5Nd_2S_3$	38.64	24.53	30.46	6.36	4.269	85.20
$01Er_2O_3$	38.75	24.68	36.38	0.18	4.241	2.40
$05Er_2O_3$	38.44	24.81	36.11	0.64	4.263	8.61
$1Er_2O_3$	38.35	25.06	35.26	1.33	4.271	17.90
$2Er_2O_3$	38.50	24.75	34.26	2.49	4.207	35.10
40Se-GLS	20.21	45.15	33.63	-	-	-
$1Er_2O_3$-1	21.37	44.14	33.55	0.94	4.494	14.10
60Se-GLS	6.51	62.46	31.02	-	-	-
$1Er_2O_3$-2	6.37	6.19	30.71	1.03	4.679	15.00

The measurement of the emitted spectral lines and the P^n curves was carried out with the set up shown in Figure 42. The pump lasers used were operating at the wavelengths of 975 nm for Er^{3+} and 785 nm for Nd^{3+} irradiating the edge of the samples. The emitted light was collimated and focused into a monochromator (Jobin Yvon iHR320) with the aid of two planar-convex lenses matching the numerical aperture (NA) of the monochromator. The emission spectra in the near-infrared was detected with a Hamamatsu P4631-02 detector, whilst a Hamamatsu R928P detector was used for the emissions in the visible range. For the measurement of the excited state lifetime, the pump light was modulated as a squared-wave with a frequency generator and the signal detected by an amplified detector (Thorlabs PDA10CS). The quality of the signal was further improved reducing the signal-to-noise ratio with a lock-in amplifier (Stanford Research Systems SR830 DP lock-in amplifier). The decay curves were recorded with a digital oscilloscope (Tektronix TDS350) and fitted to the equation of exponential decay:

$$I(t) = I_0 e^{-kt}$$

Equation 44

where I(t) is the intensity of the signal at the time t, I_0 is the intensity before the decay started, k it the decay constant and t is the time. The experimental data point were fitted to Equation 44 following the least square method.
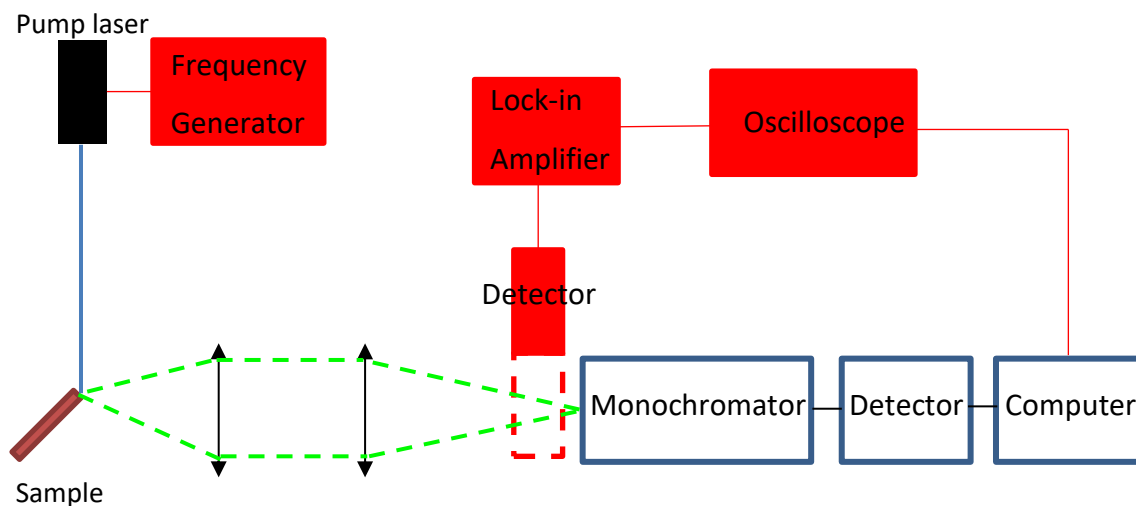
Figure 42: Set up used for the acquisition on fluorescence spectra and P^n curves (blue empty squares) and fluorescence lifetimes (red full squares). Note: optical equipment such as filters have been omitted.

5.4   Theoretical models

5.4.1   Judd-Ofelt Theory

The Judd-Ofelt (JO) theory aims to describe the intensity of the transitions occurring in Ln^{3+} from which parameters such as radiative lifetime and branching ratios can be obtained. The JO analysis allowed the calculation of the intensities of the transitions of RE in solids and solution and it has been used extensively to describe the behaviour of Rare Earths in crystals and glasses. The model is based on several approximations, namely static approximation, free-ion approximation and single configuration approximation.[184]–[186] The static approximation assumes the electric field produced by the CF to be static. The free-ion model treats the CF as a perturbation of the free-ion Hamiltonian. The single configuration approximation assumes the interaction between electrons with different configuration negligible. As a result, the intensity of the transitions expressed as theoretical line-strength S_t can be calculated as:

$$S_m = \sum_{i=2,4,6} \Omega_i |\langle a||U^{(i)}||b\rangle$$

Equation 45

where Ω_2, Ω_4, Ω_6 are the JO intensity parameters and $U^{(2)}$, $U^{(4)}$, $U^{(6)}$ are the reduced matrix elements for the intermediate coupling tabulated by Carnall.[187] The JO analysis requires accurate measurements of the absorption cross-sections and the refractive index of the material in the largest possible spectral range. The procedure adopted for the calculation of the JO parameters and the theoretical radiative lifetime was described by Walsh and was used to develop an appropriate Matlab script.[186], [188] Initially, the cross-section of absorption for each transition was calculated from the absorption spectrum of the sample as:

$$\sigma(\lambda) = \frac{-\ln\frac{T(\lambda)}{100}}{t \cdot N} \qquad \text{Equation 46}$$

where T is the transmittance of the sample, t is the thickness in cm and N is the ionic concentration of the dopant in cm^{-3}. The integral cross-section of absorption can then be used to calculate the measured line-strength S_m of a given transition, adopting the formula:

$$S_m = \frac{3ch(2J+1)}{8\pi^3 e^2 \lambda_{Avg}} n \left(\frac{3}{n^2+2}\right)^2 \int \sigma(\lambda)d\lambda \qquad \text{Equation 47}$$

where c is the speed of light, h is the Plank's constant, J is the quantum number representing the total angular momentum of the ground state, e is the charge of an electron in units of statcoulomb, $n(\lambda)$ is the refractive index, and λ_{Avg} is the average wavelength of the transition, calculated as:

$$\lambda_{Avg} = \frac{\sum \sigma(\lambda)}{\sum \lambda \sigma(\lambda)} \qquad \text{Equation 48}$$

The intensity parameters Ω_2, Ω_4, Ω_6 can be determined with a least square fitting minimising the squared difference between S_m and S_t. This can be expressed in matrix form as:

$$\sigma^2 = \sum_{j=1}^{N}\left(S_j^m - \sum_{i=1}^{3} M_{ij}\Omega_i\right) \qquad \text{Equation 49}$$

and minimised by calculating the derivative with respect to Ω equal to zero:

$$\frac{\delta(\sigma^2)}{\delta(\Omega_k)} = -2\sum_{j=1}^{N} M_{jk}\left(S_j^m - \sum_{i=1}^{3} M_{ij}\Omega_i\right) = 0 \qquad \text{Equation 50}$$

where σ is the deviation between S_m and S_t, M_{ij} is the matrix of N x 3 components containing the reduced matrix elements $U^{(i)}$ and M_{jk} is the transpose of the matrix M_{ij}. Following the procedure in Appendix F, it can be found that the set of Ω_2, Ω_4, Ω_6 that minimised the difference between S_m and

S_t is $\Omega = \left(M^T M\right)^{-1} M^T S_m$. The optimised JO parameters can be used to calculate the probability of spontaneous emission:

$$A(J',J) = \frac{64\pi^4 e^2}{3h(2J'+1)\lambda_{Avg}^3}\left[n\left(\frac{n^2+2}{3}\right)^2 S_{ED} + n^2 S_{MD}\right] \qquad \text{Equation 51}$$

where J' is the total angular momentum of the excited state, S_{ED} is the theoretical line-strength for electric dipole transitions and S_{MD} is the line-strength for magnetic dipole transitions. Since the contribution of the magnetic dipole transitions is usually small compared to the electric dipole transitions, S_{MD} has been approximated as described in previous works on Er^{3+}-doped GLS glass.[95] From A(J',J) the radiative lifetime τ and the branching ratio β can be calculated:

$$\tau = \frac{1}{A(J',J)} \qquad \text{Equation 52}$$

$$\beta = \frac{A(J',J)}{\sum_J A(J',J)} \qquad \text{Equation 53}$$

The error associated with the model can be calculated as the root-mean-square of the deviation between the measured and theoretical strength lines, following the formula:

$$\sigma_{rms} = \left(\frac{\sum(S_m - S_t)^2}{S_t^2}\right)^{1/2} \qquad \text{Equation 54}$$

The error associated with the JO analysis is usually between 15-20% and it can be substantially larger when the accuracy of the absorption spectrum is low. In addition, the least square method is more accurate for spectra showing a large number of transitions. This is a limiting for IR materials since the electronic edge tends to obscure the transitions in the visible range. In the case of GLSSe, the visible-range transitions can be observed up to 500nm improving the quality of the least square fitting. Previous works correlated Ω_2 with the covalency of the glass and this parameter is expected to decrease as the concentration of Se increases.[189] On the other hand, Ω_4 and Ω_6 depend on properties such as viscosity and dielectric of the media and vibronic interaction of the Ln^{3+} ions with surrounding atoms.[174], [175] Due to the variability reported for quadrupole transitions, these have not been included in the calculation of the JO parameters.

5.4.2   Auzel models

The models developed by Auzel aim to describe the effect of the concentration of the dopant on the excited state lifetime and can be used to optimise the concentration of the gain medium.[182]

As described in the Section 5.2.1, the contraction of the measured excited state lifetime as the concentration of Nd^{3+} increased is known to be due to cross-relaxation.[100] As depicted in Figure 40, cross-relaxation in Nd^{3+} involves the interaction between an ion at the excited state and an ion at the ground state exchanging energy. The decay from the level $^4I_{15/2}$ is non radiative and the net result consists of the pump light being converted into heat.[190] In materials with a high phonon energy such as oxide glasses, the rate of cross-relaxation tends to be high. As a result, the temperature of the gain medium quickly increases when pumped. The efficiency of cross-relaxation depends on the distance between ions, therefore the density of the material is an important factors to take into account. The measured excited state lifetime and the concentration are related by the equation:[182]

$$\tau(N) = \frac{\tau_0}{1 + \left(\frac{N}{0.83\,N_0}\right)^2} \qquad \text{Equation 55}$$

where $\tau(N)$ is the measured lifetime, τ_0 is the theoretical lifetime in absence of any cross-relaxation (i.e. single ion in the host material), N is the ionic concentration in cm^{-3} and N_0 is the quenching concentration. The parameters τ_0 and N_0 were found fitting the experimental data with the least square method. The study of the transition $^4I_{13/2} \rightarrow {}^4I_{15/2}$ of Er^{3+} required a different approach due to the different dynamics involved in the quenching of the excited state lifetime. This transition is usually studied pumping erbium doped glasses at 980 nm promoting ions from the ground state to the level $^4I_{11/2}$. Normally, Er^{3+} should undergo concentration quenching due to clustering resembling the behaviour observed for cross-relaxation. However, some of the ions are promptly up-converted from the level $^4I_{11/2}$ to $^4F_{7/2}$ exhibiting the emission of green light. As depicted in Figure 41, this process also results in a donor ion down-converted to the ground state. The ion decayed to the ground state can re-absorb the emitted light that matches the ground state absorption. As a result, the observed lifetime is far longer than expected and it tends to increase with the concentration.[191], [192] In principle, the issue can be overcome by grinding the sample minimising the volume of sample that interacts with the incident beam.[192] However, the sample in powder form would promptly absorb moisture and be oxidised changing the composition of the glass. It was found more convenient to quantify the effect the concentration on the measured lifetime with the equation:[181]

$$\tau_R = \tau_0 \left(1 + N\sigma_{abs}l\right) \qquad \text{Equation 56}$$

where τ_R is the lifetime in affected by re-absorption and l is the average absorption length. In order to account for both cross-relaxation and re-absorption, Equation 55 has to be multiplied by and Equation 56 giving:[181]

$$\tau_m = \frac{\tau_0 \, (1 \, + \, N \, \sigma_{abs} \, l)}{1 \, + \, \left(\dfrac{N}{0.83 \, N_0}\right)^2} \qquad\qquad \text{Equation 57}$$

The lifetimes measured were fitted to Equation 57 with the least square method calculating l, τ_0 and N_0 as fitting parameters bearing in mind that the validity condition is $N\sigma_{abs}l < 1$. The effect of re-absorption from the experimental data dividing by $(1+N\sigma_{abs}l)$ and extrapolating the corrected lifetimes. The corrected values can be fitted to Equation 55 using the same τ_0 and N_0 found with Equation 55. The results of this model were compared with the JO model to determine the accuracy of τ_0 and to investigate the trend for re-absorption as the concentration of Se is increased.

5.5   Results

5.5.1   Spectroscopy of Er^{3+}-doped Se-GLS glass

A structural comparison between the Er^{3+}-doped samples and the undoped Se-GLS glasses was carried out comparing the results of the TG-DTA. The characteristic temperatures of the undoped and doped glass samples are summarised in Table 13. The characteristic temperatures did not exhibit significant changes caused by the substitution of La^{3+} with Nd^{3+} and E^{r3}+. An increase of Tg was observed for all the samples that could be due to the greater melting point of Er$_2$O$_3$ and the change in the chemistry of the glass melt it caused.[29], [57]

The Tm did not undergo dramatic change which indicated that the structure of the doped samples was comparable to the one of the regular Se-GLS glasses. Further comparison wasmade calculating the Kw with Equation 29 to estimate the thermal stability of the samples.[59] The values of Kw observed for the Er^{3+}-doped samples were found to be comparable to those determined for the undoped glasses with exception of the sample containing 2 mol% Er$_2$O$_3$. This sample exhibited a contraction of the $T_x - T_g$ gap which may suggest a change in the structure due to the smaller ionic radius of Er^{3+}. It was also noticed that Kw remained well above than GLS glass used to build the only reported chalcogenide fibre laser.[30], [67] Therefore, the thermal properties of Er^{3+}-doped Se-GLS represent an improvement of GLS glass which may be suitable for fibre drawing and rare earth doped chalcogenide fibre laser. Raman spectroscopy was not employed for this purpose due to the strong absorption of Er^{3+} at the wavelength used by the available Raman spectrometer. In addition, the spectra exhibited a strong photoluminescence arising from the transition $^4S_{3/2} \rightarrow {}^4I_{15/2}$ that covered part of the Raman signal.

Table 13: Composition of the Er^{3+}-doped samples.

Sample	T_g (± 3 °C)	T_x (± 3 °C)	T_m (± 3 °C)	K_w	Density (±0.001 g·cm-3)
20Se-GLS	522	682	789	0.202	-
$01Er_2O_3$	525	672	789	0.197	4.241
$05Er_2O_3$	526	678	790	0.204	4.263
$1Er_2O_3$	523	689	790	0.203	4.271
$2Er_2O_3$	531	638	782	0.137	4.207
40Se-GLS	500	663	763	0.214	-
$1Er_2O_3$-1	508	665	762	0.207	4.494
60Se-GLS	486	627	767	0.184	-
$1Er_2O_3$-2	485	635	775	0.194	4.679

The absorption spectra of the samples $1Er_2O_3$, $1Er_2O_3$-1 and $1Er_2O_3$-2 are shown in Figure 43 in units of cross-section. The spectra of the samples $1Er_2O_3$-1 and $1Er_2O_3$-2 did not include the absorptions of the transitions $^4S_{3/2} \rightarrow {}^4I_{15/2}$ and $^2H_{11/2} \rightarrow {}^4I_{15/2}$ as these were covered by the band gap absorption. The bands centred at 1527nm and 663nm showed some variations in FWHM probably due to the change in the ionic density of the dopant. In addition, the maximum absorption cross-section was slightly increased by increasing the content of Se. As a result, the radiative lifetime is expected to decrease for increasing concentrations of Se.

Table 14: FWHM of some absorption bands of Er^{3+}-doped samples.

	Wavelengths of absorption			
	1527 nm	984 nm	808 nm	663 nm
Sample	FWHM (nm)	FWHM (nm)	FWHM (nm)	FWHM (nm)
$01Er_2O_3$	50.0	16	22	22.2
$1Er_2O_3$-1	55.8	14	20	26.2
$1Er_2O_3$-2	41.5	14	21	22.6
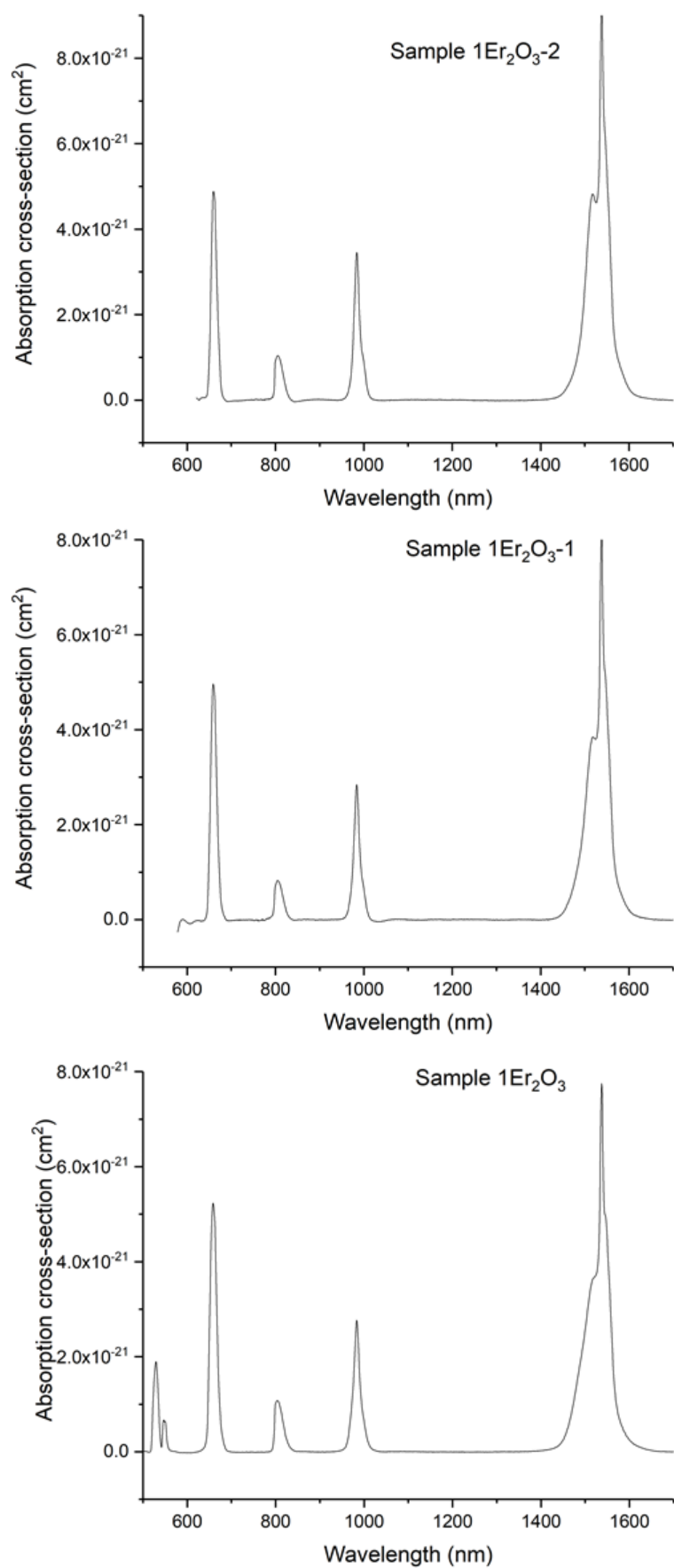
Figure 43: Absorption spectra of the samples 1Er$_2$O$_3$, 1Er$_2$O$_3$-1 and 1Er$_2$O$_3$-2.

The study on the fluorescence properties of the samples was done exciting the Er^{3+} ions to the level $^4I_{9/2}$ with a 975nm laser. As a result, the emission of light arising from the transition $^4I_{13/2} \rightarrow {}^4I_{15/2}$ was observed as well as the transitions $^4F_{9/2} \rightarrow {}^4I_{15/2}$, $^4S_{3/2} \rightarrow {}^4I_{15/2}$ and $^2H_{11/2} \rightarrow {}^4I_{15/2}$ falling into the visible range. The emitted radiations were studied correlating the incident pump power and the intensity of the emission expecting an exponential relationship. The exponent n was determined and represented the number of photons mediating the emission.[193] The normalised emission spectra and the P^n curves are shown in Figure 44. It was observed that the relative intensity of the emission at 665 nm increased significantly along with the concentration of Er^{3+}. As shown in the energy level diagram (Figure 41), the levels $^2H_{11/2}$ and $^4S_{3/2}$ are close to the electronic edge. As the concentration of Er_2O_3 increased, these energy levels may have been included in the electronic edge absorption. The Pn curves revealed all the Visible emissions to assume a value of n was around 2, proving that two photons from the pump were necessary to cause the emission (i.e. up-conversion). The value of n associated with the emission at 1527 nm was calculated around 1. This may suggest that the contribution of up-converted ions to this emission was negligible. Indeed, if any of the up-converted ions decayed to the level $^4I_{13/2}$ the value of n would be closer to 2. A similar observation was done for high levels of Ga_2Se_3 with the electronic edge located at 540 nm for the sample Er_2O_3-1 and at 565 nm for the sample Er_2O_3-2. In both cases, a fraction of the emission bands with wavelengths 530 and 550 nm may be absorbed by band gap absorption exhibiting the emission at 663nm as the most intense.
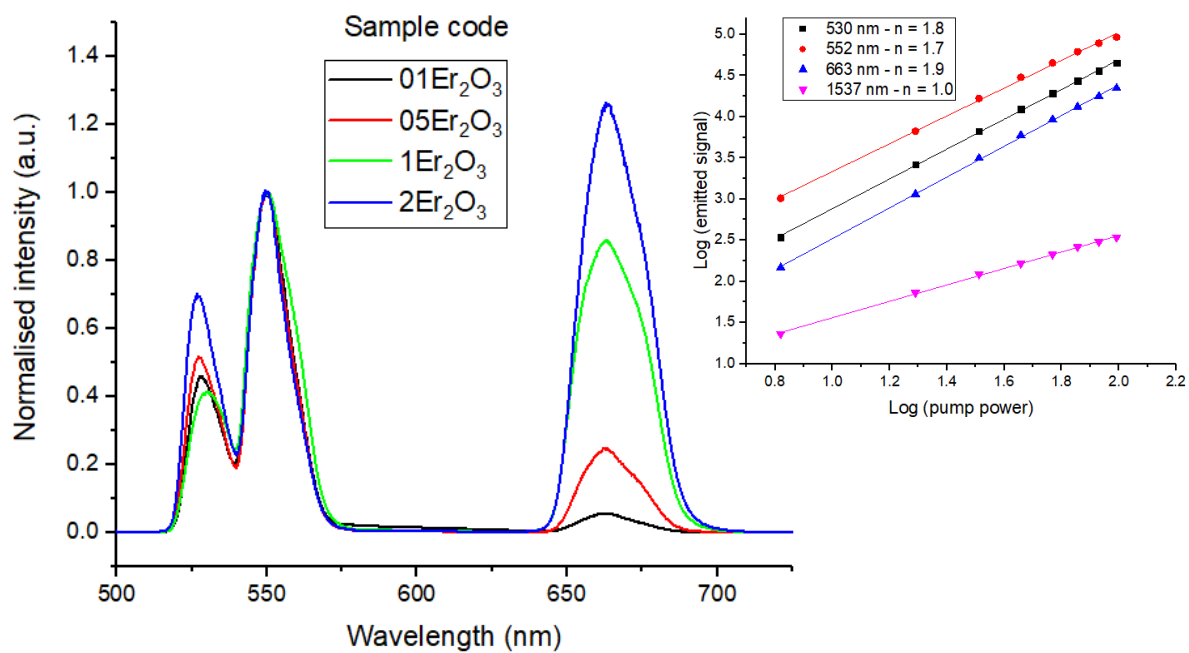
Figure 44: Visible emission spectra of Er^{3+}-doped samples comprised of 20mol% Ga_2Se_3 and P^n curves of the emissions of the sample $1Er_2O_3$.
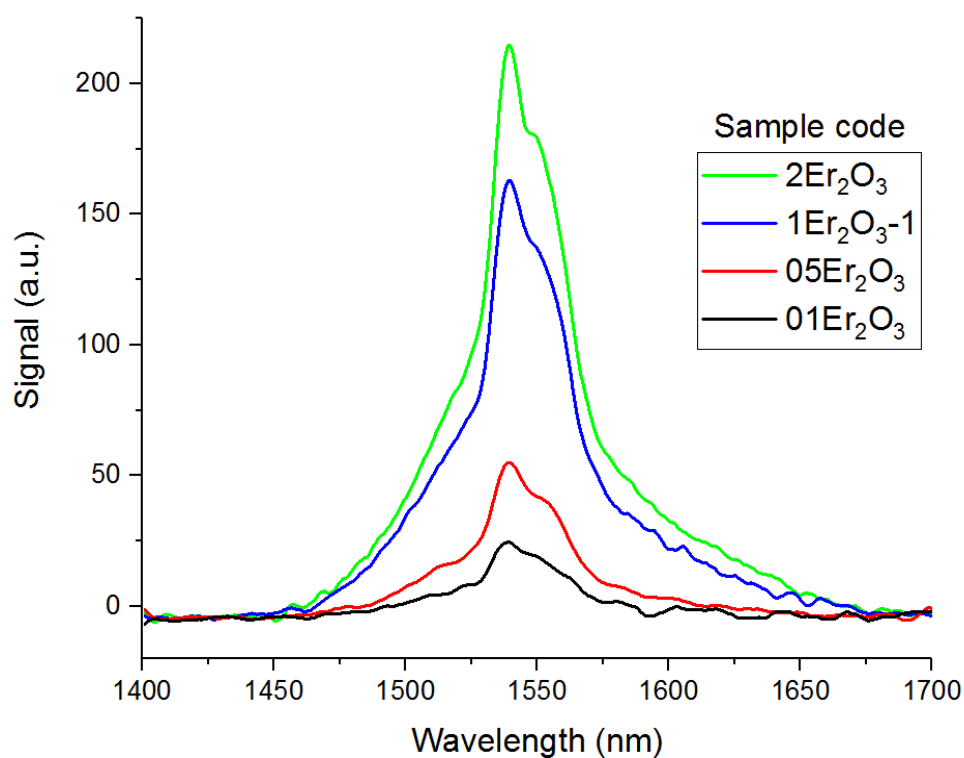
Figure 45: Emission band centred at 1527nm of Er^{3+}-doped samples comprised of 20mol%.
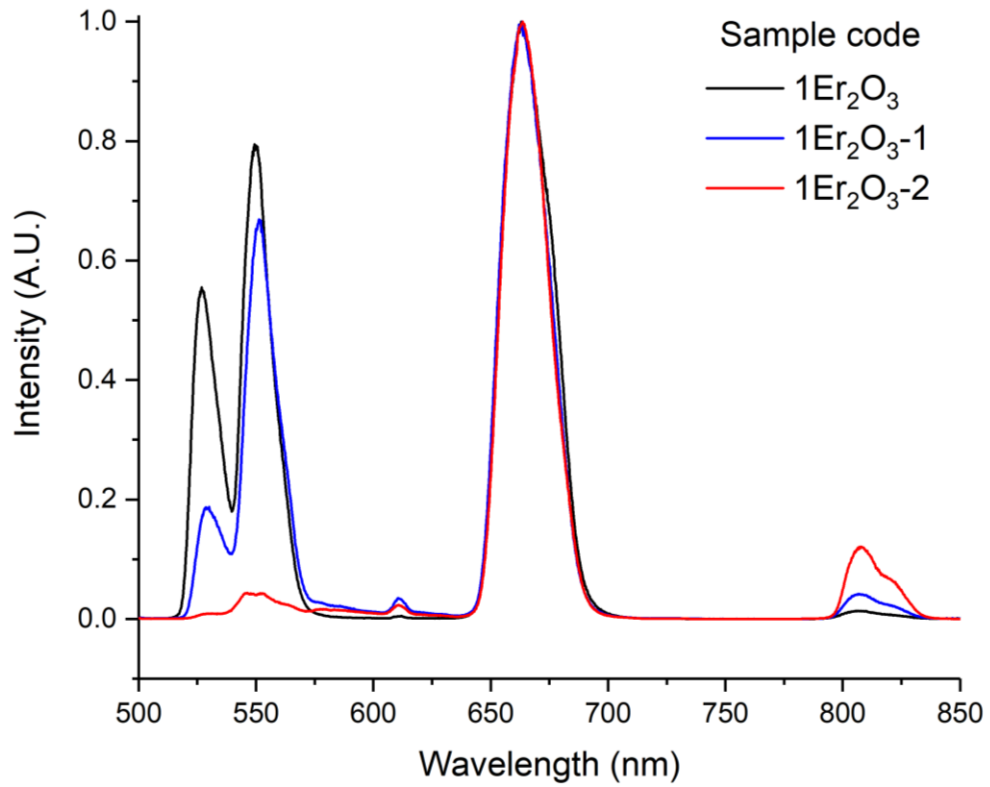
Figure 46: Emission spectra of Er^{3+}-doped samples Er_2O_3-1 and Er_2O_3-2.

It was then essential to determine whether the up-conversion was of a co-operative type (i.e. two ions interacting) or a two photon absorption (i.e. absorption of two irradiated photon without any interaction between Er^{3+} ions). This was done observing the variation of radiative lifetime for the transition $^4I_{13/2} \rightarrow {}^4I_{15/2}$ with the concentration. The first observation made was that the radiative lifetime increased with the concentration of dopant (Figure 47, left). This observation was attributed to the re-absorption caused by ions in the ground state, since the increase in concentration is expected to cause clustering. In addition, the radiative decay rate was found to be pump power dependent. These observations suggest that the up-conversion occurred via a co-operative mechanism. Indeed, if clustering was the prominent mechanism the decay rate would not be pump power dependent. Furthermore, since re-absorption requires ions in the ground state, a co-operative mechanism would explain the increase of measured lifetime with the concentration. Indeed, the donor ions involved in the co-operative mechanism are down-converted to the ground state and can absorb a fraction of the emissions. Moreover, as the concentration of the dopant grows, both clustering and the acceptor-donor interaction would be favoured. To confirm the simultaneous occurrence of clustering and re-absorption in Er^{3+}-doped samples, the radiative lifetimes were fitted to Equation 57. The fitting resulted in an agreement between with the equation (R^2=0.997) with σNl = 0.89, N_0 = 1.20·10^{21} cm^{-3} and τ_0 = 3.57 ms. The value of τ_0 was fund close to the lifetime calculated with the JO analysis (τ_{JO}) as reported in Table 15. The effect of re-absorption on the experimental lifetimes was eliminated dividing the data

points by (1+σNl) and fitting the results to Equation 55 (Figure 47). The new data points exhibited the trend expected for clustering proving the occurrence of this mechanism.
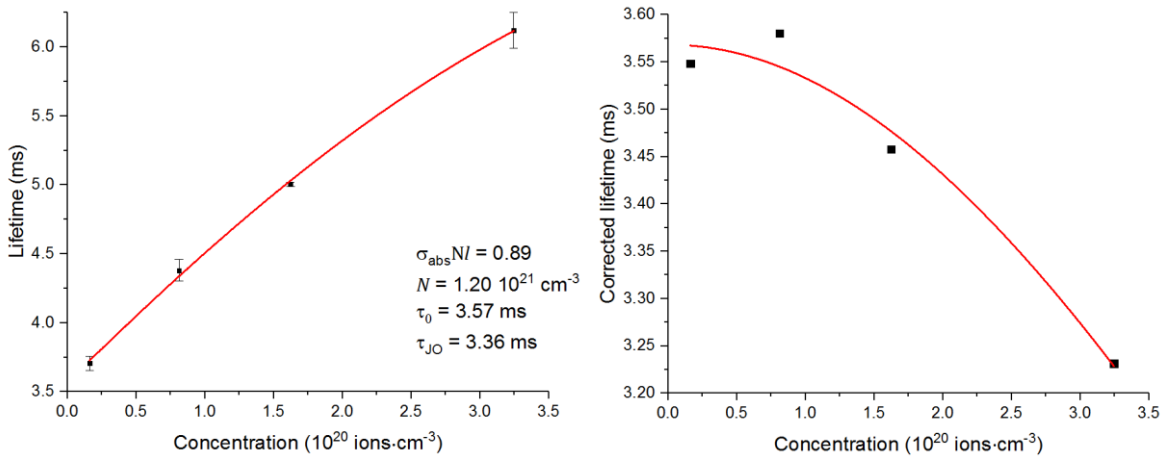
Figure 47: Left, fitting of the experimental excited state lifetime to Equation 57; Right, corrected lifetimes fitted to Equation 55.

Further evidence of the presence of re-absorption was obtained measuring the emission of the transition $^4I_{13/2} \rightarrow {}^4I_{15/2}$ in samples in powder form. As shown in Figure 48, the emission band of the samples in powder form is narrower than that for the bulk samples. This observation is typical of re-absorption and was reported in previous works on chalcogenide glasses.[194] Furthermore, for samples with 40 and 60 mol% Ga_2Se_3, the difference between the τ_{JO} and the measured lifetime increased with the content of Se (Table 15). A decreasing trend of τ_{JO} and an increasing trend of Ω_2 were expected as a result of the increase in covalency and refractive index of the samples.[195] On the other hand, the growing trend of the measured lifetimes suggests that the effect of re-absorption is stronger in materials with high refractive index.

Table 15: Values of τ_m, τ_s and JO parameters of Er^{3+}-doped samples.

Sample	$^4I_{13/2}$ τ_m (ms)	$^4I_{13/2}$ τ_{JO} (ms)	Ω_2 $(10^{-21}$ cm$^2)$	Ω_4 $(10_{-21}$ cm$^2)$	Ω_6 $(10^{-21}$ cm$^2)$
$01Er_2O_3$	3.61	-	-	-	-
$05Er_2O_3$	4.38	-	-	-	-
$1Er_2O_3$	5.07	3.37 ± 2.83%	2.218	9.309	9.305
$2Er_2O_3$	5.74	-	-	-	-
$1Er_2O_3$-1	5.96	3.26 ± 1.96%	1.799	6.815	8.160
$1Er_2O_3$-2	6.87	2.74 ± 7.39%	0.398	4.201	9.205

Note: the theoretical lifetime is expressed as τ_{JO} ± RMS error; the RMS error was calculated with Equation 54.
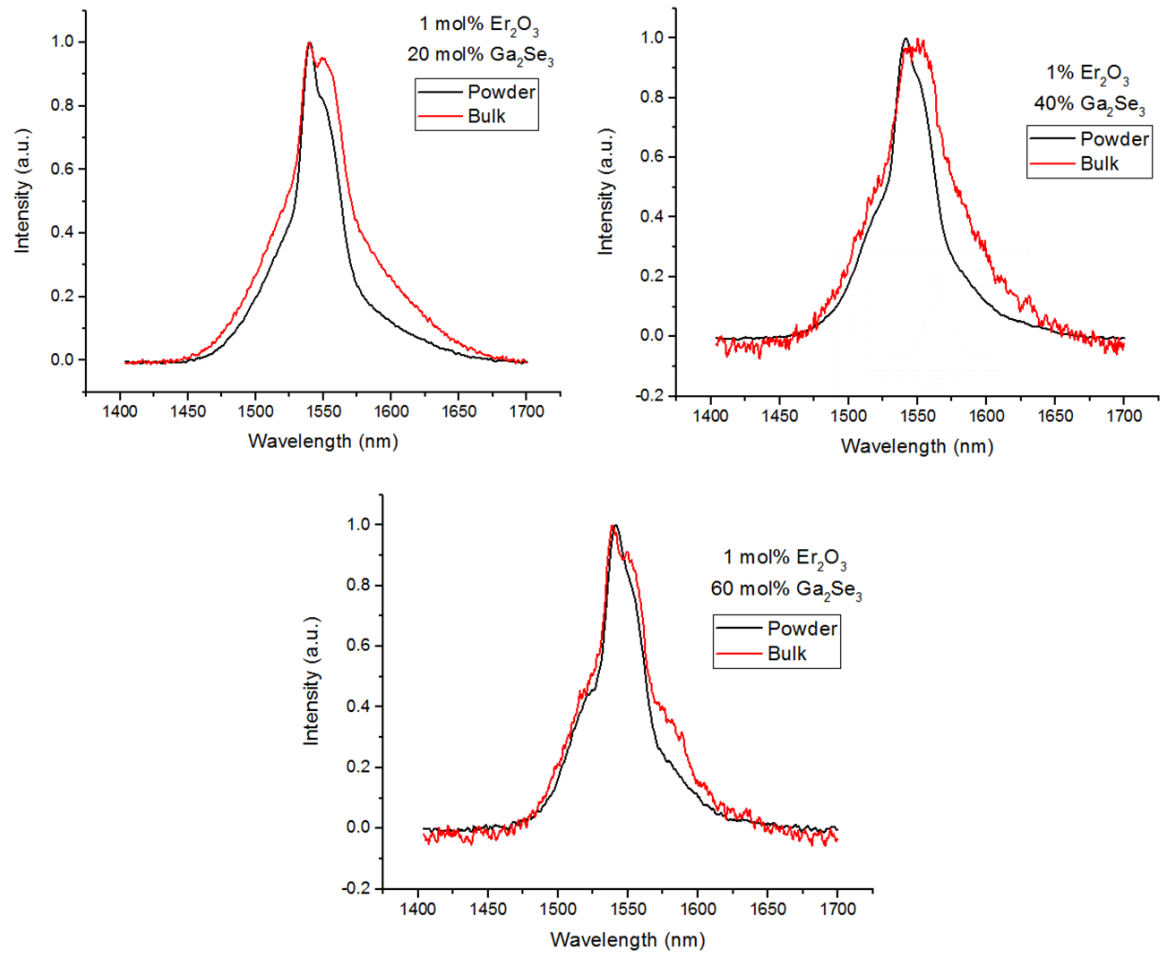
Figure 48: $^4I_{13/2}$ → $^4I_{15/2}$ transition in bulk and ground samples.

5.5.2 Spectroscopy of Nd^{3+}-doped Se-GLS glass

For the samples containing Nd^{3+} the results from Raman spectroscopy and TG-DTA were compared to these of the undoped samples. Figure 49 reports the comparison between the

Raman spectra of Nd^{3+}-doped and undoped Se-GLS glass. The increase of the concentration of Nd_2S_3 affected increased the intensity of the peak at 145 cm^{-1} assigned to La_2S_3.[70] The band relative to $GaSe_4$ between 200 and 300 cm^{-1} also increased in intensity, probably due to the overlap with the peak of Nd_2S_3 and the complexity of the glass network.[196], [197] On the other hand, the addition of Nd_2S_3 decreased the relative intensity of the GaS_4 peak between 300 cm^{-1} and 400 cm^{-1}. However, the energy of the Raman shifts did not change indicating that the structure of doped and undoped samples were analogous. The results of the thermal analysis are reported in Table 16. As found for Er^{3+}-doped samples, the characteristic temperatures did not undergo significant changes and value of K_W fluctuated due to the changed T_x-T_g gap. These observations confirmed that the structure of the glass did not change after the introduction of the dopant.

Table 16: Characteristic temperatures of Nd^{3+}-doped samples.

Sample	T_g (± 3 °C)	T_x (± 3 °C)	T_m (± 3 °C)	K_w
20Se-GLS	522	682	789	0.202
01Nd$_2$S$_3$	527	687	791	0.186
05Nd$_2$S$_3$	528	684	793	0.192
1Nd$_2$S$_3$	530	692	795	0.210
2.5Nd$_2$S$_3$	527	694	790	0.211
5Nd$_2$S$_3$	528	689	792	0.202
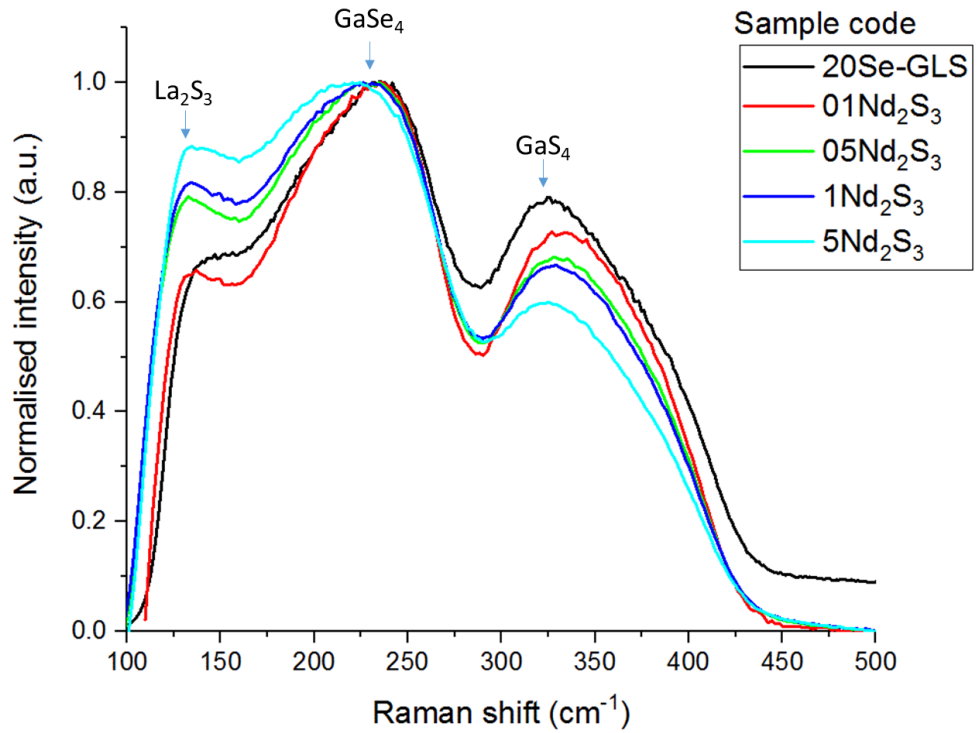
Figure 49: Raman spectra of regular Se-GLS and Nd^{3+}-doped samples.

The spectrum of Nd^{3+} in Se-GLS glass is shown in Figure 50 in units of absorption cross-section and also showing the schematics of the transition $^4F_{3/2} \rightarrow {}^4I_{11/2, \text{ the}}$ object of this investigation. The emission arising from this transition and the relative P^n curve are reported in Figure 51. The P^n curve was determined swinging the pump power from 34 to 231 mW. As shown in Figure 51 the slope of the log-log curve was calculated as 1, which excludes the occurrence of other radiative phenomena. The peak intensity of the emission was measured as 1087 nm exhibiting a red-shift from the emission of Nd-doped GLS at 1080 nm.[30] This shift could result from the nephelauxetic effect caused by the substitution of S by Se.[45],[198] Furthermore, the emission band was broadened as the concentration of Nd^{3+} grew. Since the broadening occurred predominantly at longer wavelengths, this observation could be due to the inhomogeneous broadening caused by the chemistry of the glass. Indeed, as the concentration of the dopant increases the ions occupy sites with different chemistry causing small changes in the emitted spectrum.[100] In addition, the broadening towards longer wavelengths may indicate that Nd^{3+} was located in sites with increased covalency, justifying the change in FWHM in comparison with other glasses.[198]
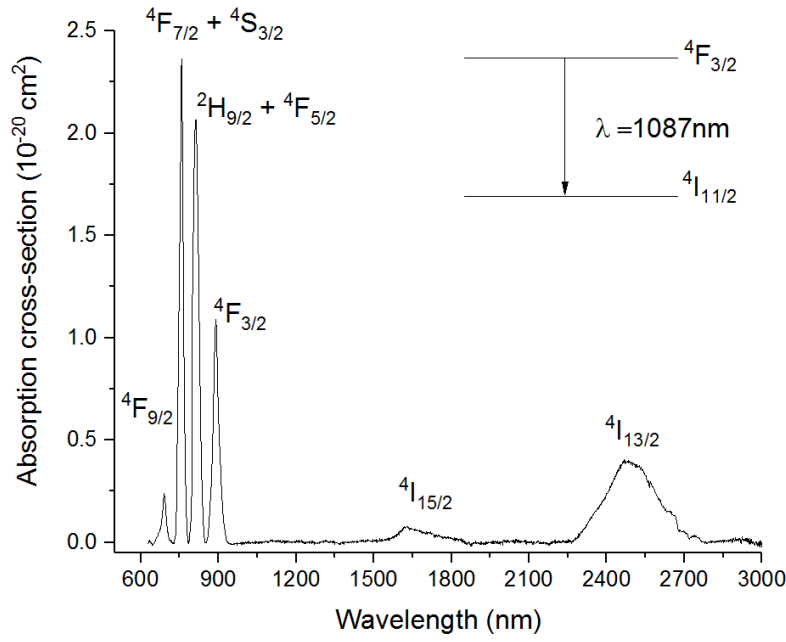
Figure 50: Absorption spectrum and schematics of the transition $^4F_{3/2} \rightarrow {}^4I_{11/2}$ in Nd^{3+}-doped samples.
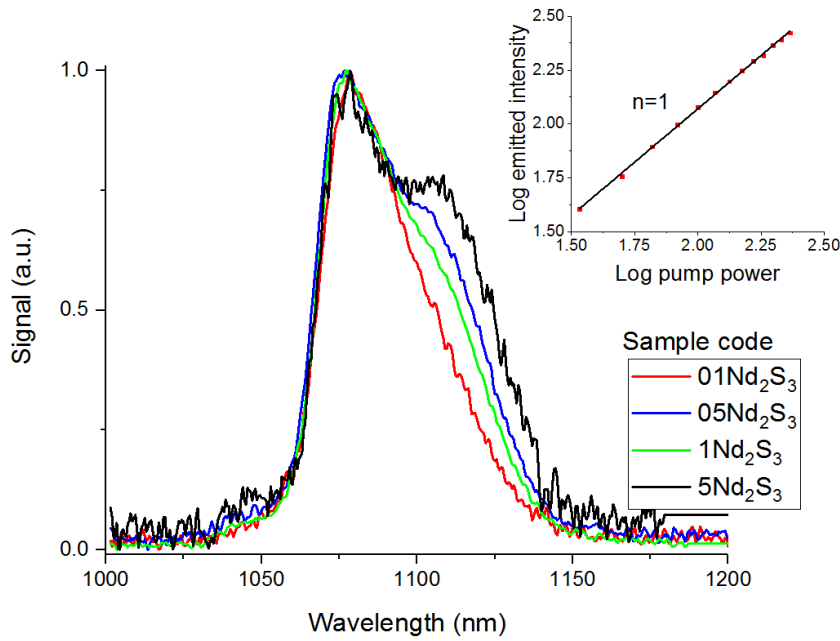
Figure 51: Emission band and P^n curve for the transition $^4F_{3/2} \rightarrow {}^4I_{11/2}$.

The effect of the concentration of the dopant on the measured lifetime of the transition $^4F_{3/2} \rightarrow {}^4I_{11/2}$ is reported in Figure 52. The occurrence of cross-relaxation was determined the shortening of the measured lifetime. This effect becomes stronger as the concentration of the dopant increases placing the ions closer to each other. The quenching effect of cross-relaxation can be quantified fitting the experimental lifetimes to Equation 55 determining τ_0 and N_0.[182] As a result, a τ_0 of 88 μs and N_0 of $4.7 \cdot 10^{20}$ ions·cm^{-3} were calculated. The value of τ_0 obtained

matched those reported for Nd^{3+}-doped chalcogenide glasses and was lower than those for oxide glasses.[30], [198]–[200] Optical materials with high refractive index and high $\sigma_{em}\tau$ product are known to have shorter excited state lifetimes.[100] However, the N_0 was found to be comparable to those reported for widely studied oxide such as silicates and phosphates and represent an unusual feature for chalcogenide glasses.[100] The good solubility of rare earths in GLS-based glasses is due to the capability of the lone pairs of S^{2-} to form a dative bond with the empty p-orbital of Ga^{3+}.[24] This same principle was adopted to increase the solubility of lanthanides in SiO_2 glass by the addition of Al_2O_3.[201] In addition, the large content of La^{3+} in GLS glasses can accommodate the substitution of this metal for other bulky ions such as Ln^{3+} and Na. In Se-GLS, a balance between the ionic character of La_2S_3 and the covalent character of Ga_2S_3 has to be kept in order to avoid devitrification.[65], [202] This aspect has to be taken into account while designing doped Se-GLS in order to avoid unwanted crystallisation upon irradiation by pump lasers.
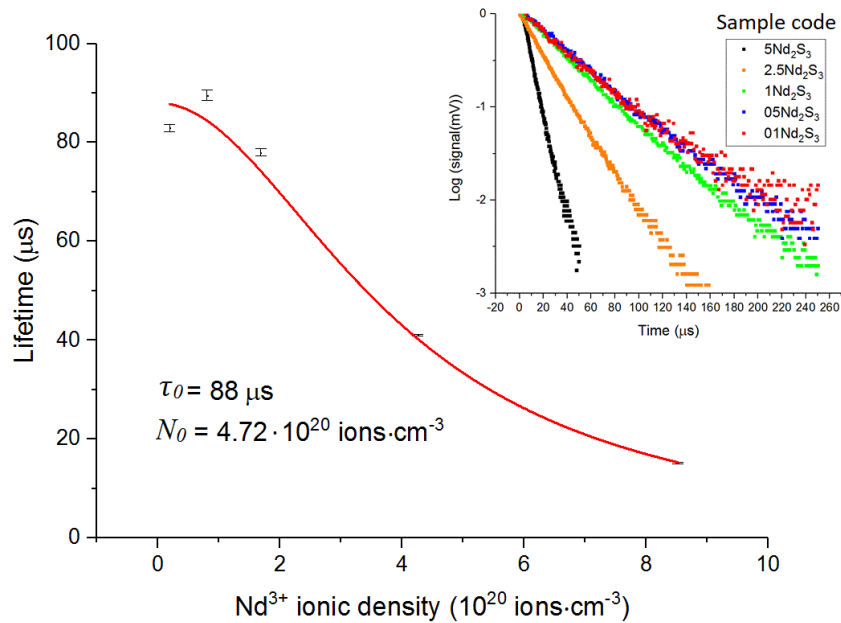
Figure 52: Decay curves and fitting to Equation 55 of the measured lifetimes of Nd^{3+} samples.

5.6   Conclusions

In this chapter, a detailed investigation on the spectroscopy of Er^{3+} and Nd^{3+} doped Se-GLS glasses is presented. The dopants were introduced in Se-GLS glass by substituting La^{3+} with Er^{3+} and Nd^{3+}. The effect of the dopants on the structure of the glass was assessed comparing Raman spectra, characteristic temperatures and K_w for doped and undoped samples. The analysis did not exhibit significant changes indicating similar structures. Particularly, the Raman spectra of Nd^{3+} doped samples comprised shifts within the energy range of Se-GLS glasses while the TG-DTA resulted in unchanged T_m. However, the thermal stability parameter K_w was subjected to some variability because of larger T_x-T_g. These changes can arise from the different chemistry of the dopants

which were also characterised by a higher melting point than La_2S_3. Nevertheless, the K_w for all the samples was higher than that reported for Nd^{3+}-doped GLS glass. Since Nd^{3+}-doped GLS is the only chalcogenide glass for which lasing of Nd^{3+} has been reported, the improved thermal properties of Se-GLS should not represent an obstacle in the application of this family of materials in active optical devices.

The spectral properties of Er^{3+} and Nd^{3+}-doped samples were investigated to determine the mechanisms governing emission of light and probe the features of Se-GLS as a rare earth host. As reported in previous works, the electronic transition $^4F_{3/2} \rightarrow {}^4I_{11/2}$ of Nd^{3+}-doped samples was characterised by cross-relaxation. This effect had a substantial effect on the measured lifetime as the concentration of the dopant increased. Equation 55 was employed to predict the impact of cross relaxation determining a theoretical lifetime τ_0 of 88 μs was and a critical concentration $N_0 = 1.20 \cdot 10^{21}$ cm^{-3}. The value of τ_0 was in good agreement with chalcogenide glasses, for which a lower lifetime than oxide glasses is observed due to the strongly covalent character of chalcogenides. This also produced a red-shifted emission peak found at 1087 nm against 1060 nm for silica.[198]

The study of the spectral properties of Er^{3+}-doped samples exhibited a complex dynamics of light emission. The investigation focused on the $^4I_{13/2} \rightarrow {}^4I_{15/2}$ transition, which showed an unexpectedly long measured lifetime increasing with the concentration of the dopant. This effect was due to a large fraction of emitted light being re-absorbed by ions in the ground state. This effect has been studied in past works, where effect of the re-absorption was attenuated measuring emission spectra and lifetime for samples in powder form. This strategy was adopted in this work and showed narrower emission bands for all the samples examined (Figure 48). However, the wide surface area of the powder promoted moisture absorption and oxidation of the material. Therefore, the impact of re-absorption was studied more conveniently fitting the experimental lifetimes to Equation 57. As a result, the values of τ_0 similar to the one predicted with Judd-Ofelt analysis. In addition, the gap between τ_0 and τ_{JO} increased with the concentration of Ga_2Se_3. This indicated that re-absorption became more pronounced as the covalent character of the material was strengthened. A mechanism causing re-absorption (Figure 41) was formulated correlating the observed up-conversion and extended lifetime of the samples. In particular, the emission of Er^{3+} at 1537 nm results from a three-level system including a non-radiative transition. Indeed, the transition $^4I_{11/2} \rightarrow {}^4I_{13/2}$ mediated by molecular vibrations. Due to the low phonon energy of chalcogenides, the rate of this non-radiative processes was lower allowing an efficient co-operative up-conversion. The donor ions involved in the co-operative up-conversion re-absorbed the light emitted in radiative decay. The longer lifetimes measured for samples with larger

amounts of Se supported this observation and proved the key role of the phonon energy in the co-operative up-conversion.

Future studies may focus on understanding further the role of the concentration. Particularly, the adoption of XPS may give information on the distance between ions and the chemistry of their coordination sphere. This work opened new possibilities for Se-GLS glass to be adopted in active optical devices such as lasers, amplifiers and sensing, as demonstrated for Nd^{3+}-doped GLS.[30] Furthermore, the large re-absorption observed in Er^{3+}-doped samples could be adopted to improve the performance of existing devices. For instance, Er^{3+} was proposed as an enhancer for laser gain media with re-absorption acting as an energy-storing process to decrease the pump power threshold. Furthermore, the possibility to tailor the of up-conversion in Er^{3+}-doped materials adopted in several studied to increase the efficiency of light harvesters.[203]–[205] Since chalcogenides are receiving considerable efforts for applications in energy production, doping chalcogenides with Ln^{3+} could improve their performance.

Chapter 5

Chapter 6

Final remarks and further works

The synthesis and the properties of GLS-based glasses comprised of Se, Te, In and CsCl with has been described. The results obtained demonstrated the fabrication of selenide glasses using open systems, unlike the sealed ampoule systems typically used with Se based glass. The process produced low losses in mass and it offered advantages in safety and ease of fabrication. The system allowed the employment of high purity and high melting precursors mixed and homogenised prior to melting. The substitution of S with Se and Te was achieved introducing Ga_2Se_3 and Ga_2Te_3 gradually decreasing the concentration of Ga_2S_3. The glass forming range observed for Se-GLS was substantially larger than that for Te-GLS. In particular, glass formation was observed for the composition 70 mol% Ga_2Se_3 - 30 mol% La_2S_3 where Ga_2S_3 was not in the mixture. The tie-line 70 mol% Ga_2Ch_3 - 30mol% La_2S_3 (Ch = S, Se) was also the most where the glass forming region was largest and without traces of phase separation. On the other hand, the variation of the ratio Ga_2S_3/La_2S_3 resulted in a small number of glass forming melts. A small glass forming region was also observed when Ga_2S_3 was replaced by In_2S_3, with amorphous samples up to 20 mol% of In_2S_3. The substitution of La_2S_3 for CsCl in Se-GLS produced glass-ceramic samples where the particles obscured the whole transmission window.

The optical properties of Se-GLS glasses demonstrated the use of this glass in multispectral applications. The most interesting optical features were observed in Se-GLS glasses, which exhibited visible to LWIR transmission in all the compositions studied. The sample containing 60 mol% Ga_2Se_3 exhibited transmission up to 16.62 µm with a Visible cut-off at 575 nm. This observation places Se-GLS glasses in the category of multispectral materials where only AsS has a visible-to-LWIR transmission window. However, AsS is still produced in sealed ampoules with risks of explosions and impurity trapping. Other multispectral materials are produced containing CsCl with the drawback of moisture sensitivity and ready devitrification.[27], [43], [75], [127] The investigation on the properties in the THz range resulted in strong changes in refractive index as the average polarisability of the materials increased. The measurement of n_2 exhibited similar results as the concentration of Se in the glass increased. The optical features for GLS added of 10 mol% Ga_2Te_3 were comparable to those of the sample containing 20 mol% Ga_2Se_3. However, the volatily of Te did not allow a full control of the glass melt and a large loss of mass was registered. The effect of In_2S_3 to GLSSe reduced the visible transmission with the cut-off edge of the sample containing 10 mol% In_2S_3 at 640 nm.

The results obtained from the thermal and mechanical characterisations have been discussed within the framework of the commercial chalcogenide glasses. The formation of weaker Ga-Se and La-Se bonds resulted in reduced characteristic temperatures and mechanical strength with respect of GLS glass. The lower T_g observed was 466°C for the sample 70 mol% Ga_2Se_3 - 30 mol% La_2S_3. Nonetheless, the thermal stability of the glasses was found to be better than undoped GLS glass due to the larger T_x-T_g gap. The compositional dependence of H_W, softening point, H_V and CTE of Se-added GLS showed a local maximum when the concentration of Ga_2Se_3 reached 40 mol%. This behaviour corresponded to the phase transitions of Ga-S and Ga-Se systems. The addition of In_2S_3 up to 30 mol% had significantly stronger effects with a minimum T_g of 420°C. The T_g for Te-GLS was higher than the 20 mol% Ga_2Se_3, indicating a higher energy barrier for the glass formation. The thermal and mechanical properties of GLS-based glasses were found to be superior to those for commercial chalcogenide glasses. This indicated the possibility to manufacture optical components with improved mechanical properties and higher temperature of operation.

In this thesis, a detailed investigation on the spectroscopy of Er^{3+} and Nd^{3+} doped Se-GLS glasses described. The dopants were introduced in Se-GLS glass substituting La^{3+} with Er^{3+} and Nd^{3+}. The effect of the dopants on the structure of the glass was assessed comparing Raman spectra, characteristic temperatures and Kw for doped and undoped samples. The analysis did not exhibit significant changes indicating similar structures. Particularly, the Raman spectra of Nd^{3+} doped samples comprised shifts within the energy range of Se-GLS glasses while the TG-DTA resulted in unchanged T_m. However, the thermal stability parameter Kw was subjected to some variability because of larger T_x-T_g. These changes can arise from the different chemistry of the dopants which were also characterised by a higher melting point than La_2S_3. Nevertheless, the Kw for all the samples was higher than that reported for Nd^{3+}-doped GLS glass. Since Nd3+-doped GLS is the only chalcogenide glass for which lasing of Nd^{3+} has been reported, the improved thermal properties of Se-GLS should not represent an obstacle in the application of this family of materials in active optical devices.

The spectral properties of Er^{3+} and Nd^{3+}-doped samples have been studied to investigate the mechanisms of light emission and evaluate Se-GLS as a rare earth host. The transition $^4F_{3/2} \rightarrow {}^4I_{11/2}$ of Nd^{3+}-doped samples emitted a band centred at 1087 nm. This was found at lower energy than Nd^{3+}-doped silica where the band is centred at 1060 nm. The effect of cross-relaxation substantially reduced the measured lifetime at high concentrations. The equations formulated by Auzel were used to estimate a theoretical lifetime τ_0 of 88 μs was and a critical concentration $N_0 = 1.20 \cdot 10^{21}$ cm^{-3}. Although the value of τ_0 was in comparable to other chalcogenide glasses, Se-GLS could host a significantly higher amount of Nd^{3+}. The spectral properties of Er^{3+}-doped samples exhibited a more complex scenario. The initial observation of suspiciously long lifetimes for the

transition $^4I_{13/2} \rightarrow {}^4I_{15/2}$ transition suggested the occurrence of radiation trapping. Since this effect is known to be produced by ions in the ground state and a large amount of green light was observed, co-operative operative upconversion was recognised as responsible for both observations. The experimental lifetimes were fitted to the Auzel equations and the results showed a good agreement between τ_0 and τ_{JO} and a high solubility of Er^{3+}. In addition, it was observed that for samples with high Se concentration the effect of reabsorption was stronger, proving the strong impact of the phonon energy in the mechanism of emission prposed.

The results presented in this thesis offer many perspective for future works. For instance, the melting apparatus can be improved to achieve higher quenching rates and better optical properties. Indeed, the glass forming region observed strictly depended on the quenching rate and increasing this parameter can enlarge the glass forming region of modified GLS glasses. This could be of particular interest for Te-GLS, which exhibited extended transmission in the IR for a low level of doping. This material also requires the development of a melting process to drastically reduce the losses of mass. Initial studied could be carried out with sealed systems in order to probe the properties of Te-GLS. The development of an improved melting system could also benefit the production of Se-GLS and In-GLS producing a larger range of glass forming compositions. Further efforts on the purification of the precursors should be spent in order to reach a comparable optical performance to that of commercial chalcogenides. The main impurities are oxides, probably coming from La_2S_3 since the La-O bond is the strongest in nature making La_2S_3 very hard to purify. Further investigations could be done to study the occurrence for all the thermal and mechanical properties of a local maximum at 40 mol% Ga_2Se_3. This challenge could be addressed adopting XPS to determine the distance between atoms and the type of bonding involved. This investigation could be also beneficial for RE-doped glasses to harvest information on the chemistry of the RE coordination sphere. This would correlate the effect of the concentration on the spectral properties and the effect of the chemistry of the emission bands.

Lastly, the properties of Se-GLS could be exploited to produce optical components for a variety of applications. The increased IR transmission and n_2 of Se-GLS could be used for supercontinuum generation. Since these non-linear effects were stronger than in regular GLS, the supercontinuum spectrum for Se-GLS is expected to be larger than the 3250 nm found with GLS in previous works. Such device could be developed in fibre form as well as waveguide and bulk.

The spectral properties of RE-doped GLS can be used to replicate the laser activity observed in Nd^{3+}-doped GLS and produce active optical devices in the mid-IR. Furthermore, the strong radiation trapping observed in Er^{3+}-doped Se-GLS could be exploited to improve the properties of devices such as the of light harvesters. Previous works demonstrated an increase in the efficiency upon doping with Er^{3+} giving a promising role to reabsorption.

The development of compact solutions for multispectral imaging could be another promising application. In particular, the design of lenses and other optical components to combine visible and LWIR light would be of interest as the current systems rely on two separate optical apparatuses.

Appendix A **Precursor purity analysis**

University of Southampton, Bulk Gases specifications

Bulk Gas Purification Tender Specifications

Package 1 – Argon and Nitrogen Bulk Gas Purifiers

The University of Southampton requires argon and nitrogen bulk gas purifiers to supply the building users with a full life cycle cost effective, guaranteed supply of process and purge gases via a centralised distribution system.

The successful bidder must be able to provide supporting documentation that demonstrates compliance with the specification outlined below. In addition, at least two references are required from customers who have similar systems installed within their facilities.

Incoming Supply Specification

Table 1 shows the maximum impurity levels found in the feed gas to the bulk purifiers; which are supplied from VIEs within the delivery yard via 'Ultron' seamless electro-polished 316 stainless steel pipework. The feed pressure of the system is between 5 and 7 bar.

Table 1 - Incoming gas supply specification for the bulk argon and nitrogen purifiers

Supply Gas	Maximum Impurity Levels							
	N_2 (ppb)	O_2 (ppb)	H_2 (ppb)	H_2O (ppb)	CO (ppb)	CO_2 (ppb)	THC CH4 (ppb)	Particles (pcs/scf @ 0.1 μm)
Argon (Ar)	--	1000	--	1000	1000	500	1000	10
Utility Nitrogen (UN_2)	--	2000	1000	5000	1500	500	1000	10

The system should include provision of incoming dew point sensors that have reliable performance to below -114°C (~1ppb H_2O) with a service life between recalibration of ≥13 months. The system shall include provision for the regular service change out of the humidity sensors without loss of gas quality or volume to the building.

Outgoing Supply Specification

Table 2 shows the specification of the outgoing supply after purification whilst table 3 gives average and peak flow rates that the system must be capable of handling. Potential suppliers should provide detailed information on the performance of their purifier, indicating all of the impurities removed by the system as well as the best and typical levels of each one after purification.

Table 2 - Outgoing gas supply specification for argon and nitrogen after purification

Supply Gas	Maximum Impurity Levels							
	N_2 (ppb)	O_2 (ppb)	H_2 (ppb)	H_2O (ppb)	CO (ppb)	CO_2 (ppb)	THC CH4 (ppb)	Particle Filtration (um)
High Purity Argon	<10	<10	<10	<10	<10	<10	<10	<0.01
High Purity Nitrogen	--	<10	<10	<10	<10	<10	<10	<0.01

The system should include provision of outgoing dew point sensors that have reliable performance to below -114°C (~1ppb H_2O) with a service life between recalibration of ≥13 months. The system shall include provision for the regular service change out of the humidity sensors without loss of gas quality or volume to the building.

Table 3 - Average and Peak flow rates for high purity nitrogen and argon

Gas	Average flow rate	Peak flow rate
High purity Nitrogen	40 m³/hr.	60m³/hr.
High purity Argon	0.5 m³/hr.	2 m³/hr.

Appendix A

Testbourne Ltd
Products for Industry, Research & Development

Unit C, The Loddon Centre
Wade Road, Basingstoke, Hampshire
RG24 8FL, England
Tel: +44 (0)1256 467055
Fax: +44 (0)1256 362 955
Email: info@testbourne.com

Certificate of Analysis

Product Description:

Part No.: G2-5009-M
Material: Gallium Selenide, Ga2Se3
Form: 1-6mm pieces

Purity:
99.999%

Customer Reference

Analysis method: ICP-ICP/MS

Contaminants reported as : Wt%

	Reported		Reported		Reported		Reported
Al	0.4	Eu		Nb		Si	<0.1
Ag	<0.1	Fe	0.2	Nd		Sr	
Au		Ga		Ni	<0.1	Ta	
As		Ge		Os		Te	0.3
B		Gd		P		Ti	
Be		Hf		Pb	0.3	Tl	
Ba		Hg	<0.1	Pd		Tm	
Br		Ho		Pr		Tb	
Bi	0.3	I		Pt		Th	
Ca		Ir		Rb		U	
Cl		In	<0.1	Re		V	
Cr		K		Ru		Y	
Co		La		Rh		Yb	
Cu	0.1	Li		S		W	
Cd	0.2	Lu		Sc		Zn	<0.1
Cs		Mg	0.2	Se		Zr	
Ce		Mn	0.2	Sb	0.2		
Dy		Mo		Sm		C	
Er		Na		Sn	<0.1	N	
						O	
						F	
						H	

Composition

wt%	Reported		Reported

19/04/2016	G Richards	G. Stromdale	BM TRADA
Date:	Completed By:	Approved:	ISO 9001:2008

Form 11/CG

Testbourne Ltd
Products for Industry, Research & Development

Unit C, The Loddon Centre
Wade Road, Basingstoke, Hampshire
RG24 8FL, England
Tel: +44 (0)1256 467055
Fax: +44 (0)1256 362955
Email: info@testbourne.com

Certificate of Analysis

Product Description:

Part No.: G2-9015-D3
Material: Gallium Telluride, Ga2Te3
Form: 50.8mm dia x 4mm thick target

Purity:
99.99%

LOT No
LOT000042

Analysis method: **ICP-OES**

Contaminants reported as : ppm

	Reported		Reported		Reported		Reported
Al	<10	Eu		Nb		Si	
Ag	<5	Fe	<10	Nd		Sr	
Au		Ga		Ni	<10	Ta	
As		Ge		Os		Te	
B		Gd		P		Ti	
Be		Hf		Pb	<10	Tl	
Ba		Hg		Pd		Tm	
Br		Ho		Pr		Tb	
Bi	<10	I		Pt		Th	
Ca		Ir		Rb		U	
Cl		In	<10	Re		V	
Cr		K		Ru		Y	
Co		La		Rh		Yb	
Cu	<10	Li		S		W	
Cd		Lu		Sc		Zn	
Cs		Mg	<10	Se		Zr	
Ce		Mn		Sb	<5		
Dy		Mo		Sm		C	
Er		Na		Sn		N	
						O	
						F	
						H	

Composition

wt%	Reported		Reported

23/06/2017
Date:

G Richards
Completed By:

G. Stromdale
Approved:

BM TRADA
ISO 9001:2008

NAGQF011

Form 11/CG

129

Appendix A

Appendix B **Principles of X-ray diffraction**

In X-Ray Diffraction the source of radiations is a cathode ray tube appropriately filtered to emit a monochromatic band. The beam is collimated and directed towards the sample which can be in powder form, a single crystal or a film. The interaction between the beam and the sample results in a constructive interference when the Bragg's Law is respected. The condition for constructive interference is:

$$n\lambda = 2dsin\theta$$

where *n* is an integer, λ is the wavelength, d is the distance between atomic layers and θ is the incident angle. Every material possess a unique set of factors *d*, which are correlated to the dimensions of the unit cell. The long-range regularity of crystal structures ensure a strong interference throughout the sample. In the case of glass, the molecular structure is not consistent and lacks of long-range repeatability of the geometrical parameters such as bonds length and angles. Therefore, the signal arising from XRD of glasses is found to be weak and broad. The lack of an order molecular arrangement decrease the amount of constructive interference, whilst *d* assumes a large number of values for the same atomic distance broadening the peaks.[206]
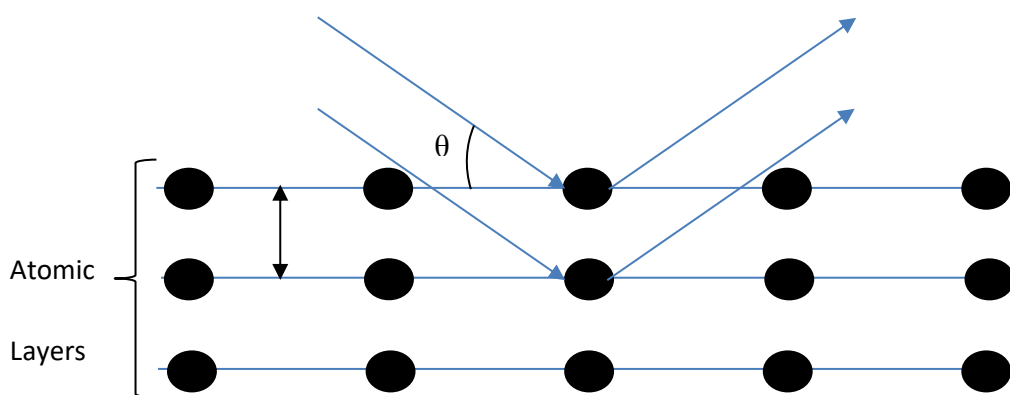

Figure 53: Schematics of the mecahnism of X-Ray diffraction

Appendix C   **Principles of Raman Spectroscopy**

The origin of the Raman spectra can be found in the interaction between light with frequency v_0 and molecular units of a material causing scattering of light. The light can be scattered by the molecule elastically or inelastically. The elastic scattering is Rayleigh scattering and it is the most probable. On the other hand, the Raman scattering in inelastic and represents 10^{-5} of the incident light. The frequency of the light arising from Raman scattering is $v_0 \pm v_m$, where v_m is the frequency of vibration of the molecule. In particular, the frequency $v_0 - v_m$ is known as Stokes line whilst the frequency $v_0 + v_m$ is the anti-Stokes line. Therefore, the vibrational frequency of the molecules are observed as a shift from the incident frequency. In order to observe a Raman shift the molecular vibration has to possess a non-null rate of change in polarizability. Therefore, the geometry of the molecule and the symmetry of the vibration are of vital importance. In particular, the polarizability ellipsoid of the molecule has to change size, shape or orientation as a consequence of the interaction.[68], [197] The Raman spectrum of a material in crystalline and amorphous form are different in broadness due to the geometry of the molecules. In crystals, every given molecular unit has a well defined geometry with bond lengths and angles repeated consistently. Therefore, the Raman shift will occur within a narrow range of frequencies producing a sharp peak. On the other hand, amorphous materials are intrinsically disorder and the geometrical features of the molecules are not constant. The shifts are exhibited as broad peaks centred in the same position of these for the material in crystal form. An example of this behaviours is showed in Figure 11.
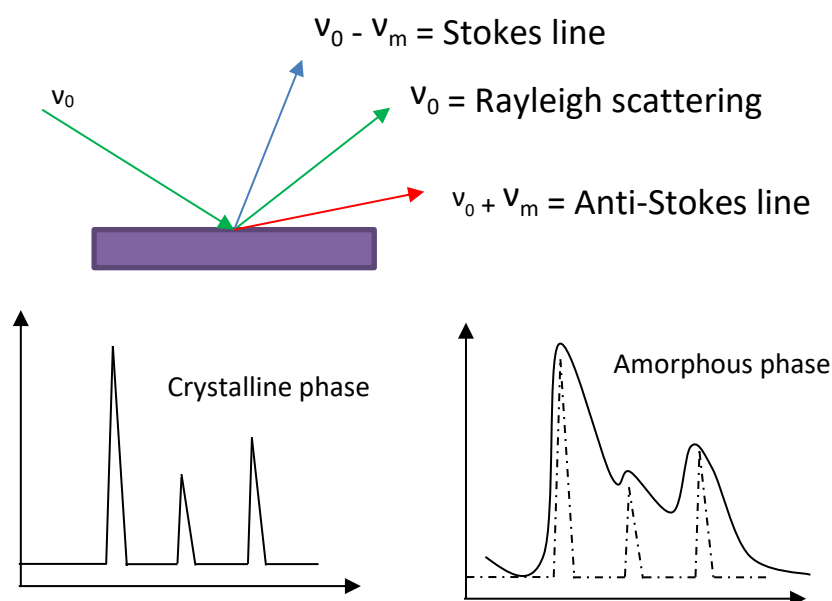
Figure 54: Schematics of Raman effect and examples of spectra for crystalline and amorphous spectra.

Appendix D   FTIR and UV-Visible spectra

Figure 55: Transmission spectrum of the sample with composition 20 mol% Ga_2Se_3 – 50 mol%Ga_2S_3 – 30 mol% La_2S_3.

Figure 56: Transmission spectrum of the sample with composition 30 mol% Ga_2Se_3 – 40 mol%Ga_2S_3 – 30 mol% La_2S_3.
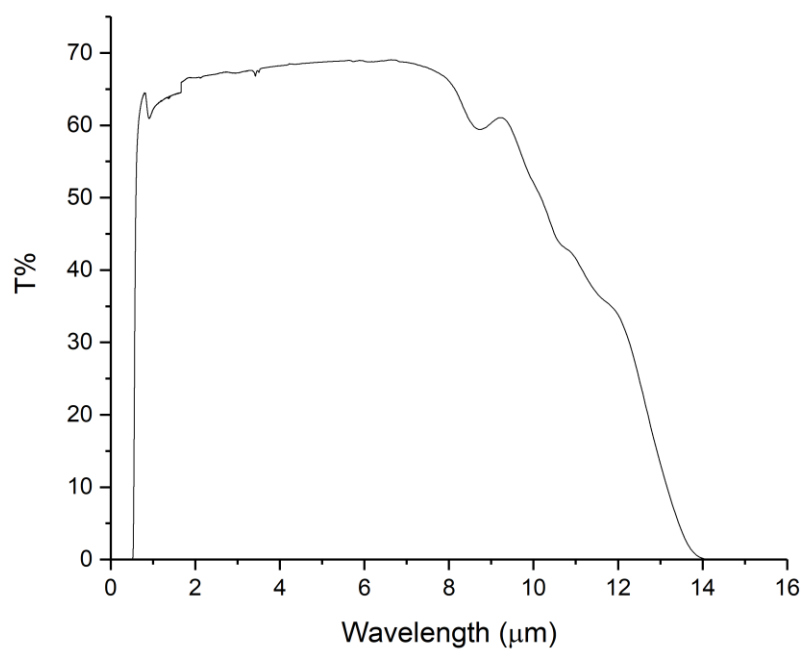
Figure 57: Transmission spectrum of the sample with composition 35 mol% Ga_2Se_3 – 35 mol%Ga_2S_3 – 30 mol% La_2S_3.
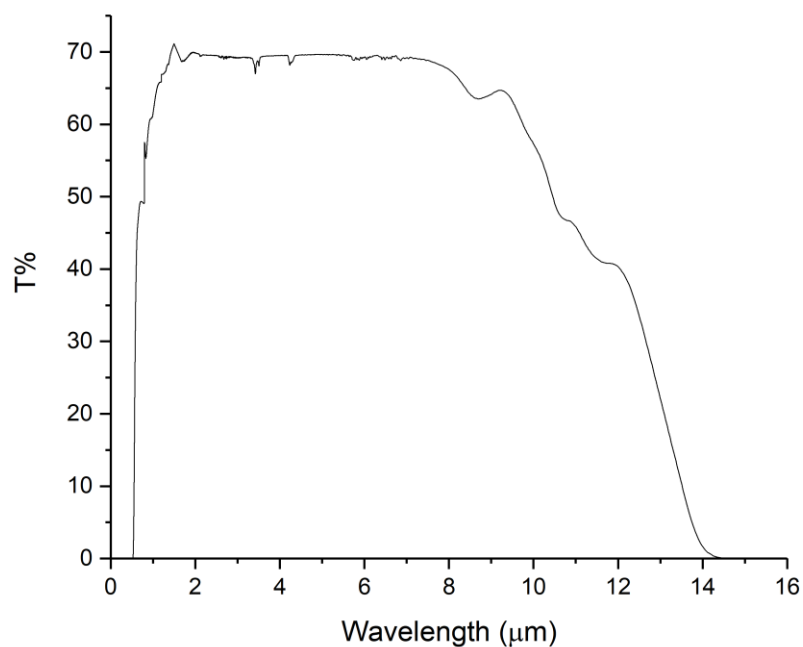
Figure 58: Transmission spectrum of the sample with composition 40 mol% Ga_2Se_3 – 30 mol%Ga_2S_3 – 30 mol% La_2S_3.
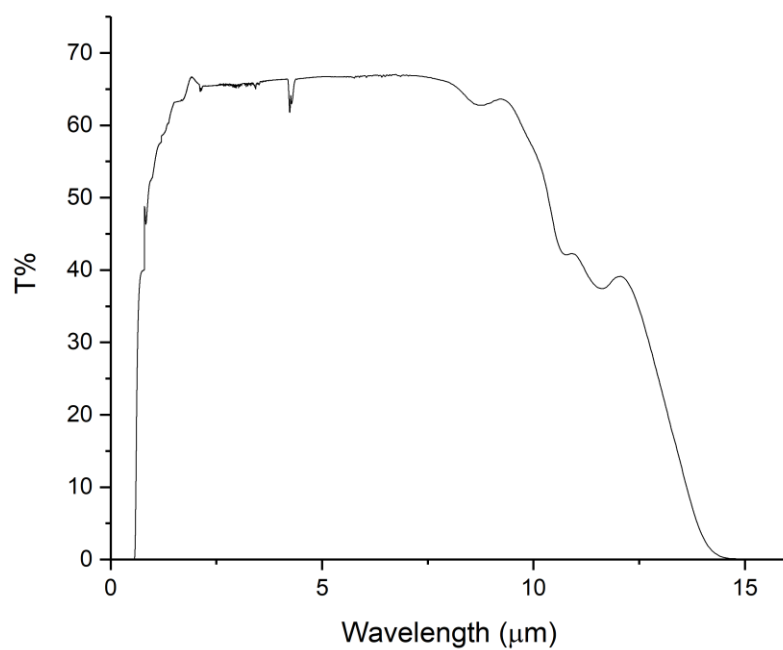
Figure 59: Transmission spectrum of the sample with composition 50 mol% Ga_2Se_3 –
20 mol%Ga_2S_3 – 30 mol% La_2S_3.
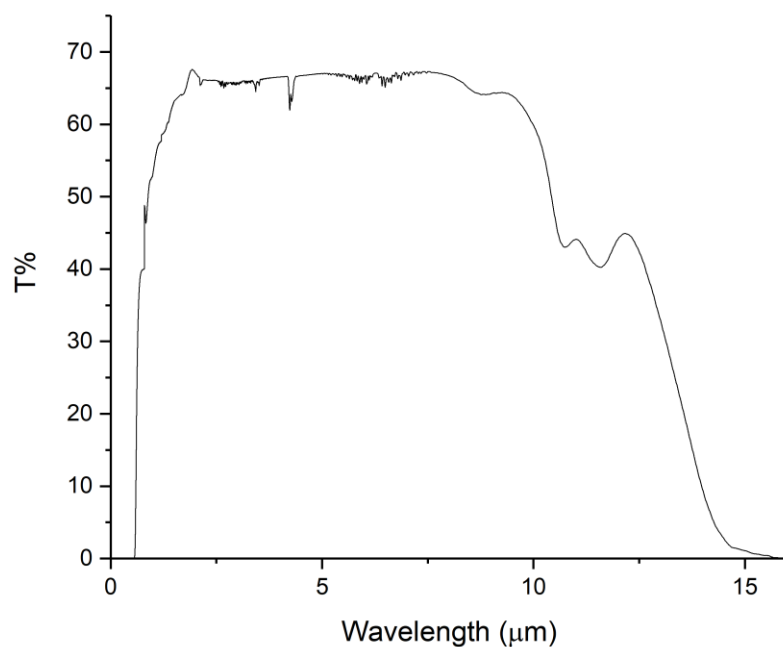
Figure 60: Transmission spectrum of the sample with composition 60 mol% Ga_2Se_3 –
20 mol%Ga_2S_3 – 30 mol% La_2S_3.
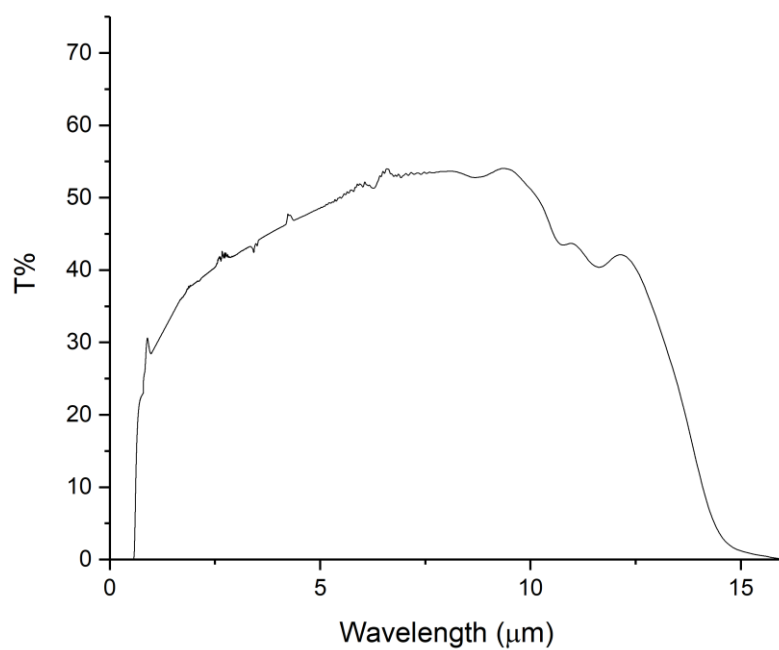
Figure 61: Transmission spectrum of the sample with composition 70 mol% Ga_2Se_3 – 0 mol%Ga_2S_3 – 30 mol% La_2S_3.
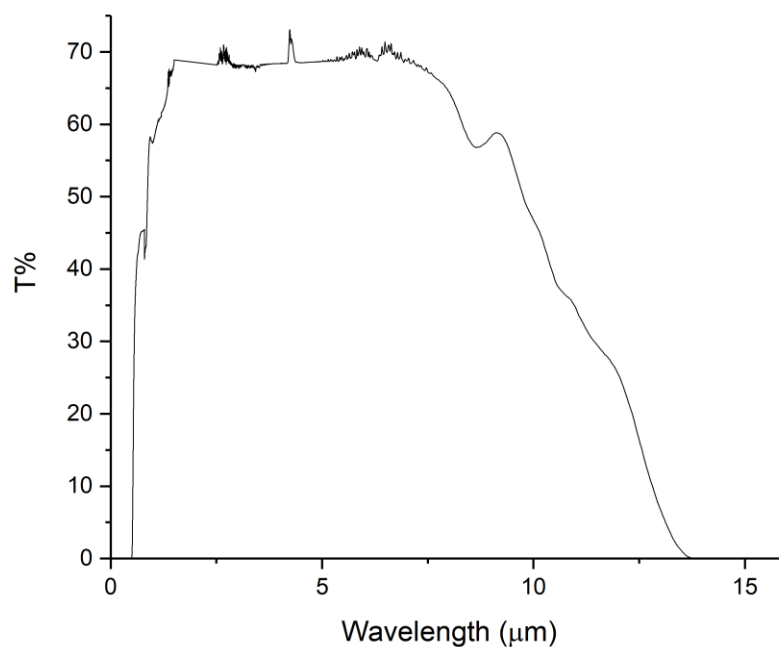
Figure 62: Transmission spectrum of the sample with composition 20 mol% Ga_2Se_3 – 40 mol%Ga_2S_3 – 40 mol% La_2S_3.
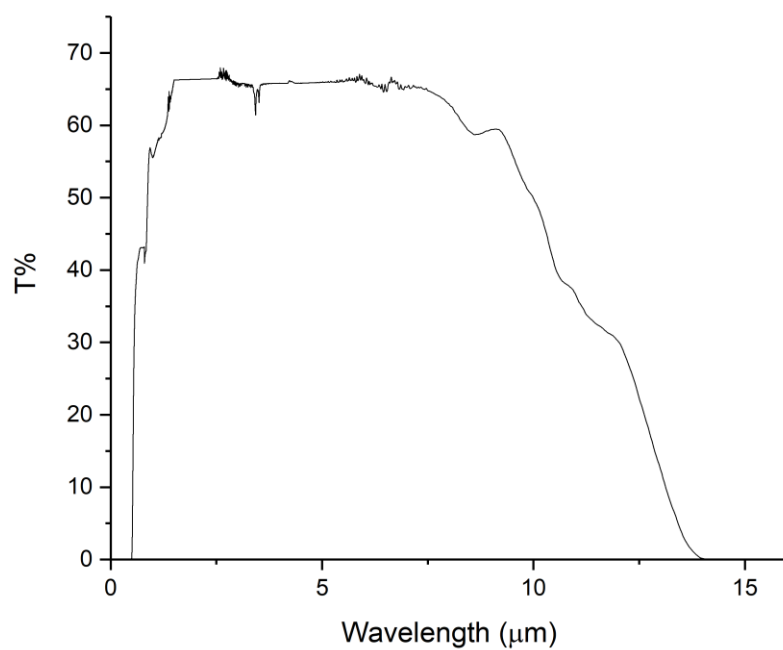
Figure 63: Transmission spectrum of the sample with composition 20 mol% Ga_2Se_3 – 45 mol%Ga_2S_3 – 35 mol% La_2S_3.
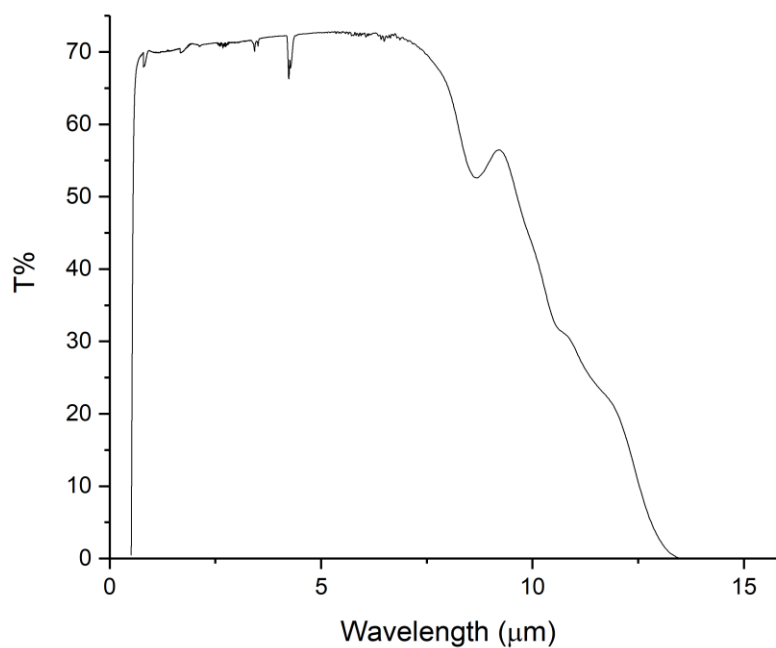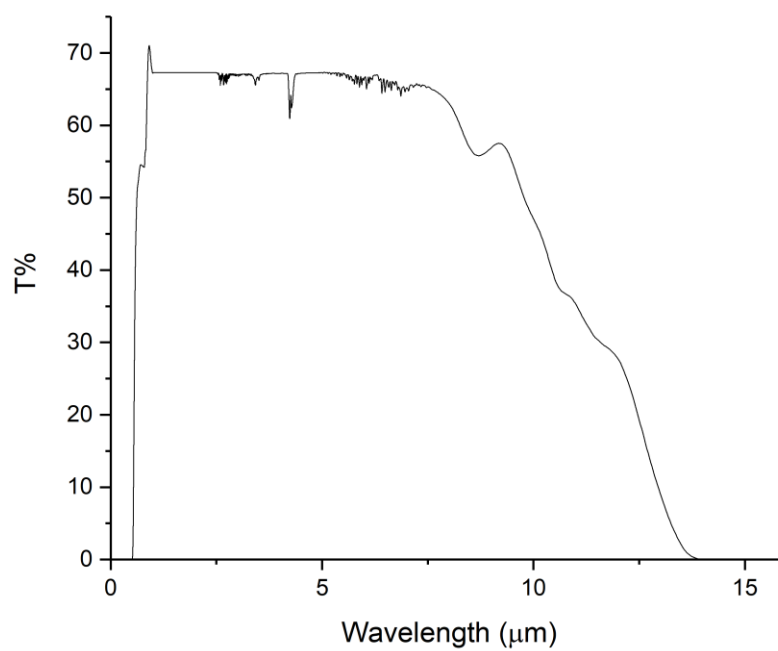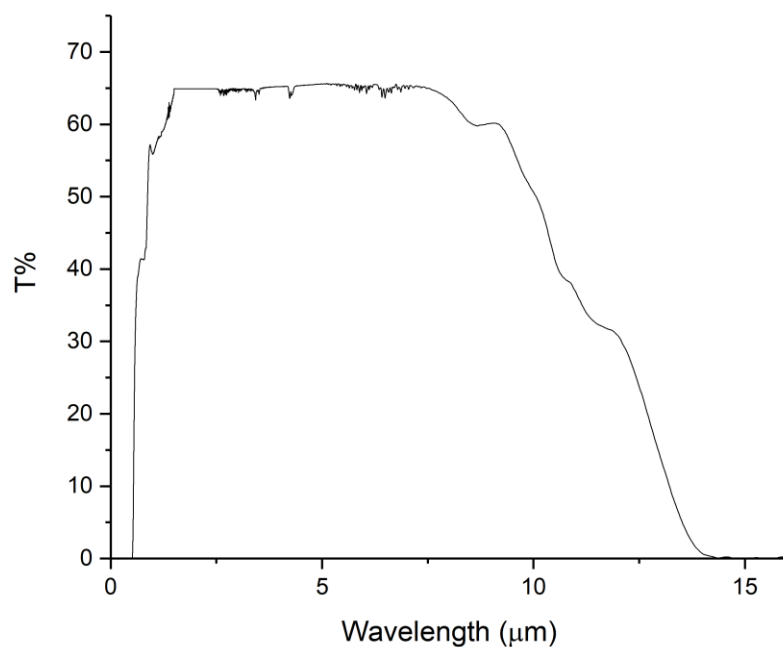

Figure 64: Transmission spectrum of the sample with composition 30 mol% Ga_2Se_3 – 30 mol%Ga_2S_3 – 40 mol% La_2S_3.

Appendix E   **Sellmeier coefficients**

Sample	A	B	C	A1	B1	C1
LD1746	1.8399	1.6430	1.0078	0.0249	0.0246	0.0289
LD1762	0.3065	2.1079	2.2505	0.1371	0.0428	0.0433
LD1748	0.0006	4.3842	0.4942	0.0292	0.0482	0.0920
LD1750	1.9852	0.8574	2.1145	0.0536	0.0765	0.0521
LD1752	4.3337	0.6872	0.0947	0.0417	0.0387	0.1628
LD1758	3.5719	0.6574	0.6564	0.0642	0.0241	0.0241

Appendix F **Least squares method with matrices**

In the JO analysis, the aim is to minimise $(S_m - S_{JO})^2$. We can define S_{JO} as:

$$S_{JO} = \Omega_i M + \varepsilon = S_m$$

$$\varepsilon = S_m - \Omega_i M$$

where Ω_i is the matrix with the JO parameters, M is the matrix containing the reduced matrix elements, S_m is the matrix of the measured line strength and ε is the matrix of the residuals for each transition. The minimisation of $(S_m - S_{JO})^2$ is thus correspondent to the minimisation of $\sigma(\Omega_i) = \varepsilon^2$. This results in:

$$\sigma(\Omega_i) = \varepsilon^2 = \varepsilon\varepsilon' = S_m{}'S_m - S_m{}'\Omega_i M - \Omega_i' M' S_m - \Omega_i{}'M'M\Omega_i$$

where the symbol ' indicates the transpose of the matrix. Then the first derivative can be equalised to 0 as:

$$\frac{\delta\sigma(\Omega_i)}{\delta\Omega_i} = 2M'S_m - 2M'M\Omega_i = 0$$

$$Note: S_m{}'\Omega_i M = \Omega_i'M'S_m \; as \; they \; are \; both \; 1x1 \; and \; thus \; symmetric.$$

We can then conclude that:

$$2M'M\Omega_i = 2M'S_m$$

$$\Omega_i = (M'M)^{-1}M'S_m$$

List of References

[1]   R. H. Brill, "Ancient Glass," *Sci. Am.*, vol. 209, no. 5, pp. 120–131, Nov. 1963.

[2]   E. D. Zanotto and J. C. Mauro, "The glassy state of matter: Its definition and ultimate fate," *J. Non. Cryst. Solids*, vol. 471, pp. 490–495, Sep. 2017.

[3]   ASTM Interational, "Standard Terminology of Glass and Glass Products," *ASTM Standards*. ASTM International, West Conshohocken, 2015.

[4]   J. Zarzycki, *Les Verres et l'état vitreux.*, Paris: Masson, 1982.

[5]   J. Wong and C. A. Angell, *Glasstruktur: Glass Structure by Spectroscopy.*, New York: Marcel Dekker Inc., 1976.

[6]   A. K. Varshneya and J. C. Mauro, "Comment on misconceived ASTM definition of 'Glass' by A. C. wright," *Glas. Technol. Eur. J. Glas. Sci. Technol. Part A*, vol. 51, no. 1, pp. 28–30, 2010.

[7]   I. Pethes *et al.*, "Short range order in Ge-Ga-Se glasses," *J. Alloys Compd.*, vol. 651, pp. 578–584, 2015.

[8]   Y. Yin, H. Sone, and S. Hosaka, "Simulation of Proposed Confined-Chalcogenide Phase-Change Random Access Memory for Low Reset Current by Finite Element Modelling," *Jpn. J. Appl. Phys.*, vol. 45, no. 8A, pp. 6177–6181, Aug. 2006.

[9]   D. Hohl and R. O. Jones, "First-principles molecular-dynamics simulation of liquid and amorphous selenium," *Phys. Rev. B*, vol. 43, no. 5, pp. 3856–3870, Feb. 1991.

[10]   S. Caravati, M. Bernasconi, T. D. Kühne, M. Krack, and M. Parrinello, "Coexistence of tetrahedral- and octahedral-like sites in amorphous phase change materials," *Appl. Phys. Lett.*, vol. 91, no. 17, p. 171906, Oct. 2007.

[11]   B. M. Scalet, M. Garcia Muñoz, Q. Sissa Aivi, S. Roudier, and D. S. Luis, *Best Available Techniques (BAT) Reference Document for the Manufacture of Glass.*, Seville: European Commission, 2013.

[12]   I. D. Aggarwal and J. S. Sanghera, "Development and applications of chalcogenide glass optical fibers at NRL," *J. Optoelectron. Adv. Mater.*, vol. 4, no. 3, pp. 665–678, 2002.

[13]   B. J. Eggleton, B. Luther-Davies, and R. Kathleen, "Chalcogenide photonics," *Nat. Photonics*, vol. 5, no. 12, pp. 725–725, 2011.

List of References

[14]   A. Zakery and S. R. Elliott, "Optical properties and applications of chalcogenide glasses: a review," *J. Non. Cryst. Solids*, vol. 330, no. 1–3, pp. 1–12, Nov. 2003.

[15]   A. B. Seddon, "Chalcogenide glasses: a review of their preparation, properties and applications," *J. Non. Cryst. Solids*, vol. 184, pp. 44–50, 1995.

[16]   Vitron, "Vitron IG6," 2015. [Online]. Available: http://www.vitron.de/datasheets/VITRON IG-6 Datenblatt Jan 2015.pdf.

[17]   Vitron, "Vitron IG5," 2015. [Online]. Available: http://www.vitron.de/datasheets/VITRON IG-5 Datenblatt Jan 2015.pdf.

[18]   Umicore, "GASIR-1." [Online]. Available: http://eom.umicore.com/storage/eom/gasir1-for-infrared-optics.pdf.

[19]   "AMTIR," 2017. [Online]. Available: http://www.amorphousmaterials.com/products/.

[20]   Vitron, "Vitron IG3," 2015. [Online]. Available: http://www.vitron.de/datasheets/VITRON IG-3 Datenblatt Jan 2015.pdf.

[21]   Vitron, "Vitron IG2," 2015. [Online]. Available: http://www.vitron.de/datasheets/VITRON IG-2 Datenblatt Jan 2015.pdf.

[22]   Vitron, "Vitron IG4," 2015. [Online]. Available: http://www.vitron.de/datasheets/VITRON IG-4 Datenblatt Jan 2015.pdf.

[23]   Umicore, "GASIR-5." [Online]. Available: http://eom.umicore.com/en/infrared-optics/blanks/GASIR5-for-infrared-optics.pdf.

[24]   D. W. Hewak *et al.*, "Chalcogenide glasses for photonics device applications," in *Photonic Glasses and Glass-Ceramics*, Kerala: Research Signpost, 2010, pp. 29–102.

[25]   D. Gibson, S. Bayya, J. Sanghera, V. Nguyen, M. Kotov, and G. Drake, "IR Gradient Index (GRIN) Materials For Broad-Band IR Optics," *Adv. Photonics*, pp. 9–10, 2015.

[26]   A. B. Seddon, Z. Tang, D. Furniss, S. Sujecki, and T. M. Benson, "Progress in rare-earth-doped mid-infrared fiber lasers," *Opt. Express*, vol. 18, no. 25, pp. 26704–26719, 2010.

[27]   J. S. McCloy, B. J. Riley, and D. A. Pierce, "Infrared-transparent glass ceramics: An exploratory study," *J. Non. Cryst. Solids*, vol. 410, pp. 160–173, 2015.

[28]   Y. Ledemi *et al.*, "Structural investigations of glass ceramics in the Ga_2S_3-GeS_2-CsCl system," *J. Phys. Chem. B*, vol. 113, no. 44, pp. 14574–14580, 2009.

[29]   A. M. Loireau-Lozac'h, M. Guittard, and J. Flahaut, "Verres formes par les sulfures L₂S₃ des terres rares avec le sulfure de gallium Ga₂S₃," *Mater. Res. Bull.*, vol. 11, no. 12, pp. 1489–1496, 1976.

[30]   T. Schweizer, B. N. Samson, R. C. Moore, D. W. Hewak, and D. N. Payne, "Rare-earth doped chalcogenide glass fibre laser," *Electron. Lett.*, vol. 33, no. 5, pp. 414–416, 1997.

[31]   T. Schweizer, D. W. Hewak, B. N. Samson, and D. N. Payne, "Spectroscopy of potential mid-infrared laser transitions in gallium lanthanum sulphide glass," *J. Lumin.*, vol. 72–74, no. 96, pp. 419–421, 1997.

[32]   T. Schweizer, "Rare-earth-doped gallium lanthanum sulphide glasses for mid-infrared fibre lasers," University of Southampton, 2000.

[33]   J. S. Sanghera and I. D. Aggarwal, *Infrared fibre optics*. Washington D.C.: CRC Press, 1998.

[34]   W. A. King, A. G. Clare, and W. C. LaCourse, "Laboratory preparation of highly pure As₂Se₃ glass," *J. Non. Cryst. Solids*, vol. 181, no. 3, pp. 231–237, Feb. 1995.

[35]   S. Danto *et al.*, "Correlation between native As₂Se₃ preform purity and glass optical fiber mechanical strength," *Mater. Res. Bull.*, vol. 49, no. 1, pp. 250–258, 2014.

[36]   C. T. Moynihan, P. B. Macedo, M. S. Maklad, R. K. Mohr, and R. E. Howard, "Intrinsic and impurity infrared absorption in As₂Se₃ glass," *J. Non-Cryst. Solids*, vol. 17, no. 3, pp. 369–385, May 1975.

[37]   A. R. Hilton, D. J. Hayes, and M. D. Rechtin, "Infrared absorption of some high-purity chalcogenide glasses," *J. Non. Cryst. Solids*, vol. 17, no. 3, pp. 319–338, May 1975.

[38]   T. Kanamori, Y. Terunuma, S. Takahashi, and T. Miyashita, "Transmission loss characteristics of As₄₀S₆₀ and As₃₈Ge₅Se₅₇ glass unclad fibers," *J. Non. Cryst. Solids*, vol. 69, no. 2–3, pp. 231–242, Jan. 1985.

[39]   S. Shibata, T. Manabe, and M. Horiguchi, "Preparation of Ge-S glass fibers with reduced OH, SH content," *Jpn. J. Appl. Phys.*, vol. 20, no. 1, pp. L13–L16, Jan. 1981.

[40]   H. Yuan, J. Zhang, R. Yu, and Q. Su, "Synthesis of rare earth sulfides and their UV-vis absorption spectra," *J. Rare Earths*, vol. 27, no. 2, pp. 308–311, 2009.

[41]   Y.-R. Luo, "Comprehensive handbook of chemical bond energies," *Journal of Physics and Chemistry of Solids*, vol. 58, no. 3. p. 1075, 2007.

[42]   R. Beerkens, "Fining of Glass Melts: What We Know about Fining Processes Today," in *69th*

Conference on Glass Problems: Ceramic Engineering and Science Proceedings, Volume 30, Issue 1, John Wiley & Sons, Inc., 2009, pp. 13–28.

[43] A. Brehault, L. Calvez, T. Pain, P. Adam, J. Rollin, and X. H. Zhang, "Multispectral glass transparent from visible to thermal infrared," *Proc. SPIE*, vol. 9070. p. 90702F – 90702F – 12, 2014.

[44] P. Lucas, G. J. Coleman, S. Jiang, T. Luo, and Z. Yang, "Chalcogenide glass fibers: Optical window tailoring and suitability for bio-chemical sensing," *Opt. Mater. (Amst).*, vol. 47, pp. 530–536, 2015.

[45] J. L. Adam, "Lanthanides in non-oxide glasses," *Chem. Rev.*, vol. 102, no. 6, pp. 2461–2476, 2002.

[46] L. J. Mattos and A. G. Clare, "The crystallisation and optical properties of gallium cerium lanthanum sulphide glass," *Phys. Chem. Glas.*, vol. 34, no. 6, pp. 244–250.

[47] M. F. Churbanov, "High-purity chalcogenide glasses as materials for fiber optics," *J. Non. Cryst. Solids*, vol. 184, no. 13, pp. 25–29, 1995.

[48] D. Pugliese *et al.*, "Concentration quenching in an Er-doped phosphate glass for compact optical lasers and amplifiers," *J. Alloys Compd.*, vol. 657, pp. 678–683, 2016.

[49] D. W. Hewak *et al.*, "Quantum-Efficiency of Praseodymium Doped Ga:La:S Glass for 1.3 μm Optical Fibre Amplifiers," vol. 6, no. 5, pp. 609–612, 1994.

[50] V. S. Shiryaev, J. L. Adam, X. H. Zhang, and M. F. Churbanov, "Study of characteristic temperatures and nonisothermal crystallization kinetics in As-Se-Te glass system," *Solid State Sci.*, vol. 7, no. 2, pp. 209–215, 2005.

[51] V. S. Shiryaev and M. F. Churbanov, "Preparation of high-purity chalcogenide glasses," in *Chalcogenide Glasses*, Oxford: Woodhead Publishing, 2014, pp. 3–35.

[52] H. H. Adler and P. F. Kerr, "Variations in infrared spectra, molecular symmetry and site symmetry of sulfate minerals," *Am. Mineral.*, vol. 50, pp. 132–147, 1965.

[53] M. F. Churbanov, I. V. Scripachev, G. E. Snopatin, V. S. Shiryaev, and V. G. Plotnichenko, "High-purity glasses based on arsenic chalcogenides," *J. Optoelectron. Adv. Mater.*, vol. 3, no. 2, pp. 341–349, 2001.

[54] J. Yang, Y. Zhao, and R. L. Frost, "Infrared and infrared emission spectroscopy of gallium oxide α-GaO(OH) nanostructures," *Spectrochim. Acta - Part A Mol. Biomol. Spectrosc.*, vol.

74, no. 2, pp. 398–403, 2009.

[55]   M. Salavati-Niasari, G. Hosseinzadeh, and F. Davar, "Synthesis of lanthanum hydroxide and lanthanum oxide nanoparticles by sonochemical method," *J. Alloys Compd.*, vol. 509, no. 10, pp. 4098–4103, 2011.

[56]   M. F. Churbanov, "High-purity chalcogenide glasses as materials for fiber optics," *J. Non. Cryst. Solids*, vol. 184, pp. 25–29, May 1995.

[57]   D. L. Perry, "Inorganic Compound Data," in *Handbook of Inorganic Compounds, Second Edition*, CRC Press, 2011, pp. 1–476.

[58]   M. M. A. Imran, D. Bhandari, and N. S. Saxena, "Enthalpy recovery during structural relaxation of $Se_{96}In_4$ chalcogenide glass," *Phys. B Condens. Matter*, vol. 293, no. 3–4, pp. 394–401, 2001.

[59]   P. Gabbot, *Principles and Applications of Thermal Analysis.*, Oxford: Wiley-Blackwell, 2008.

[60]   G. Riondino and G. Baricco, "Structural relaxation in metallic glasses," *Philos. Mag. Part B*, vol. 56, no. 2, pp. 177–183, 1987.

[61]   X. H. Zhang *et al.*, "Infrared transmitting glasses and glass-ceramics," *J. Non. Cryst. Solids*, vol. 352, no. 23–25, pp. 2411–2415, 2006.

[62]   N. Mehta, "Applications of chalcogenide glasses in electronics and optoelectronics: A review," *J. Sci. Ind. Res. (India).*, vol. 65, no. 10, pp. 777–786, 2006.

[63]   J. H. Kim, J. S. Park, E. S. Park, W. T. Kim, and D. H. Kim, "Estimation of critical cooling rates for glass formation in bulk metallic glasses through non-isothermal thermal analysis," *Met. Mater. Int.*, vol. 11, no. 1, pp. 1–9, 2005.

[64]   M. D. Mikhailov and A. S. Tver'yanovich, "Critical Cooling Rates of Chalcogenide Glass-forming Melts," *Fiz. Khim. Stekla*, vol. 12, no. 3, pp. 274–284, 1986.

[65]   A. M. Loireau-Lozac'h and M. Guittard, "System ternaire La_2Se_3-Ga_2Se_3-$GeSe_2$. Phase diagram-glass study.," *Mater. Res. Bull.*, vol. 12, p. 877, 1977.

[66]   J. D. Shephard *et al.*, "The effect of GaSe on Ga-La-S glasses," *J. Non. Cryst. Solids*, vol. 326–327, pp. 439–445, 2003.

[67]   P. Bastock, C. Craig, K. Khan, E. Weatherby, J. Yao, and D. W. Hewak, "Properties of Gallium Lanthanum Sulphide Glass," in *CLEO: 2015*, 2015, p. STh1G.1.

List of References

[68] P. Larkin, "Ir and Raman Spectroscopy - Principles and Spectral Interpretation," in *Infrared and Raman Spectroscopy*, London: Elsevier, 2011, pp. 1–5.

[69] C. Julien *et al.*, "Raman and infrared spectroscopic studies of GeGaAg sulphide glasses," *Mater. Sci. Eng. B*, vol. 22, no. 2–3, pp. 191–200, 1994.

[70] M. Dunleavy, G. C. Allen, and M. Paul, "Characterization of lanthanum sulphides," *Adv. Mater.*, vol. 4, no. 6, pp. 424–427, Jun. 1992.

[71] A. Kuhn, R. Chevalier, and A. Rimsky, "Atomic structure of a 4 H GaSe polytype named δ-type," *Acta Crystallogr. Sect. B Struct. Crystallogr. Cryst. Chem.*, vol. 31, no. 12, pp. 2841–2842, Dec. 1975.

[72] J. Saiter, J. Ledru, G. Saffarini, and S. Benazeth, "About the coordination number of indium in $Ge_xSe_{1-x-y}In_y$ glasses," *Mater. Lett.*, vol. 28, no. 4–6, pp. 451–455, 1996.

[73] A. M. Abd Elnaeim, K. A. Aly, N. Afify, and A. M. Abousehlly, "Glass transition and crystallization kinetics of $In_x(Se_{0.75}Te_{0.25})_{100-x}$ chalcogenide glasses," *J. Alloys Compd.*, vol. 491, no. 1–2, pp. 85–91, 2010.

[74] J. Wang *et al.*, "Halide-modified Ga–La sulfide glasses with improved fiber-drawing and optical properties for Pr^{3+}-doped fiber amplifiers at 1.3 μm," *Appl. Phys. Lett.*, vol. 71, no. 13, p. 1753, 1997.

[75] Y. Ledemi, M. El-Amraoui, L. Calvez, X.-H. Zhang, B. Bureau, and Y. Messaddeq, "Colorless chalco-halide Ga_2S_3-GeS_2-CsCl glasses as new optical material," *Photonic Fiber Cryst. Devices Adv. Mater. Innov. device Appl. VII*, vol. 8847, p. 884704, 2013.

[76] J. D. Shephard, R. I. Kangley, R. J. Hand, D. Furniss, C. A. Miller, and A. B. Seddon, "Properties of Ga-La-Na sulphide glasses," *J. Non. Cryst. Solids*, vol. 332, no. 1–3, pp. 271–278, 2003.

[77] A. K. Vijh, "Chemical Approaches to the Approximate Prediction of Band Gaps of Binary Semiconductors and Insulators," *J. Electrochem. Soc.*, vol. 117, no. 5, p. 173C–178C, 1970.

[78] F. Di Quarto, C. Sunseri, S. Piazza, and M. C. Romano, "Semiempirical Correlation between Optical Band Gap Values of Oxides and the Difference of Electronegativity of the Elements. Its Importance for a Quantitative Use of Photocurrent Spectroscopy in Corrosion Studies," *J. Phys. Chem. B*, vol. 101, no. 14, pp. 2519–2525, 1997.

[79]   H. Yayama, S. Fujino, K. Morinaga, H. Takebe, D. W. Hewak, and D. N. Payne, "Refractive index dispersion of gallium lanthanum sulfide and oxysulfide glasses," *J. Non. Cryst. Solids*, vol. 239, no. 1–3, pp. 187–191, 1998.

[80]   D. W. Hewak and M. Mairaj, "Gallium lanthanum sulfide glasses and optical waveguides and devices using such glasses," Patent No. US20030118315 A1, 2003.

[81]   Y. D. West, T. Schweizer, D. J. Badry, and D. W. Hewak, "Gallium Lanthanum Sulphide Fibers for Infrared Transmission," *Fiber Integr. Opt.*, vol. 19, no. 3, pp. 229–250, Jul. 2000.

[82]   A. C. Lasaga and R. T. Cygan, "Electronic and ionic polarizabilities of silicate minerals.," *American Mineralogist*, vol. 67, no. 3–4. pp. 328–334, 1982.

[83]   O. M. Nefedov and M. P. Egorov, "Modern trends in physical organic chemistry," *Pure Appl. Chem.*, vol. 69, no. 2, pp. 259–262, Feb. 1997.

[84]   M. Poulain, "Fluoride glasses: Properties, technology and applications," in *Photonic Glasses and Glass-Ceramics*, S. M. Ganapathy, Ed. Kerala, India: Research Signpost, 2010, pp. 1–28.

[85]   J. L. Adam and X. Zhang, *Chalcogenide Glasses*. Cambridge: Woodhead Publishing, 2013.

[86]   V. S. Shiryaev and M. F. Churbanov, "Recent advances in preparation of high-purity chalcogenide glasses for mid-IR photonics," *J. Non. Cryst. Solids*, vol. 475, pp. 1–9, Nov. 2017.

[87]   D. J. Brady, "Gallium lanthanum sulphide based glasses for mid-infrared optical fibres," University of Southampton, 1999.

[88]   A. Mairaj, "Optical waveguides and lasers in improved gallium lanthanum sulphide glass," University of Southampton, 2003.

[89]   L. Calvez *et al.*, "Similar behaviors of sulfide and selenide-based chalcogenide glasses to form glass-ceramics," *Proc. SPIE*, vol. 7598, pp. 759802-1-759802–16, 2010.

[90]   D. J. Brady, T. Schweizer, J. Wang, and D. W. Hewak, "Minimum loss predictions and measurements in gallium lanthanum sulphide based glasses and fibre," *J. Non. Cryst. Solids*, vol. 242, no. 2–3, pp. 92–98, 1998.

[91]   J. D. Dow and D. Redfield, "Toward a unified theory of Urbach's rule and exponential absorption edges," *Phys. Rev. B*, vol. 5, no. 2, pp. 594–610, 1972.

[92]   D. L. Wood and J. Tauc, "Weak absorption tails in amorphous semiconductors," *Phys. Rev. B*, vol. 5, no. 8, pp. 3144–3151, 1972.

List of References

[93] S. H. Simon, *The Oxford Solid State Basics*. Oxford, 2013.

[94] C. B. Layne, W. H. Lowdermilk, and M. J. Weber, "Multiphonon relaxation of rare-earth ions in oxide glasses," *Phys. Rev. B*, vol. 16, no. 1, pp. 10–20, 1977.

[95] C. C. Ye, D. W. Hewak, M. Hempstead, B. N. Samson, and D. N. Payne, "Spectral properties of Er^{3+}-doped gallium lanthanum sulphide glass," *J. Non. Cryst. Solids*, vol. 208, no. 1–2, pp. 56–63, 1996.

[96] F. Auzel, "Upconversion and Anti-Stokes Processes with f and d Ions in Solids," *Chem. Rev.*, vol. 104, no. 1, pp. 139–173, 2004.

[97] M. Lancry, B. Poumellec, and C. Gonnet, "Low loss multimode optical fibers via fictive temperature reduction by means of outer-cladding na doping," *J. Light. Technol.*, vol. 34, no. 4, pp. 1238–1241, 2016.

[98] D. A. Pinnow, T. C. Rich, F. W. Ostermayer, and M. Didomenico, "Fundamental optical attenuation limits in the liquid and glassy state with application to fiber optical waveguide materials," *Appl. Phys. Lett.*, vol. 22, no. 10, pp. 527–529, 1973.

[99] M. E. Lines, "Scattering losses in optic fiber materials. I. A new parametrization," *J. Appl. Phys.*, vol. 55, no. 11, pp. 4052–4057, 1984.

[100] M. J. F. Digonnet, *Rare-earth-doped fiber lasers and amplifiers, revised and expanded*. New York: CRC press, 2001.

[101] B. R. Judd, "Hypersensitive Transitions in Rare-Earth Ions," *J. Chem. Phys.*, vol. 44, no. 2, p. 839, 1966.

[102] P. Bastock, "Manufacturing novel fibre," University of Southampton, 2015.

[103] K. Nakamoto, "Infrared and Raman Spectra of Inorganic and Coordination Compounds: Part A: Theory and Applications in Inorganic Chemistry," in *Wiley, Hoboken, New Jersey*, 2009, pp. 1–432.

[104] J. S. Sanghera, L. E. Busse, and I. D. Aggarwal, "Effect of scattering centers on the optical loss of As_2S_3glass fibers in the infrared," *J. Appl. Phys.*, vol. 75, no. 10, pp. 4885–4891, 1994.

[105] V. Gomes, C. D. G. De Borba, and H. G. Riella, "Production and characterization of glass ceramics from steelwork slag," *J. Mater. Sci.*, vol. 37, no. 12, pp. 2581–2585, 2002.

[106]   S. Y. El-Zaiat, "Determination of the complex refractive index of a thick slab material from its spectral reflectance and transmittance at normal incidence," *Opt. - Int. J. Light Electron Opt.*, vol. 124, no. 2, pp. 157–161, Jan. 2013.

[107]   K. Hinrichs, K. J. Eichhorn, G. Ertl, D. L. Mills, and H. Lüth, "Ellipsometry of Functional Organic Surfaces and Films," *Springer Ser. Surf. Sci.*, vol. 52, 2014.

[108]   W. Sellmeier, "Zur Erklärung der abnormen Farbenfolge im Spectrum einiger Substanzen," *Ann. Phys.*, vol. 219, no. 6, pp. 272–282, 1871.

[109]   G. Demetriou, D. W. Hewak, A. Ravagli, C. Craig, and A. Kar, "Nonlinear refractive index of ultrafast laser inscribed waveguides in gallium lanthanum sulphide," *Appl. Opt.*, vol. 56, no. 19, p. 5407, Jul. 2017.

[110]   M. Sheik-Bahae, A. A. Said, T. H. Wei, D. J. Hagan, and E. W. Van Stryland, "Sensitive Measurement of Optical Nonlinearities Using a Single Beam," *IEEE J. Quantum Electron.*, vol. 26, no. 4, pp. 760–769, 1990.

[111]   M. Sheik-Bahae A. A. Said, T. Wei, D. J. Hagan, E. W. Van Stryland, "Sensitive Measurement of Optical Nonlinearities Using a Single Beam," *IEEE J. Quantum Electron.*, vol. 26, no. QE-26, pp. 760–769, 1990.

[112]   M. Naftaly and R. Dudley, "Linearity calibration of amplitude and power measurements in terahertz systems and detectors," *Opt. Lett.*, vol. 34, no. 5, p. 674, 2009.

[113]   M. F. Churbanov and V. G. Plotnichenko, "Optical fibers from high-purity arsenic chalcogenide glasses," in *Semiconductors and Semimetals*, vol. 80, 2004, pp. 209–230.

[114]   J. Komma, C. Schwarz, G. Hofmann, D. Heinert, and R. Nawrodt, "Thermo-optic coefficient of silicon at 1550 nm and cryogenic temperatures," *Appl. Phys. Lett.*, vol. 101, no. 4, pp. 4–8, 2012.

[115]   J. Requejo-Isidro, A. K. Mairaj, V. Pruneri, D. W. Hewak, M. C. Netti, and J. J. Baumberg, "Self refractive non-linearities in chalcogenide based glasses," *J. Non. Cryst. Solids*, vol. 317, no. 3, pp. 241–246, 2002.

[116]   F. Smektala, C. Quemard, V. Couderc, and A. Barthélémy, "Non-linear optical properties of chalcogenide glasses measured by Z-scan," *J. Non. Cryst. Solids*, vol. 274, no. 1, pp. 232–237, 2000.

[117]   J. A. Duffy, *Bonding, energy level and bands in inorganic solids.*, New York [NY]: Longman Scientific & technicals, 1990.

List of References

[118] C. Z. Tan and J. Arndt, "The mean polarizability and density of glasses," *Phys. B Condens. Matter*, vol. 229, no. 3–4, pp. 217–224, 1997.

[119] U. Strom and P. C. Taylor, "Temperature and frequency dependences of the far-infrared and microwave optical absorption in amorphous materials," *Phys. Rev. B*, vol. 16, no. 12, pp. 5512–5522, 1977.

[120] R. Li and A. B. Seddon, "Gallium-lanthanum-sulphide glasses: a review of recent crystallisation studies," *J. Non. Cryst. Solids*, vol. 257, pp. 17–24, 1999.

[121] S. N. Taraskin, S. I. Simdyankin, S. R. Elliott, J. R. Neilson, and T. Lo, "Universal features of terahertz absorption in disordered materials," *Phys. Rev. Lett.*, vol. 97, no. 5, 2006.

[122] E. A. Reinsch and W. Meyer, "Finite perturbation calculation for the static dipole polarizabilities of the atoms Na through Ca," *Phys. Rev. A*, vol. 14, no. 3, pp. 915–918, 1976.

[123] M. Naftaly and R. E. Miles, "Terahertz time-domain spectroscopy of silicate glasses and the relationship to material properties," *J. Appl. Phys.*, vol. 102, no. 4, 2007.

[124] S. Onari, K. Matsuishi, and T. Arai, "Far-infrared absorption spectra and the spatial fluctuation of charges on amorphous AsS and AsSe systems," *J. Non. Cryst. Solids*, vol. 86, no. 1–2, pp. 22–32, 1986.

[125] S. B. Kang *et al.*, "Optical and dielectric properties of chalcogenide glasses at terahertz frequencies," *ETRI J.*, vol. 31, no. 6, pp. 667–674, 2009.

[126] E. P. J. Parrott *et al.*, "Atomic charge distribution in sodosilicate glasses from terahertz time-domain spectroscopy," *Phys. Rev. B - Condens. Matter Mater. Phys.*, vol. 82, no. 14, 2010.

[127] A. Bréhault *et al.*, "Evaluation of chalcogenide glasses for multispectral imaging in the visible, SWIR and LWIR spectral regions," *Proc. SPIE*, vol. 9822, p. 982202, 2016.

[128] J. McCarthy, H. Bookey, S. Beecher, R. Lamb, I. Elder, and A. K. Kar, "Spectrally tailored mid-infrared super-continuum generation in a buried waveguide spanning 1750 nm to 5000 nm for atmospheric transmission," *Appl. Phys. Lett.*, vol. 103, no. 15, 2013.

[129] G. G. Gadzhiev, S. M. Ismailov, M. M. Khamidov, K. K. Abdullaev, and V. V. Sokolov, "Thermophysical properties of sulfides of lanthanum, praseodymium, gadolinium, and dysprosium," *High Temp.*, vol. 38, no. 6, pp. 875–879, 2000.

[130]   S. Stecura and W. J. Campbell, "Thermal expansion and phase inversion of rare-earth oxides," *US Bur. Mines Rep. Number 5847*, 1961.

[131]   A. F. Kozmidis-Petrović, "Theoretical analysis of relative changes of the Hruby, Weinberg, and Lu–Liu glass stability parameters with application on some oxide and chalcogenide glasses," *Thermochim. Acta*, vol. 499, no. 1–2, pp. 54–60, Feb. 2010.

[132]   British Standard Institution, "Differential scanning calorimetry (DSC) Part 2 : Determination of glass transition temperature and glass transition step height." Standards Publication Plastics, 2014.

[133]   A. Tarasov and L. Fröberg, "Thermal Analysis: methods, principles, application," *Lect. Ser. Heterog. Catal.*, p. 36, 2014.

[134]   R. Rawlings, J. Wu, and a Boccaccini, "Glass-ceramics: Their production from wastes - A Review," *J. Mater. Sci.*, vol. 41, no. 3, pp. 733–761, 2006.

[135]   I. Avramov, E. D. Zanotto, and M. O. Prado, "Glass-forming ability versus stability of silicate glasses. II. Theoretical demonstration," *J. Non. Cryst. Solids*, vol. 320, no. 1–3, pp. 9–20, Jun. 2003.

[136]   A. Hrubý, "Evaluation of glass-forming tendency by means of DTA," *Czechoslov. J. Phys.*, vol. 22, no. 11, pp. 1187–1193, 1972.

[137]   M. C. Weinberg, "Assessment of glass stability criteria," *Phys. Chem. Glas.*, vol. 35, no. 3, pp. 119–123, 1994.

[138]   Z. P. Lu and C. T. Liu, "A new glass-forming ability criterion for bulk metallic glasses," *Acta Mater.*, vol. 50, no. 13, pp. 3501–3512, 2002.

[139]   V. Vassilev, I. Karadashka, and S. Parvanov, "New chalcogenide glasses in the Ag_2Te-As_2Se_3-CdTe system," *J. Phys. Chem. Solids*, vol. 69, no. 7, pp. 1835–1840, 2008.

[140]   T. Kambe, *Elementary fluid dynamics*, First Ed. London: World Scientific Publishing, 2007.

[141]   I. Avramov, "Viscosity activation energy," *Phys. Chem. Glas. Eur. J. Glas. Sci. Technol. Part B*, vol. 48, no. 1, pp. 61–63, 2007.

[142]   L. S. Garca-Coln, L. F. Del Castillo, and P. Goldstein, "Theoretical basis for the Vogel-Fulcher-Tammann equation," *Phys. Rev. B*, vol. 40, no. 10, pp. 7040–7044, 1989.

[143]   International Organization for Standardization, "ISO 11359-2:1999 Plastics -- Thermomechanical analysis (TMA) -- Part 2: Determination of coefficient of linear thermal

expansion and glass transition temperature." p. 10, 1999.

[144]   British Standard Institution, "Differential scanning calorimetry (DSC) Part 4 : Determination of specific heat capacity." Standards Publication Plastics, 2014.

[145]   M. W. Chase Jr., "NIST-JANAF Themochemical Tables, Fourth Edition," 1998.

[146]   "Viscosity and viscometric fixed points of glass," *British Standard Institution*, vol. BS 7034-2:, no. August. 1993.

[147]   C. Vitale-Brovarone, G. Novajra, J. Lousteau, D. Milanese, S. Raimondo, and M. Fornaro, "Phosphate glass fibres and their role in neuronal polarization and axonal growth direction," *Acta Biomater.*, vol. 8, no. 3, pp. 1125–1136, 2012.

[148]   ASTM Int., "ASTM E384: Standard Test Method for Knoop and Vickers Hardness of Materials," *ASTM Stand.*, pp. 1–43, 2012.

[149]   E. P. Fel and L. I. Stefanovich, "Kinetics of the spinodal decomposition of glasses," *Sov. Phys. JEPT*, vol. 1704, no. November 1990, pp. 951–956, 1991.

[150]   Amorphous Materials Inc., "Comparison of IR Materials." [Online]. Available: http://www.amorphousmaterials.com/products/.

[151]   V. S. Shiryaev, J.-L. Adam, X. H. Zhang, and M. F. Churbanov, "Study of characteristic temperatures and nonisothermal crystallization kinetics in AsSeTe glass system," *Solid State Sci.*, vol. 7, no. 2, pp. 209–215, Feb. 2005.

[152]   H. Suzuki and R. Mori, "Phase Study on Binary System Ga-Se," *Japan J. Appl. Phys.*, vol. 13, no. 3, pp. 417–423, 1974.

[153]   R. M. A. Lieth, H. J. M. Heijligers, and C. W. M. Heijden, "The P-T-X Phase Diagram of the System Ga-S," *J. Electrochem. Soc.*, no. August 1966, pp. 798–801, 1967.

[154]   E. V Karaksina, V. S. Shiryaev, M. F. Churbanov, E. A. Anashkina, T. V Kotereva, and G. E. Snopatin, "Core-clad Pr^{3+}-doped Ga(In)-Ge-As-Se-(I) glass fibers: Preparation, investigation, simulation of laser characteristics," *Opt. Mater. (Amst).*, vol. 72, pp. 654–660, 2017.

[155]   R. J. Mears, L. Reekie, I. M. Jauncey, and D. N. Payne, "Low-noise erbium-doped fibre amplifier operating at 1.54μm," *Electron. Lett.*, vol. 23, no. 19, p. 1026, 1987.

[156]   K. Gerd, *Optical Fiber Communication*. New York [NY]: McGraw-Hill, 1991.

[157]   L. Shaw, B. Harbison, B. Cole, J. Sanghera, and I. Aggarwal, "Spectroscopy of the IR

transitions in Pr^{3+} doped heavy metal selenide glasses.," *Opt. Express*, vol. 1, no. 4, pp. 87–96, 1997.

[158]   F. Xia, X. Zhang, J. Ren, G. Chen, H. Ma, and J. L. Adam, "Glass Formation and Crystallization Behavior of a Novel GeS_2–Sb_2S_3–PbS Chalcogenide Glass System.," *J. Am. Ceram. Soc.*, vol. 89, no. 7, pp. 2154–2157, 2006.

[159]   A. N. Romanov *et al.*, "Near-IR luminescence from subvalent bismuth species in fluoride glass," *Opt. Mater. (Amst).*, vol. 34, no. 1, pp. 155–158, 2011.

[160]   W. B. White and D. G. Minser, "Raman spectra and structure of natural glasses," *J. Non. Cryst. Solids*, vol. 67, no. 1, pp. 45–59, 1984.

[161]   L. Bodiou *et al.*, "Mid-infrared guided photoluminescence from integrated Pr^{3+}-doped selenide ridge waveguides," *Opt. Mater. (Amst).*, vol. 75, pp. 109–115, 2018.

[162]   F. Charpentier *et al.*, "Mid-IR luminescence of Dy^{3+} and Pr^{3+} doped $Ga_5Ge_{20}Sb_{10}S(Se)_{65}$ bulk glasses and fibers," *Mater. Lett.*, vol. 101, pp. 21–24, 2013.

[163]   L. Li, J. Bian, Q. Jiao, Z. Liu, S. Dai, and C. Lin, "GeS_2–In_2S_3–CsI Chalcogenide Glasses Doped with Rare Earth Ions for Near- and Mid-IR Luminescence," *Sci. Rep.*, vol. 6, no. November, p. 37577, 2016.

[164]   T. Schweizer, B. N. Samson, J. R. Hector, W. S. Brocklesby, D. W. Hewak, and D. N. Payne, "Infrared emission from holmium doped gallium lanthanum sulphide glass," *Infrared Phys. Technol.*, vol. 40, no. 4, pp. 329–335, 1999.

[165]   V. Moizan *et al.*, "Er^{3+}-doped GeGaSbS glasses for mid-IR fibre laser application: Synthesis and rare earth spectroscopy," *Opt. Mater. (Amst).*, vol. 31, no. 1, pp. 39–46, 2008.

[166]   W. Koechner, *Solid-State Laser Engineering - 6th Edition*., New York: Springer, 2014.

[167]   G. R. Choppin, "Covalency in f-element bonds," *J. Alloys Compd.*, vol. 344, no. 1, pp. 55–59, 2002.

[168]   M. N. Brekhovskikh *et al.*, "Optical properties of europium-activated hafnium fluoride-based glasses," *Inorg. Mater.*, vol. 52, no. 10, pp. 1031–1034, Oct. 2016.

[169]   S. Cotton, *Lanthanide and Actinide Chemistry*. Chichester, UK: John Wiley & Sons Ltd, 2006.

[170]   A. De Bettencourt-Dias, *Luminescence of Lanthanide Ions in Coordination Compounds and Nanomaterials*. Chichester, United Kingdom: John Wiley & Sons Ltd, 2014.

List of References

[171] L. Petit, A. Borel, C. Daul, P. Maldivi, and C. Adamo, "A Theoretical Characterization of Covalency in Rare Earth Complexes through Their Absorption Electronic Properties: f–f Transitions," *Inorg. Chem.*, vol. 45, no. 18, pp. 7382–7388, Sep. 2006.

[172] J.-C. G. Bunzli and S. V Eliseeva, "Intriguing aspects of lanthanide luminescence," *Chem. Sci.*, vol. 4, no. 5, pp. 1939–1949, 2013.

[173] N. Kaltsoyannis and P. Scott, *The f Elements*. Oxford: Oxford University Press, 1999.

[174] C. Görller-Walrand and K. Binnemans, "Chapter 167 Spectral intensities of f-f transitions," vol. 25, Elsevier, 1998, pp. 101–264.

[175] G. V. Prakash, "Absorption spectral studies of rare earth ions," *Mater. Lett.*, no. October, 2000.

[176] D. G. Karraker, "Hypersensitive Transitions of Six-, Seven-, and Eight-Coordinate Neodymium, Holmium, and Erbium Chelates," *Inorg. Chem.*, vol. 6, no. 10, pp. 1863–1868, 1967.

[177] B. C. Jamalaiah *et al.*, "Optical absorption, fluorescence and decay properties of Pr^{3+}-doped PbO-H_3BO_3-TiO_2-AlF_3 glasses," *J. Lumin.*, vol. 129, no. 9, pp. 1023–1028, 2009.

[178] S. Tanabe, "Rare-earth-doped glasses for fiber amplifiers in broadband telecommunication," *Comptes Rendus Chim.*, vol. 5, no. 12, pp. 815–824, 2002.

[179] S. Tanabe, "Optical transitions of rare earth ions for amplifiers: How the local structure works in glass," *J. Non. Cryst. Solids*, vol. 259, no. 1–3, pp. 1–9, 1999.

[180] W. J. Miniscalco, "Erbium-Doped Glasses for Fiber Amplifiers at 1500 nm," *IEEE J. Light. Technol.*, vol. 9, no. 2, pp. 234–250, 1991.

[181] F. Auzel, G. Baldacchini, L. Laversenne, and G. Boulon, "Radiation trapping and self-quenching analysis in Yb^{3+}, Er^{3+}, and Ho^{3+} doped Y_2O_3," *Opt. Mater. (Amst).*, vol. 24, no. 1–2, pp. 103–109, 2003.

[182] F. Auzel, F. Bonfigli, S. Gagliari, and G. Baldacchini, "The interplay of self-trapping and self-quenching for resonant transitions in solids; Role of a cavity," *J. Lumin.*, vol. 94–95, pp. 293–297, 2001.

[183] J. F. Suyver, J. Grimm, M. K. Van Veen, D. Biner, K. W. Krämer, and H. U. Güdel, "Upconversion spectroscopy and properties of $NaYF_4$ doped with Er^{3+}, Tm^{3+} and/or Yb^{3+}," *J. Lumin.*, vol. 117, no. 1, pp. 1–12, 2006.

[184] B. R. Judd, "Optical Absorption Intensities of Rare-Earth Ions," *Phys. Rev.*, vol. 127, no. 3, pp. 750–761, Aug. 1962.

[185] G. S. Ofelt, "Intensities of Crystal Spectra of Rare-Earth Ions," *J. Chem. Phys.*, 1962.

[186] B. M. Walsh, "Judd-Ofelt theory: principles and practices," in *Advances in Spectroscopy for Lasers and Sensing*, Dordrecht: Springer, 2006, pp. 403–433.

[187] W. T. Carnall, H. Crosswhite, and H. M. Crosswhite, "Energy level structure and transition probabilities in the spectra of the trivalent lanthanides in LaF_3," Argonne, IL (United States), Jan. 1978.

[188] A. Ravagli, "Judd-Ofelt Analysis." Zenodo, 2018.

[189] M. Seshadri, K. V. Rao, J. L. Rao, and Y. C. Ratnakaram, "Spectroscopic and laser properties of Sm^{3+} doped different phosphate glasses," *J. Alloys Compd.*, vol. 476, no. 1–2, pp. 263–270, 2009.

[190] M. B. Saleh, M. H. Aly, and N. Azzam, "Temperature dependence for cross-relaxation rate of thulium doped fiber amplifiers in different glass hosts," in *Proceedings of the Twenty-Second National Radio Science Conference, 2005. NRSC 2005.*, 2005, pp. 551–558.

[191] K. Koughia, M. Munzar, T. Aoki, and S. O. Kasap, "Photoluminescence spectra and lifetimes of $^4I_{13/2} \rightarrow {}^4I_{15/2}$ and $^4I_{11/2} \rightarrow {}^4I_{15/2}$ transitions in erbium doped GeGaSe and GeGaS glasses," *J. Mater. Sci. Mater. Electron.*, vol. 18, pp. 153–157, 2007.

[192] C. Koughia, C. Craig, D. W. Hewak, and S. Kasap, "Tailoring the $^4I_{9/2} \rightarrow {}^4I_{13/2}$ emission in Er^{3+} ions in different hosts media," *Opt. Mater. (Amst).*, vol. 41, pp. 116–121, 2015.

[193] W. Stręk, A. Bednarkiewicz, and P. J. Dereń, "Power dependence of luminescence of Tb^{3+}-doped $KYb(WO_4)_2$ crystal," *J. Lumin.*, vol. 92, no. 3, pp. 229–235, 2001.

[194] S. Kasap, K. Koughia, G. Soundararajan, and M. G. Brik, "Optical and photoluminescence properties of erbium-doped chalcogenide glasses (GeGaS:Er)," *IEEE J. Sel. Top. Quantum Electron.*, vol. 14, no. 5, pp. 1353–1360, 2008.

[195] M. Saisudha and J. Ramakrishna, "Effect of host glass on the optical absorption properties of Nd^{3+}, Sm^{3+}, and Dy^{3+} in lead borate glasses," *Phys. Rev. B*, vol. 53, no. 10, pp. 6186–6196, 1996.

[196] O. O. Madelung, U. Rössler, and M. Schulz, "Nd_2S_3: crystal structure, physical properties BT - Non-Tetrahedrally Bonded Binary Compounds II," in *Non-Tetrahedrally Bonded Binary*

Compounds II, O. Madelung, U. Rössler, and M. Schulz, Eds. Berlin, Heidelberg: Springer, Berlin Heidelberg, 2000, pp. 1–22.

[197] J. R. Ferraro, K. Nakamoto, and C. W. Brown, *Introductory Raman Spectroscopy*, Second Edi., Amsterdam: Academic press, 2003.

[198] S. E. Stokowski, R. A. Saroyan, and M. J. Weber, *Nd-doped Laser Glass Spectroscopic and Physical Properties*. Lawrence Livermore National Laboratory, University of California, 1981.

[199] A. Belykh *et al.*, "Spectral and luminescence properties of neodymium in chalcogenide glasses," *J. Non. Cryst. Solids*, vol. 213–214, pp. 238–244, 1997.

[200] B. Viana, M. Palazzi, and O. LeFol, "Optical characterization of Nd3+ doped sulphide glasses," *J. Non. Cryst. Solids*, vol. 215, no. 1, pp. 96–102, Jul. 1997.

[201] K. Arai, H. Namikawa, K. Kumata, T. Honda, Y. Ishii, and T. Handa, "Aluminum or phosphorus co-doping effects on the fluorescence and structural properties of neodymium-doped silica glass," *J. Appl. Phys.*, vol. 59, no. 10, pp. 3430–3436, May 1986.

[202] A. Ravagli, C. Craig, G. A. Alzaidy, P. Bastock, and D. W. Hewak, "Optical, Thermal, and Mechanical Characterization of Ga_2Se_3-added GLS Glass," *Adv. Mater.*, vol. 29, no. 27, p. 1606329, Jul. 2017.

[203] M. J. Lim, Y. N. Ko, Y. Chan Kang, and K. Y. Jung, "Enhancement of light-harvesting efficiency of dye-sensitized solar cells via forming TiO_2 composite double layers with down/up converting phosphor dispersion," *RSC Adv.*, vol. 4, no. 20, p. 10039, 2014.

[204] N. Yao *et al.*, "Enhanced light harvesting of dye-sensitized solar cells with up/down conversion materials," *Electrochim. Acta*, vol. 154, pp. 273–277, 2015.

[205] M. Liu, Y. Lu, Z. B. Xie, and G. M. Chow, "Enhancing near-infrared solar cell response using upconverting transparentceramics," *Sol. Energy Mater. Sol. Cells*, vol. 95, no. 2, pp. 800–803, Feb. 2011.

[206] W. Clegg, "X-ray Diffraction," in *Comprehensive Coordination Chemistry II*, Elsevier, 2003, pp. 57–64.